UNIVERSITY OF SOUTHAMPTON

Mode-locked Surface Emitting Semiconductor Lasers

by

Zakaria Mihoubi

A thesis submitted in partial fulfillment for the
degree of Doctor of Philosophy

in the
Faculty of Engineering, Science and Mathematics
School of Physics and Astronomy

November 2009

UNIVERSITY OF SOUTHAMPTON

ABSTRACT

FACULTY OF ENGINEERING, SCIENCE AND MATHEMATICS
SCHOOL OF PHYSICS AND ASTRONOMY

Doctor of Philosophy

MODE-LOCKED SURFACE EMITTING SEMICONDUCTOR LASERS

by Zakaria Mihoubi

Optically-Pumped Vertical External Cavity Surface Emitting Lasers (OP-VECSELs) are novel semiconductor-based lasers that have many advantages over other lasers in terms of the power scalability, good beam quality, compactness and low cost they can offer. They can be passively mode-locked with a Semiconductor Saturable Absorber Mirror (SESAM) to produce transform-limited sub-300 fs pulses directly from the laser cavity with high repetition rates.

This thesis describes an experimental and theoretical investigation of OP-VECSELs. A full characterization is done on a VECSEL sample to understand the physics behind its operation in the Continuous Wave (CW) mode and in the mode-locked mode. Then, a numerical model that, for the first time, shows the role of the Optical Stark Effect (OSE) in shaping the mode-locked pulses in the approach to steady state is introduced. The model results are broadly consistent with observed behavior of our mode-locked VECSELs.

Here, I also report the first coherent generation and detection of terahertz radiation using all-semiconductor components. Radiation with a bandwidth of 0.8 THz has been generated using sub-500 fs pulses with an average power of 20 mW from a mode-locked VECSEL which contains InGaAs quantum wells and an LT-GaAs/InGaAs emitter/receiver antenna in a Terahertz Time Domain Spectrometer (THz-TDS) setup. The first mode-locked OP-VECSEL at 830 nm is reported here. The combination of a GaAs quantum well-based gain sample and SESAM yielded an output with an average power of 5 mW and 15 ps-long pulses at a repetition rate of 1.9 GHz. A pumping module used to drive the laser was built for this purpose by combining the output of two commercial 665 nm diode lasers.

Declaration of Authorship

I, Zakaria Mihoubi, declare that the thesis entitled 'Mode-locked Surface Emitting Semiconductor Lasers' and the work presented in the thesis are both my own, and have been generated by me as the result of my own original research. I confirm that:

• this work was done wholly or mainly while in candidature for a research degree at this University;

• where any part of this thesis has previously been submitted for a degree or any other qualification at this University or any other institution, this has been clearly stated;

• where I have consulted the published work of others, this is always clearly attributed;

• where I have quoted from the work of others, the source is always given. With the exception of such quotations, this thesis is entirely my own work;

• I have acknowledged all main sources of help;

• where the thesis is based on work done by myself jointly with others, I have made clear exactly what was done by others and what I have contributed myself;

• parts of this work have been published as listed in Appendix B.

Signed:

Date: 31/10/2009

Contents

List of Figures

List of Tables

Acknowledgements

Here, I would like to take a moment to acknowledge the many people who helped me through the PhD phase of my life. It is difficult to put in words my gratitude to my PhD supervisor Prof. Anne Tropper. With her enthusiasm, inspiration and great deal of knowledge of the research domain, she helped me through the rough parts of my research as well as the fun parts. She was there when I needed help with either the experimental side of my work or the theoretical side of it. Because of that I say Thank you, Anne. I would also like to acknowledge the whole of my family for their patience and support throughout my time abroad. Despite the far distance from home, they were all a phone call away offering me all kinds of advice and encouragement. I am also grateful to Dr Vasilis Apostolopoulos who joined the department and helped us restart one of our most ambitious projects with Terahertz spectroscopy. He was there when I needed help and advice. A big thank you goes to Dr Geoff Daniell who helped enormously with his theoretical work on modelling the saturable absorbers used throughout this thesis. His insight into the domain of numerical modelling was a keystone for some of the successful work presented here.

I would like to thank the VECSEL group members I worked with through the years. Dr Keith Wilcox and Dr Hannah Foreman who helped get me started on my projects. A special thank you to Dr Wilcox who worked with the group as a Post Doc for about a year. During this period a great deal of work was published by the group partly due to his enthusiasm and hard work. I would like to thank Stephen Elsmere and Adrian Quarterman for their support and help through the years. Since we shared the learning curve in out PhDs, it was four years full of hard work and fun. I would like to also thank Dr Jacob Mackenzie, Aaron Chung and all the collaborators and sample growers that we worked with in joint projects. I would like to thank Jennifer Hastie for kindly lending us one of her samples to use in the mode-locking of an 840 nm VECSEL. Thanks to all members of the QLM for sharing their knowledge and research in the various seminars and colloquiums. Thanks to all the support staff who helped with either setting up the labs or making workshop item for the various projects described here.

To Mum, Dad , Yahia, Tarek, Hicham and Zizou

Chapter 1

Introduction

Optically Pumped Vertical External Cavity Surface Emitting Lasers (OP-VECSELs), also known as semiconductor disk lasers (SDL), are semiconductor based lasers that distinguish themselves from others such as VCSELs by having an external cavity. This allows the device to impose a low divergence, circular, near diffraction limited, high quality output beam and it also allows for a large emitting area for power scaling. Other features of VECSELs include the versatility of quantum wells which allows the freedom to select wavelengths of the output and the possibility to access the mode in the high-Q cavity with low output coupling. Gain samples for VECSELs are usually grown using metal-organic vapor phase epitaxy (MOVPE) or molecular beam epitaxy (MBE).

The first VECSEL demonstration was made by Kuznetsov et al in 1997 [1] in which 0.5 W of continuous wave (CW) power at 1004 nm was achieved in a TEM_{00} mode with a power transfer efficiency greater than 30%. In his work, an InGaAs/GaAsP/GaAs multi-quantum well structure (MQM) was optically pumped with a commercial diode laser emitting up to 3 W at 808 nm. Kuznetsov's ground breaking work in [1] and his blue print for making VECSELs published in [2] established the pathway for the development of VECSELs, and since then it has seen a huge rise in interest among the scientific community.

Researchers are targeting VECSELs as strong candidates to replace expensive and bulky laser systems in their labs. VECSELs, among other things, have given access to wavelengths that were, in the past, exclusive to certain types of lasers like solid state lasers and fibre lasers. Their development has not just been about finding competitive wavelength sources because a lot of research has targeted VECSEL output powers, active and passive mode-locking as well as finding new applications for these devices.

The gain medium of a VECSEL can be pumped either optically or electrically. The latter case makes sample growth complicated because of the need to incorporate p-n junctions and making electrical contacts[3, 4, 5]. Novalux Inc. supports this way of pumping and owns a patent for NECSELs (Novalux External Cavity Semiconductor Lasers) which use electrical pumping and are aimed at making displays and projection TVs.

Absorption lengths for semiconductors are generally short and are of the order of a few microns so consequently, pump absorption efficiency is high in the active region of these devices with the added bonus of a simple growth process. Standard diode-pumping techniques developed for solid state laser are used to achieve uniform pumping of an emitting area that can be much larger than in other types of semiconductor laser.

These techniques can be divided into different types depending on the targeted absorption region of the VECSEL structure. In barrier pumping, pump light is absorbed by barriers on either sides of the quantum wells [2]. This leads to the creation of carriers which are trapped in the wells. It is the simplest of the two configuration but since the difference in bandgaps between the wells and the adjacent layers is large, the difference between pump wavelength and lasing wavelength will consequently be high too. Consequently, this method of pumping has a lower limit for quantum defect which is defined as the energy difference of pump and laser photons. As a result, heating is more of an issue in this case.

In the second configuration, known as in-well pumping, pump light is absorbed by the quantum well. This has the advantage of lowering the quantum defect due to the small difference between lasing and pumping wavelengths [6, 7]. However, since quantum wells are usually a few nanometres thick, the absorption efficiency is low compared to the first method. Beyertt et al produced 1.9 W at 980 nm using a sample pumped in-well at 940 nm. This laser had a slope efficiency of 35% but with 70% of pump radiation absorbed by the well [8].

A recently developed method of pumping is called end-pumping. In this scheme, the substrate is removed by selective wet etching, then liquid capillary bonding method is used to bond the DBR side of VECSEL chip to the surface of an optically transparent heat spreader. Pumping in this case is done from a diode laser through the DBR structure which was designed with a reduced reflectance to avoid losses. Multi-Watt level operation has been demonstrated from this way of pumping in [9, 10, 11].

The wavelength of the laser output from a VECSEL can be designed by varying the quantum well material that makes up the active region. VECSELs with output wavelengths ranging from 391 nm up to 5 μm have been demonstrated and are listed along with their composition in [3]. It includes an 850 nm result from GaAs/AlGaAs/GaAs quantum wells [12], a 0.6 W CW at 1320 nm from a GaInNAs-based VECSEL [13], a 0.7 W CW power at 1555 nm from InP-based structure [14] and 3 mW of CW at 5 μm were reported in [15].

Power scalability has been demonstrated in VECSELs through efficient heat removal from the pumped area. The total thickness of the active region is of the order of 20 μm which makes the material thin enough for the heat flow through it to be approximately one-dimensional [3]. Hence the output power can be increased by increasing the mode area on the gain sample and the pump power by the same factor. Powers of up to 30 W have been demonstrated by Chilla et al in [16].

The major constraints on the performance of VECSELs in terms of output powers are thermal effects. As with most semiconductor based lasers, the effective gain is reduced as temperature rises and power roll-over is often seen in this case. Pumping large areas adds to the thermal load in the structure via effects such as Auger recombination that compromise the available power and often lead to multimode behaviour of the laser. Efficient heat removal techniques are needed to manage these effects.

An example of these techniques involves the removal of the substrate via selective etching. Residual pump power gets absorbed in substrate on which the VECSEL structure is grown leading to unwanted heat[17, 16, 2]. The leaves a relatively thin gain sample with a total thickness of around 20 μm which can be bonded to a heat sink ensuring an efficient heat removal from the active region. In another technique, materials with high thermal conductivity are used as heat spreaders and are attached to the front of the gain sample to help evacuate the thermal load from the pumped spot. Silicon Carbide (SiC) was used to achieve a power of 0.5 W at 850 nm in [18, 19]. A diamond heat spreader was used to achieve 10 W of CW power at 1060 nm from an InGaAs-based VECSEL [20].

Another way of obtaining high power from a VECSEL is the use of a multi-chip gain sample. Fan et al reported a CW power of 19 W at 970 nm from a cavity utilising two gain chips with an M^2 of 2.1 [21]. They also observed the tunability of the optical spectrum of the output over a range of 33 nm in [22]. Fibre amplification of VECSEL

output power has also been demonstrated in [23, 24] with average output powers of 187 W achieved.

VECSELs are also attractive as compact and potentially high power sources of short pulses through either active [26] or passive mode-locking. The first passively mode-locked VECSEL was demonstrated by Hoogland et al using a Semiconductor Saturable Absorber Mirror (SESAM)[27]. A refinement of the SESAM design led to the successful demonstration of sub-500 fs pulses at 1 μm with a repetition rate of 1 GHz [28]. This SESAM utilises the Optical Stark Effect, which can be described as an instantaneous blue shift of the absorber resonance, as a mechanism for pulse shortening which will be described in details in Chapters 3 and 4. Klopp et al showed near transform-limited 190 fs pulses at 1036 nm [29] with 3 GHz repetition rate and 10 mW of average power. One of the shortest pulses from a VECSEL was obtained by Wilcox et al in our group. His results showed 260 fs transform-limited pulses at a 1 GHz repetition rate [30] with 25 mW average output power at 1035 nm. More recently, Wilcox et al showed an improved result of 70-fs transform-limited pulses in[31]. A high power 2.1 W VECSEL giving 4.7 ps pulses at 4 GHz has also been demonstrated [32].

More developments have seen quantum dot saturable absorbers (QD-SESAM) being used to passively mode-lock lasers. For a VECSEL system, this was demonstrated in [33] with 9.7 ps pulses at a frequency of 20 GHz. This opened the door for the idea of wafer integration of the gain medium and the saturable absorber. Recently, this idea has been demonstrated with the introduction of the 'mode-locked integrated external-cavity surface emitting laser' (MIXSEL) [34]. An average output power of 185 mW with 32 ps pulses at around 3 GHz pulse repetition rate was shown. The shortest pulse from a VECSEL with a QD-SESAM is an 870 fs at 1027.5 nm reported by Wilcox et al in [35].

Recently, the first VECSEL with a quantum dot-based gain region was demonstrated by Hoffmann et al in [36]. He used 35 layers of QDs to make a 1060 nm VECSEL and succeeded in mode-locking it with a SESAM to get 18 ps long pulses at 2.57 GHz repition rate and 27 mW average output power.

Scaling down VECSELs to the highest possible repetition rates naturally leads one to contemplate some form of monolithic structure in which gain and absorber are integrated into one single semiconductor layer sequence. Up to 100 GHz repetition rate from a VECSEL has been demonstrated in [37]. Such a monolithic device would allow to reduce the cavity to a simple linear geometry requiring only an external output coupler at a distance from the chip which determines the desired repetition rate. High repetition

rate lasers are sought after for applications such as telecommunication, optical clocking and analogue-to-digital conversion.

The work presented in this thesis will aim to develop our understanding of VECSELs further. I will start by laying some foundation about the process of designing VECSELs and SESAMs. I will then dedicate two Chapters, 3 and 4, to present some theoretical and experimental work about the mechanism behind passive mode-locking of VECSELs with a slow saturable absorber. The theoretical work presented in chapter 3 relies heavily on Dr G Daniell's analysis of the SESAM.

In Chapter 5, I will present results of the first VECSEL-pumped terahertz spectrometer. By taking advantage of the compactness of the VECSEL, the setup that will be described has the potential to be mobile and efficient. Finally, I will describe my successful attempt to build the first passively mode-locked 830 nm VECSEL. This region of the spectrum is dominated by the Ti-Sapphire laser which is used in remote sensing, medicine, and research and development applications. The potential of the VECSEL at this wavelength will be discussed.

Chapter 2

Experimental Characterisation of CW and Mode-Locked VECSELs

2.1 Introduction

In this chapter, I will describe techniques used to characterise semiconductor epilayer structures used to construct modelocked VECSELs. I will illustrate the methods with data for a sample I labeled QT1872D. This structure was designed for the purpose of acting as a sub-picosecond seed source to a ytterbium-doped fibre amplifier (YDFA) at approximately 1055 nm [23]. I will also discuss the mode-locking of VECSELs by SESAMs since it is with this mode of operation that most of the results presented in this thesis are obtained.

VECSELs contain a gain sample that acts as an 'active mirror' with an active region made up of quantum wells (QWs) and a Distributed Bragg Reflector (DBR) grown behind, and have a thickness of only a few micrometers. A schematic diagram of a VECSEL is shown in Fig 2.1. The figure also shows the layer structure of a typical gain sample highlighted through the variation in the bandgap energies of the layers. In this particular example and starting from the left side of the picture, we have alternating layers of AlAs and GaAs that make up the DBR which acts as highly reflective mirror. Then we have an active region of GaAs with six QWs embedded in it. In this case each QW has GaAsP strain compensating layers as shown. An AlAs window layer is next and finally a GaAs capping layer finishes off the layer structure. The function and mechanism of operation of such a sample will be explained in this chapter.

The design process for a VECSEL starts by choosing the emission wavelength of the laser and then carefully picking the quantum well material most suited for this emission. It is important to take into consideration when picking the design wavelength the fact that, under intense pumping, the gain sample is typically heated by up to 60^{o}C which will lead to a red wavelength shift. The pump wavelength dictates the composition of the quantum well barriers. The issue that arises in some cases is the lattice mismatch between some materials. This can be seen in the bandgap versus lattice constant plot for systems based on GaAs as shown in Fig 2.2 [3]. Employing material that has a mismatch in lattice constant gives rise to strain in the chip between adjacent layers which in turn causes device degradation over time. However, strain can be beneficial when present in a system as it improves peak and differential gain characteristics and reduces losses [38, p. 437-448]. From Fig 2.2, one can see, for example, that AlGaAs is lattice matched with GaAs for all concentrations of aluminum which allows AlGaAs material to be grown on GaAs substrate with no defects.

One way of overcoming the lattice mismatch is the introduction of strain-compensating layers (SPLs) that can be grown on either side of a quantum well to give the gain chip some rigidity. In Fig 2.1, each of the six InGaAs quantum wells contained in the active region have GaAsP strain-compensating layers on both sides. Due to the difference in lattice constant between the barriers and the quantum wells, quantum wells experience a compressive strain and the barriers are under tensile strain. The SPLs role is to offset the shear force on the substrate.

Compounds such as InGaAs/GaAs/AlGaAs can be used as sources for near-infrared wavelengths in the range of 800-1100 nm because of the near-perfect lattice match between GaAs and AlGaAs. All work presented here, apart from Chapter 6, was done using VECSELs employing an InGaAs/GaAs/AlGaAs compound. By adding phosphorus, for example, materials for making red lasers becomes available as was demonstrated in [39].

The capping layer is added to stop oxidation of the window layer which contains aluminium in some cases. The role of the window layer, which is made of AlAs in the QT1872D sample, in the gain structure is to work as a tuning element (at the design stage) for what is known as the microcavity enhancement factor (MCEF). The window layer and the active region form the microcavity whilst the MCEF is a dimensionless number that represents the strength of coupling between the electric field intensity and the quantum wells.

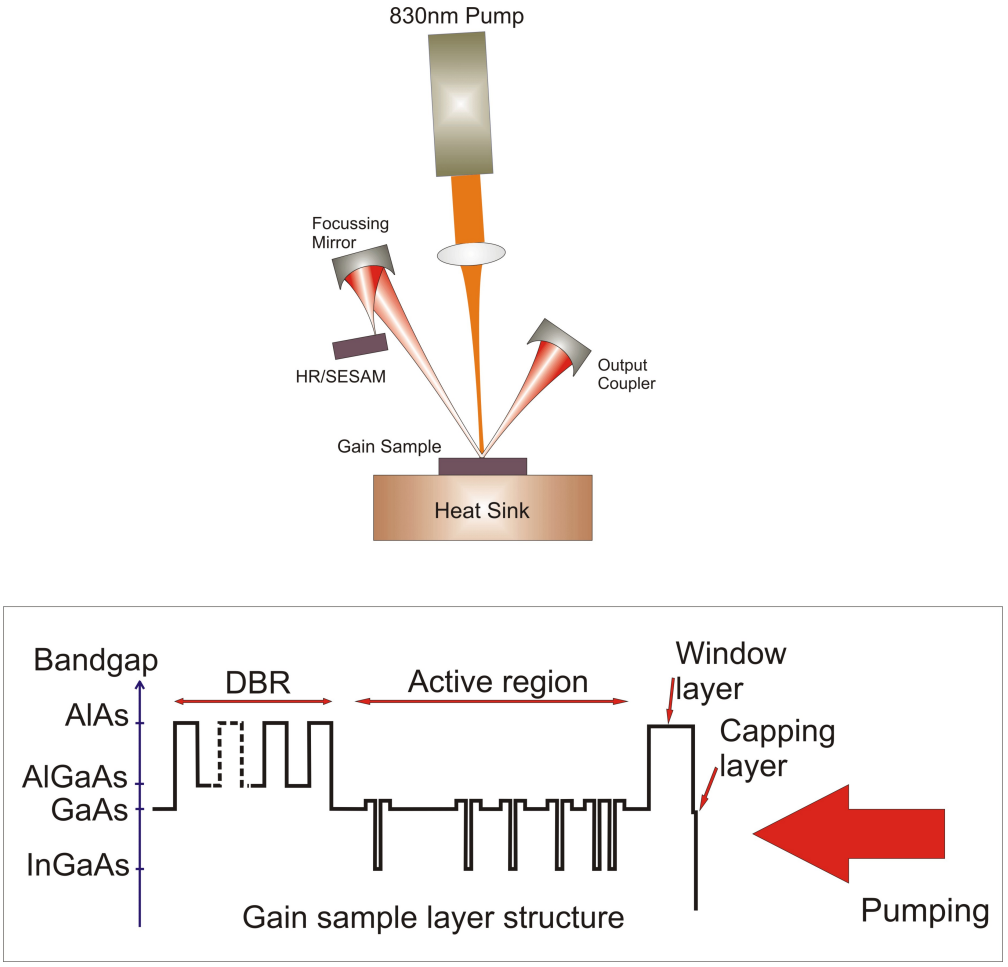

FIGURE 2.1: A schematic of a typical VECSEL components. HR: High Reflector for continuous wave mode of operation. An example of a layer list of a gain sample is shown at the bottom. Samples are usually grown on top of a substrate.

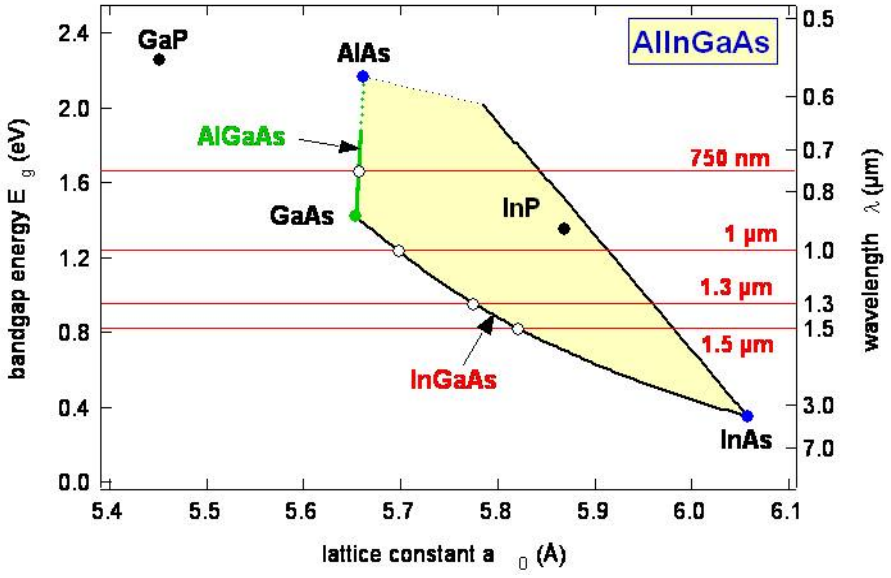

FIGURE 2.2: Bandgap energy plotted against lattice constant of various III-V semiconductors at room temperature.

The importance of the MCEF comes to light when we consider the total gain of the VECSEL sample. The latter is defined as the product of the MCEF and the material gain [40, p. 449-455]. The MCEF, Γ, is given by

$$\Gamma = \frac{\sum^{n} |E(z_n)|^2}{|E(air)|^2} \tag{2.1.1}$$

where $|E(z_n)|^2$ is the intensity of the E-field on top of the n^{th} quantum well. The multilayer program used for designing a gain structure is used to calculate this. $|E(air)|^2$ is the intensity of the E-field in the air just outside the sample.

By changing the the thickness of the window layer, one is effectively changing the length of a Fabry-Perot etalon which is formed between the DBR on one side and the air-sample interface, since the index of refraction contrast is high, on the other side. The standing wave pattern created inside the etalon by the double pass of the laser mode through the microcavity has an antinode at the DBR-active region interface for a resonant structure whilst this is set to a node for an anti-resonant structure.

The DBR design is done to achieve a highly reflecting mirror centred around the design wavelength behind the active region by using alternating quarter-wavelength-thick layers with high and low refractive indices. Fig 2.3 shows plots of the calculated reflectivity against wavelength for DBRs with differing number of pairs of GaAs/AlAs layers. As the number of layers increase the maximum reflectivity of the stop band, highlighted on Fig 2.3, also increases until a point where variations become minimal. More and more modulations on either side of the stop band appear as the number of pairs increase. The number of layers is chosen such that the stop band reflectivity is reached with the minimum amount of layers to keep the growth as simple as possible.

The active region in some of our samples is set at 7x$\lambda/2$ which allows for the pump light to get absorbed fully before reaching the DBR. Since the DBR contains GaAs at this region of operation (near 1 μm), it can absorb pump light which in turn causes heating that could jeopardise the device efficiency.

The modus operandi of a VECSEL is described next. Spacer layers grown between QWs have the important role of absorbing the pump radiation. This leads to the creation of carriers via the promotion of an electron from the valence band to the conduction band leaving behind a hole. These carriers will then move into the quantum wells and get trapped. At this stage, carrier-carrier and carrier-phonon scattering processes occur on

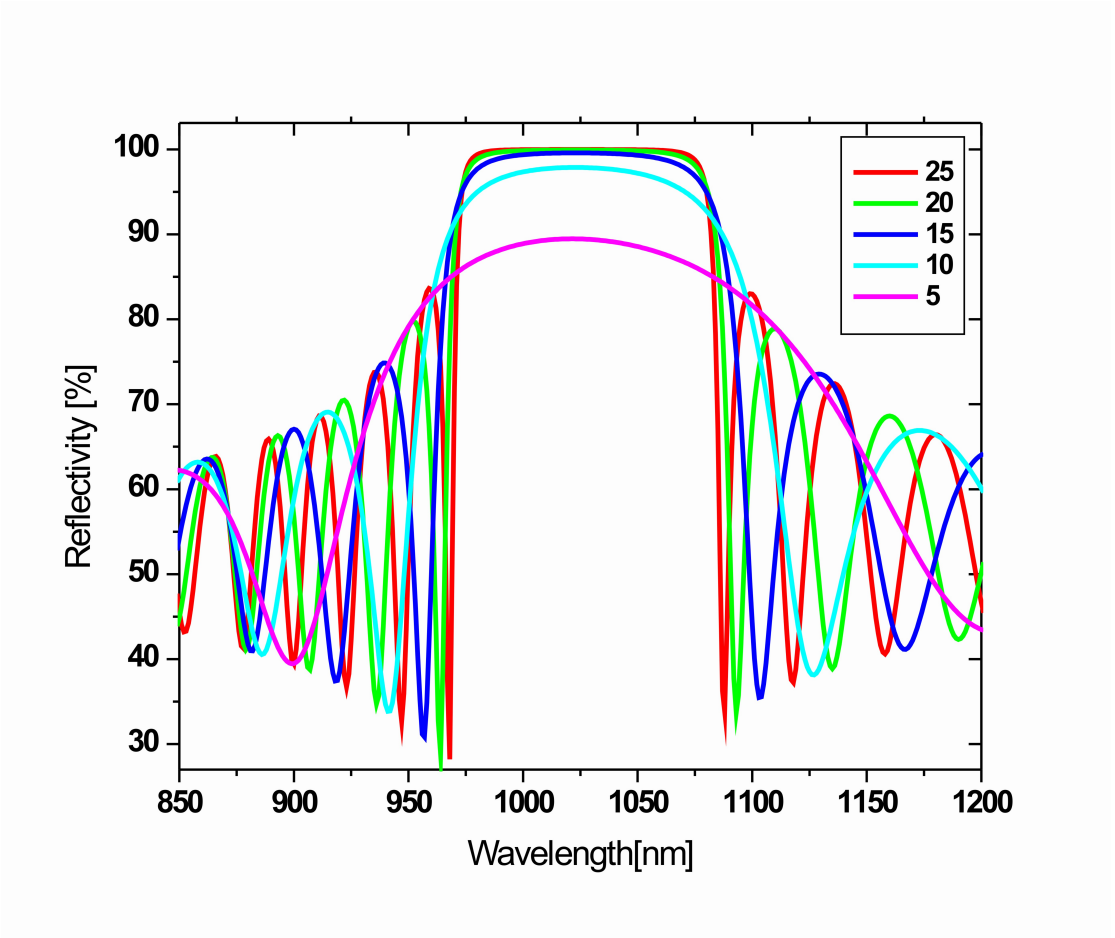

FIGURE 2.3: Reflectivity of Distributed Bragg Reflectors with different number of layers as a function of wavelength

a scale of a few hundred femtoseconds timescale alongside thermalisation of their distribution. A comparatively longer process then takes place in the form of recombination. This can happen radiatively through the emission of a photon or non-radiatively through defects or Auger recombination.

The position of the QWs in the active region is dictated by the profile of the electric field intensity in this region. QWs are positioned at the antinodes of the profile for maximum gain. An example of how the intensity profile looks in the resonant structure configuration is shown in Fig 2.4-A, where I have set the window layer thickness to 2xλ. In general, this is set to a multiple of $\lambda/2$ which leads to an antinode at the air/window layer interface. Structures like this usually offer high gain and low threshold lasers, since the quantum well coupling efficiency is optimised. This is highlighted by Fig 2.4-B which shows the MCEF Γ plotted against wavelength. It shows a narrow resonance peak around the design wavelength, 1025 nm in this example, with a peak of around 3.2.

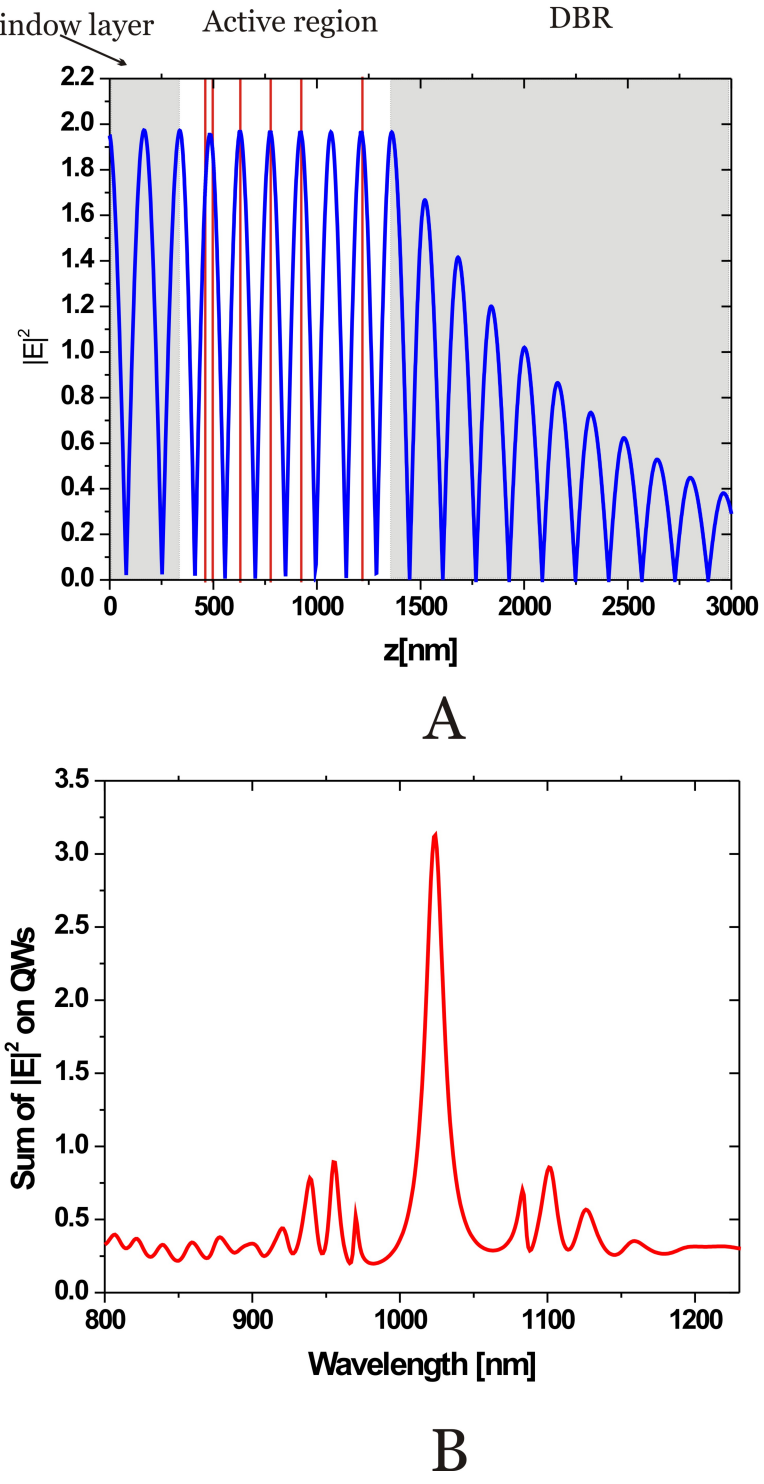

FIGURE 2.4: Signatures of a resonant gain sample structures. A- Electric-field intensity profile inside the sample as a function of distance inside the sample from the air interface (left side) to a couple of microns inside the DBR. B- A theoretical estimation of Γ by normalising E-field intensity on the QWs with that of air.

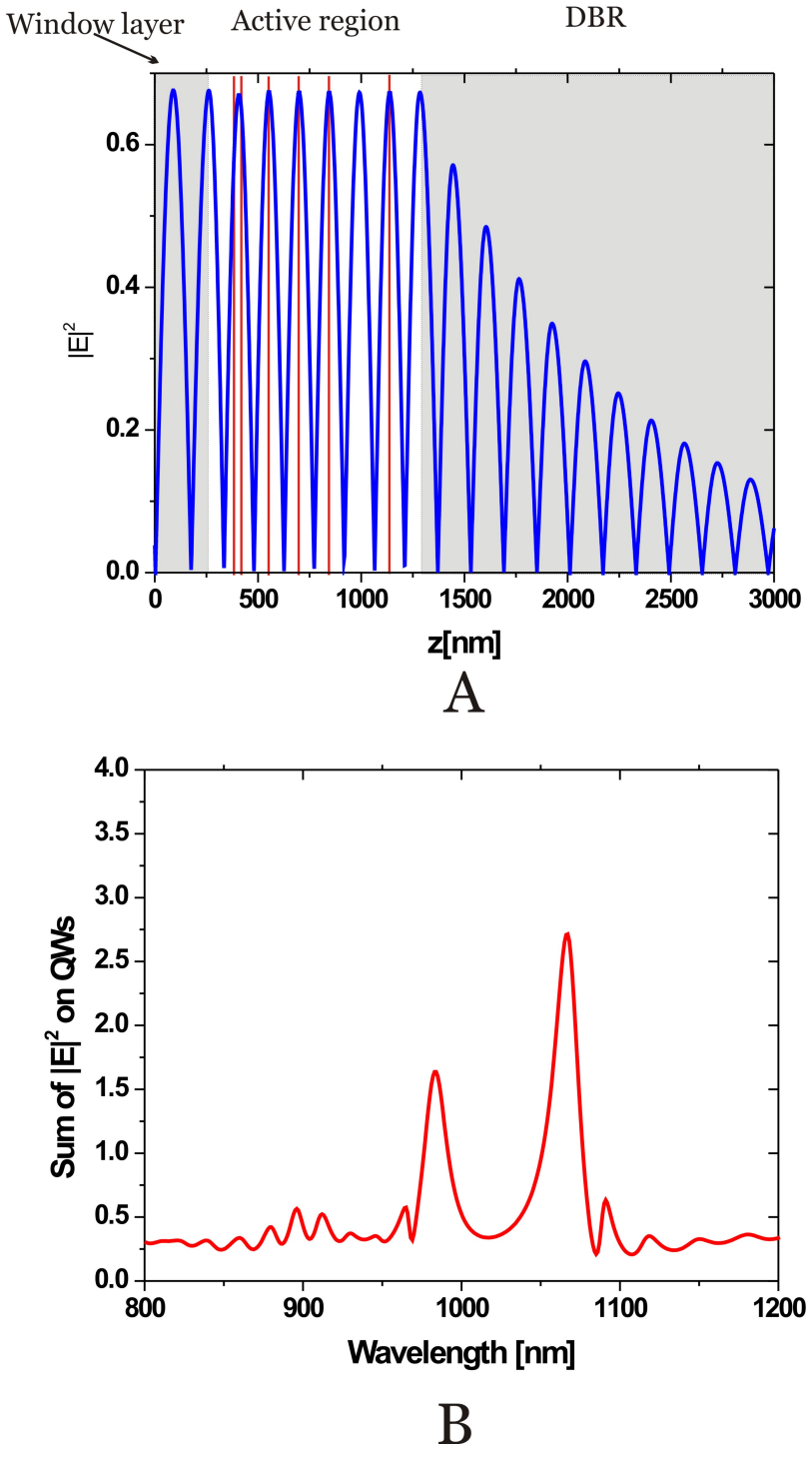

FIGURE 2.5: Signatures of a anti-resonant gain sample structures. A- Electric-field intensity profile inside the sample as a function of distance inside the sample from the air interface (left side) to a couple of microns inside the DBR. B- A theoretical estimation of Γ by normalising E-field intensity on the QWs with that of air. This shows a broad resonance in contrast to the resonant case.

The second extreme case is when there is a node at the air/window layer interface which is called an anti-resonant sample. Fig 2.5 highlights this case with similar plots as in Fig 2.4. One of the differences can be seen in Fig 2.5-B which shows the MCEF. The resonance in this case is much broader and relatively flat around the centre wavelength but with less intensity. This is expected since the quantum well coupling is less efficient in this case. This design is usually aimed for mode-locking.

In order to help create a homogeneous carrier population in each one of the quantum wells, the distribution of QWs does not have to be uniform as, for example, two QWs can be positioned under an antinode. Utilising the Beer-Lambert law for radiation transmission though a sample, the spacing between these QWs is set for an optimised carrier capture. A higher concentration of quantum wells is grown in the regions with higher carrier concentration to even out carrier distribution.

2.2 Gain Sample Characterisation

Gain samples are designed to operate at a specific wavelength, with optimised spectral characteristics. In order to test these properties, and hence the accuracy of the growth, some characterisation experiments are performed. The measured reflectivity spectrum shows where the DBR stop band is which can be compared to the theoretical value obtained from gain simulations. Top and edge photoluminescence measurements are undertaken to provide information about the quantum well emission with and without the microcavity enhancement (i.e. coupling between quantum wells and laser light) by the different layers inside the sample.

A gain sample labeled QT1872D is used at this stage to highlight the characterisation process of a gain sample. It was designed to give an output at 1060 nm with a broad gain bandwidth of 100 nm from an optical pumping at 830 nm, in order to be used as the gain sample in a mode-locked VECSEL that would provide seed pulses for the fibre amplifier. The arrangement of layers is shown schematically in Fig 2.6. The structure incorporated etch stopping layers which are made up of 300 nm thick $Al_{0.84}Ga_{0.16}As$, a 20 nm GaAs, a 75 nm layer of AlAs and a $\lambda/4$ GaAs layer with the aim of removing the substrate later by the process of etching. The Bragg mirror is made up of 27.5 pairs of $AlAs/Al_{0.2}Ga_{0.8}As$ layers. The gain sample also features an active region containing a $3x\lambda/4$ GaAs layer that incorporates six strain compensated $GaAsP_{0.06}/InGaAs/GaAsP_{0.06}$ quantum wells emitting at 1020 nm at low excitation and at room temperature. The $1.5x\lambda/2$ top layer

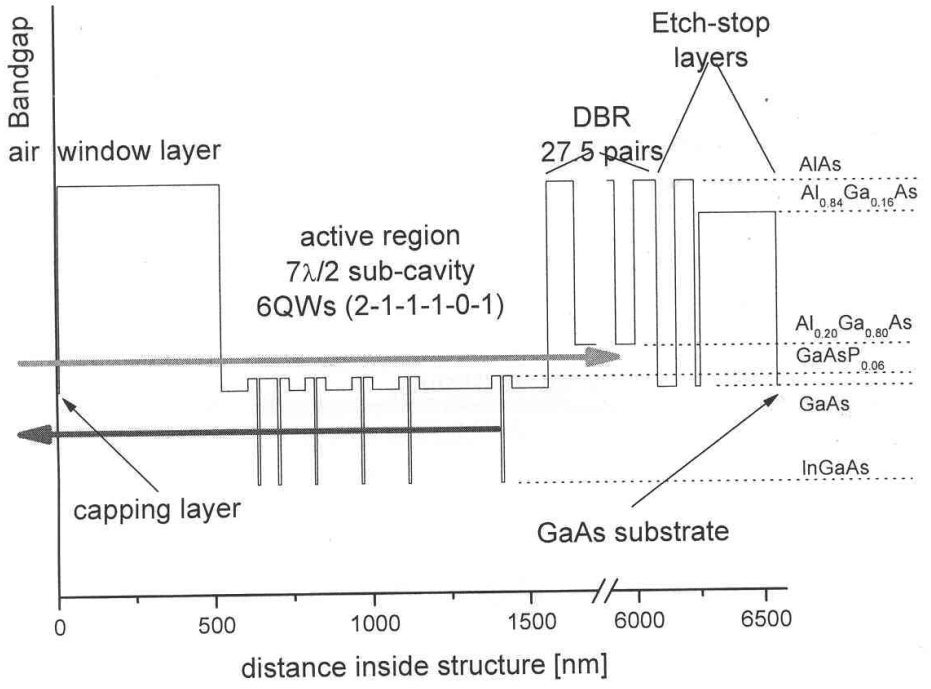

FIGURE 2.6: A schematic diagram showing the layer sequence for the QT1872D gain sample. It features 6 InGaAs strain compensated quantum wells in a $7\lambda/2$-length active region

is made of AlAs and finally a capping layer to prevent oxidation is made of GaAs with a thickness of 8 nm.

2.2.1 Reflectivity measurements

The measured variation of reflectivity of a chip from wafer QT1872D as a function of wavelength is shown in Fig 2.7 (solid red), together with a theoretical curve (dashed black) calculated using the matrix method described in [3] which had previously been implemented in Igor, a simulation software, by Hoogland [41]. This was obtained using a Jasco UV/VIS/NIR spectrophotometer capable of measuring the transmission, absorption and reflectance of samples at wavelengths from 190 to 2500 nm by placing samples on top of a 150 mm-diameter pinholes. It uses a Halogen lamp for the 330 to 2500 nm spectral range. It can be seen that the stop band is shifted to longer wavelength showing that the as-grown layers are slightly too thick. It was therefore interesting to investigate the properties of this wafer as a possible gain chip for a laser at the YDFA seed wavelength of 1055 nm. A small absorption dip can be seen at about 1030 nm in an approximately 100 nm-broad stop band; however the low signal to noise ratio of the

detector is obscuring it. This dip indicates a microcavity resonance and is a product of the intrinsic absorption of the quantum wells and the MCEF. The discrepancy between the two curves in the wings is mainly due to the fact that the interpolation formula for the refractive index is less accurate away from the design wavelength.

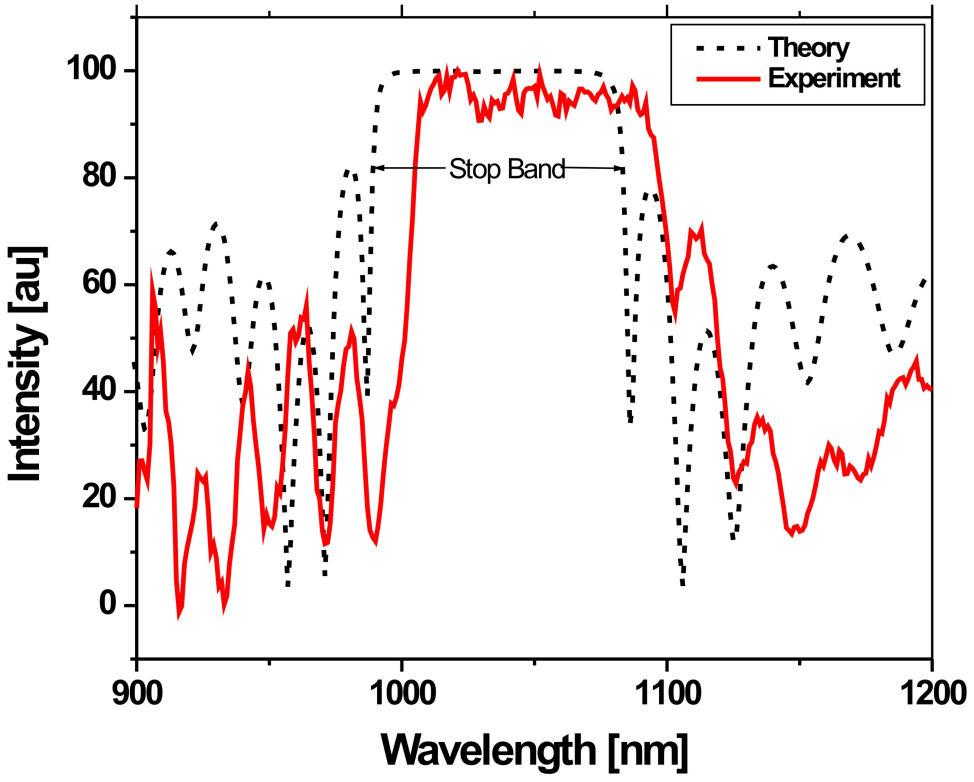

FIGURE 2.7: Reflectivity curve of the gain sample QT1872D. A slight misalignment of the spectrum was to blame for the shallower than expected absorption dip

2.2.2 Edge Photoluminescence

Edge PL measurement gives the intrinsic shape of the exciton resonance spectrum containing information of the gain medium. The measurement technique of edge PL involved mounting the gain sample on a copper block and attaching the compound to a heat sink using silver paint for temperature control. The sample was then pumped by an 830-nm fibre-coupled diode laser emitting up to 1 W of power from a 30 μm-core radius fibre. The fibre output is collimated with a 35 mm focal length doublet lens, and focussed down to a 60 μm radius spot on the sample surface by a 75 mm focal length doublet lens.

Optically pumped quantum wells emit photoluminescence in all directions; with the use of a microscope objective some of this radiation was collected and then sent to an optical spectrum analyser connected to a computer to record the data. The microscope was placed behind the gain sample at an angle of about 15 degrees from the surface of the sample so that it did not collect any reflections of the pump beam or any modulated PL (see next experiment). The PL spectrum was dispersed using a 0.25-m grating spectrometer and detected by a 1024-element Si-photodiode array.

The optical spectrum of edge emitted PL is shown on a logarithmic scale in Fig 2.8 as a function of input power and temperature. It shows that an increase in temperature or input power leads to a shift to a longer wavelength of the maximum of the spectrum with a rate of 0.3 nm/K and 17.4 nm/W respectively. This shows that the gain falls with increasing temperature due the fact that the thickness of the quantum wells changes with temperature. The total photoluminescence emitted also decreases slightly with increasing temperature at a constant pump power due to the non-radiative recombination of carriers at high temperatures. The emitted PL is significantly greater for higher pump power due to the increased rate of carrier creation and trapping in quantum wells.

2.2.3 Top Photoluminescence

Photoluminescence emitted vertically out of the multilayer structure (top PL) shows strong modulations produced by the interference in the multilayer structure. The top PL measurements share the same set up as the edge PL except for the position of the point of collection of this radiation. Only the modulated photoluminescence due to the multilayers embedded in the gain is collected by using a lens with its axis perpendicular to the sample surface to collect the top PL which is then analysed it by the spectrum analyser. Fig 2.9 shows the resulting data plotted for different temperatures and input powers. It shows the expected modulations due to the microcavity inside the gain sample; similar shifts due to changing temperature can be seen, but in this case they are due to changing thicknesses from all the layers in the sample which makes the peak wavelength tunes differently with temperature and power to that in the case of edge PL (0.09 nm/K and 9.8 nm/W).

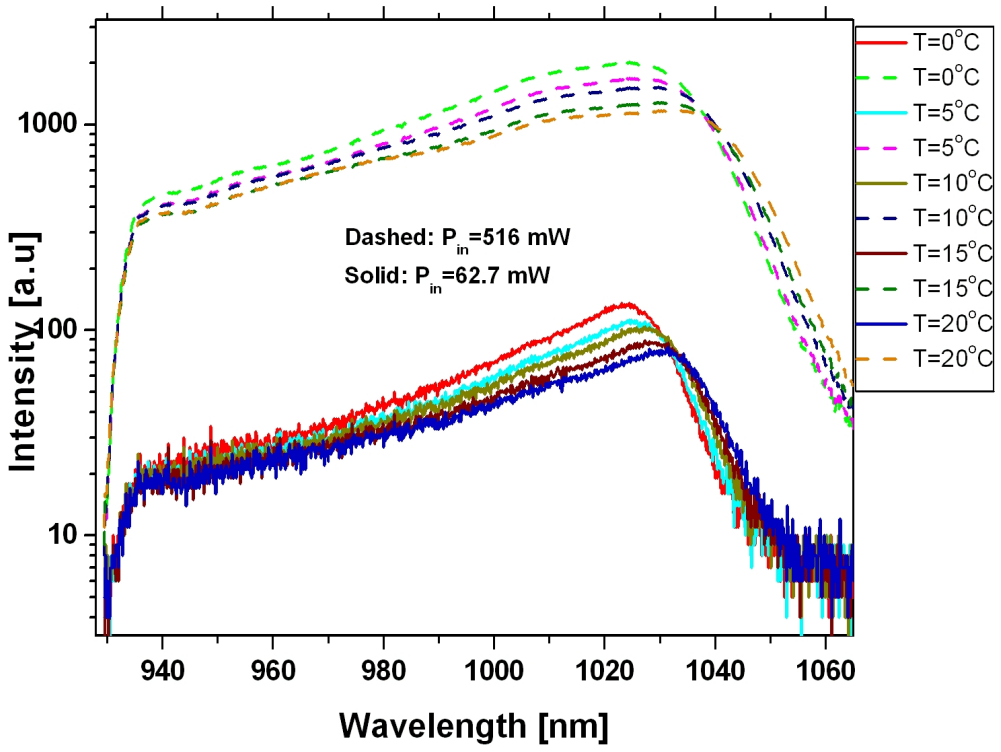

FIGURE 2.8: Edge PL measurements taken from the QT1872D gain chip for pump powers 62.7 mW (solid) and 516 mW (dashed). The data were taken for temperatures 0, 5, 10, 15 and 20^{o}C.

2.3 Continuous Wave Lasing:

The continuous wave operation of the 1872D gain sample was studied by forming a straight 2-mirror cavity and pumping the gain with the fibre coupled laser diode. The aim of the experiments was to find the gain chip with the best possible performance at 1055 nm. The pumped spot radius on the sample was set at 60 μm; two different output couplers, with transmittances of 0.7% and 1.4%, were used with the same radius of curvature of 50 mm. This was done to see the effect of cavity loss on the output power and lasing threshold. The temperature of the gain sample and the input power were varied and the laser spectrum was recorded for each case.

The resulting data for the case of a 0.7% output coupler are shown in Fig 2.10. It is clear that the wavelength of the output gets longer for higher temperature because as temperature increases the band gap energy decreases. A similar argument can be applied to the case of increasing the input pump power. As pump power is increased, the sample temperature increases and so does the carrier density which leads to many-body effects.

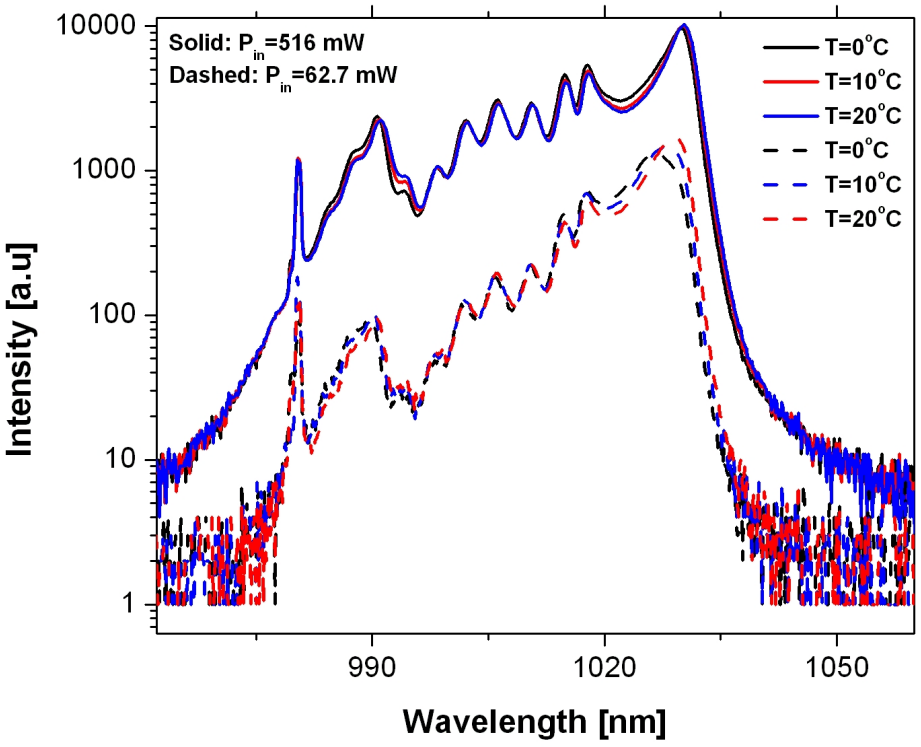

FIGURE 2.9: Top PL graphs of QT1872D for different input powers and temperatures. 62.7 mW (dashed) and 516 mW (solid). The data were taken for temperatures 0^o, 5^o, 10^o, 15^o and 20^oC

However, the wavelength of the output laser varies between 1030.4 nm at 0^o C to 1032.1 nm at 20^o C and varies between 1031 nm for 1.2 W and 1032.2 nm for 0.74 W of input power. This is too short for the fibre amplifier described earlier. To get the laser output wavelength to be longer than 1030 nm, I tried increasing the output coupling (i.e. intracavity loss) of the cavity. This results in higher threshold pump because of the need for greater carrier density for lasing to start. More pumping means higher temperature and hence both these effects will push the temperature further upwards.

Fig 2.11 shows the resulting graphs obtained from the same cavity as before but with a 1.4% output coupler. It can clearly be seen that the laser output has shifted to a longer wavelength region of around 1050 nm. The modulations that can be clearly seen on low temperature graphs are due to the etalon effects associated with working with unpolished gain samples. For warmer temperatures, at 15 and 20^oC, these modulations disappear from the spectrum. This is due to the fact that the intrincsic gain is being tuned away from the flat region of the MCEF into one of the side peaks as shown previously in Fig 2.5 and this means an increased differential gain for one of the modes which takes

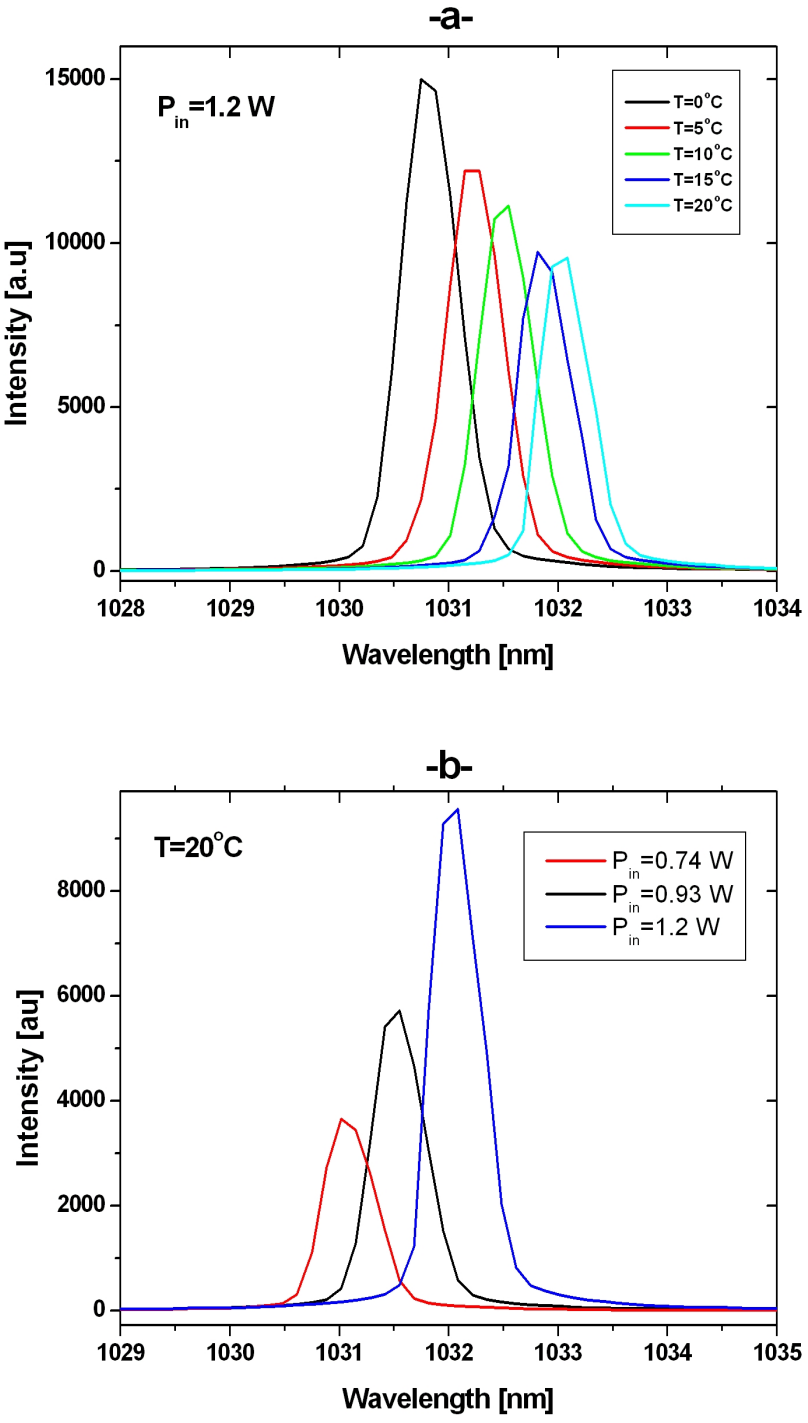

FIGURE 2.10: CW lasing characterisation for the laser with a 0.7% output coupler. Graph a) is for the gain chip temperatures of 0^o, 5^o, 10^o, 15^o and 20^oC with an input power of 1.2 W. Graph b) is for laser operation at 20^oC for three different input powers: 0.74 W, 0.93 W and 1.2 W.

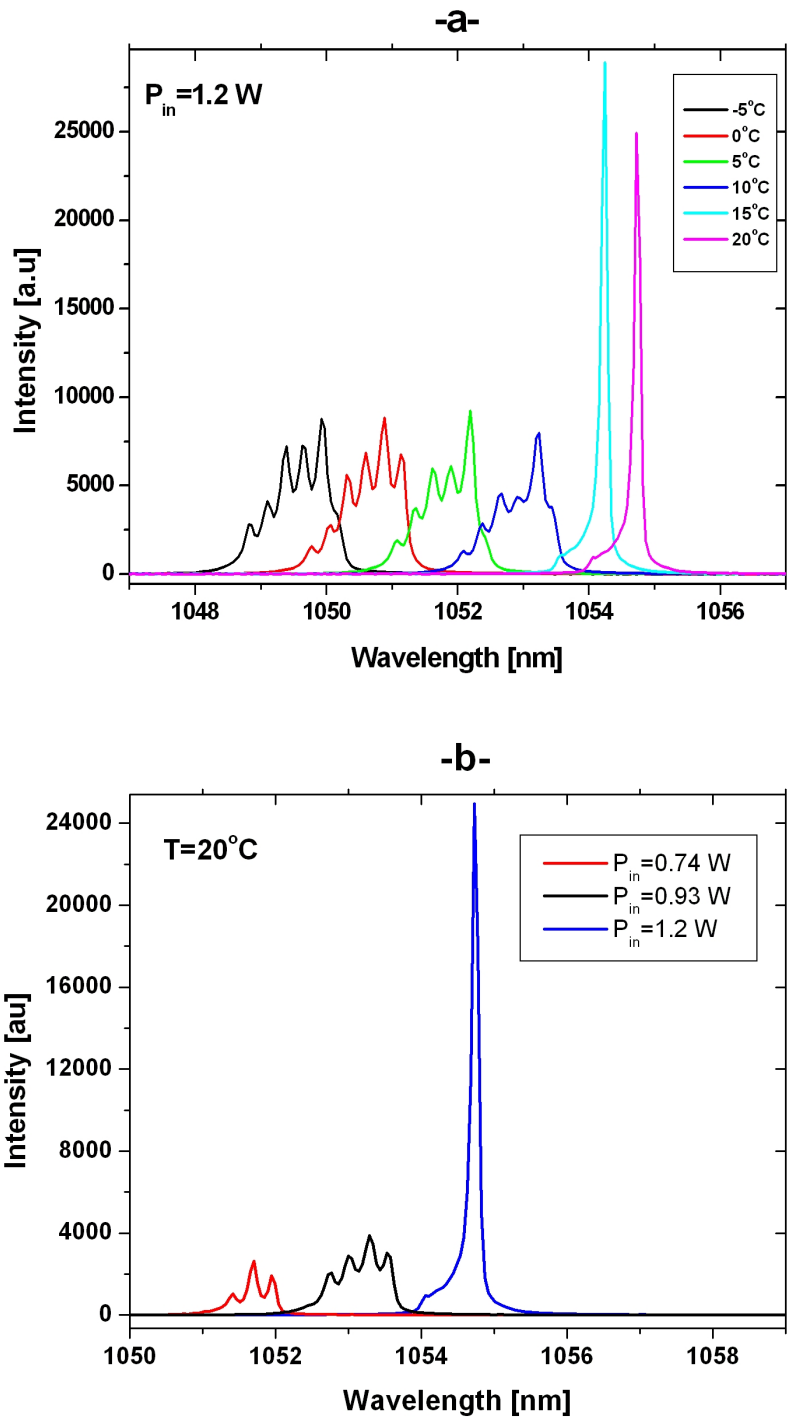

FIGURE 2.11: CW lasing characterisation for the laser with a 1.4% output coupler. Graph c) is for the gain chip temperatures of -5^o, 0^o, 5^o, 10^o, 15^o and 20^oC with an input power of 1.2 W. Graph b) is for laser operation at 20^oC for three different input powers: 0.74 W, 0.93 W and 1.2 W.

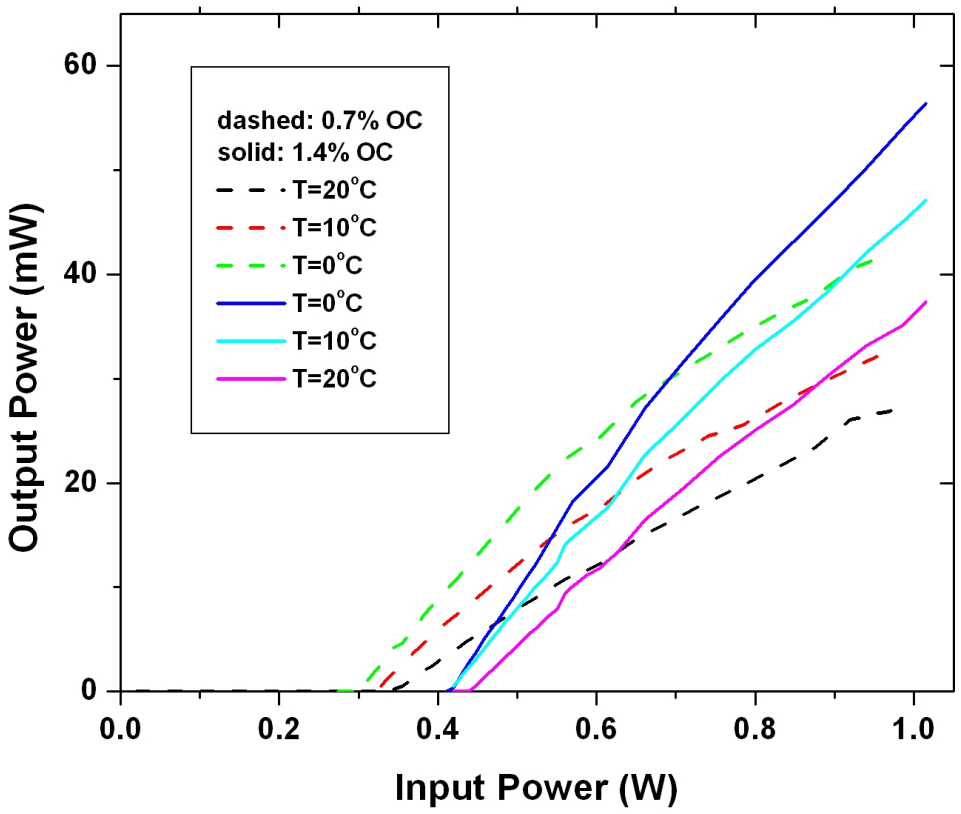

FIGURE 2.12: Power transfer plots of the continuous wave operation of the VECSEL gain sample for two different output couplers. Dashed lines are for cavities with a 0.7% OC and the solid line curves are for 1.4%

over and takes over all the power from the rest of the modes. Despite the fact that the DBR in the wafer had some growth inaccuracies that were noted when the reflectivity spectrum was taken, this sample shows promise when used in conjunction with a high output coupler. Hence, a good starting position has been established before moving on to passively mode-lock this output with a saturable absorber in order to generate sub-picosecond seed pulses for the YDFA system.

The power transfer characteristic was also measured for each of the two output couplers at different temperatures. This is shown in Fig 2.12. It is clear that the threshold increases with temperature and the amount of intracavity loss because the gain needs to surmount the extra loss before lasing starts. Higher output power is obtained with higher output coupling because as mentioned before, the wavelength relation with gain and loss varies with output coupling, and the laser likes to operate at whichever wavelength maximizes its intra-cavity circulating power.

2.4 Passive Mode-locking of a VECSEL

Mode-locked operation of a laser occurs when there is a phase locking of longitudinal cavity modes in the form of a single short pulse in the cavity. There are two ways in which this can be done. The first type is what is called active mode-locking where, for example, an acousto-optic modulator driven electrically to modulate the light amplitude or the pumping mechanism itself is modulated as in asynchronous mode-locking. The second type, which is used in all of this thesis, is called passive mode-locking which does not need an external source of modulation but relies on inclusive components in the cavity to spontaneously start the pulsing operation. The most common type of such a component is a semiconductor saturable absorber.

In a VECSEL cavity, the gain chip can form one end of the cavity opposite an output coupler (OC) in a simple straight cavity or can act as a folding mirror between two arms with a high reflector and an output coupler at each end in a V-cavity configuration. For most mode-locking experiments, a Z-cavity configuration is preferred as it allows for saturation to be set preferentially stronger for saturable absorber.

Passive mode-locking can be divided into two types based on the recovery time of the 'passive' element introduced to the laser. If the recovery time of such an element is shorter than the pulse formed, then it is called a fast saturable absorber. If on the other hand the recovery is slower than the pulse length then it is called a slow saturable absorber. Pulse formation in the first type relies only on the absorber saturation whereas in the second type the gain saturation also plays a role in shaping the pulse. Most SESAMs we worked with are, as mentioned before, slow saturable absorbers; but they can develop a fast element in their recovery due to the Stark effect which will be discussed in Chapters 3 and 4.

2.4.1 Semiconductor Saturable Absorber Mirror (SESAM)

VECSELs can be passively mode-locked by using a SESAM. SESAMs typically incorporate a Bragg mirror at the back of the structure with a saturable absorber at the front. The latter can be, for example, a quantum well or a layer of quantum dots. A typical SESAM structure is shown schematically in Fig 2.13 where the different layers are highlighted by the difference in the bandgap of their composition. It contains a DBR made up of 27 pairs of GaAs/AlAs layers with a GaAs separation layer then an InGaAs quantum well and finally a GaAs window layer.

SESAMs can be grown with the same techniques as VECSEL gain samples with specific properties to operate with different kinds of lasers from solid state lasers to semiconductor lasers. They are slow saturable absorbers meaning they have a recovery time longer than the pulse duration. When added to a laser cavity with a gain material, they introduce a bleachable loss and as a result the laser spontaneously mode-locks.

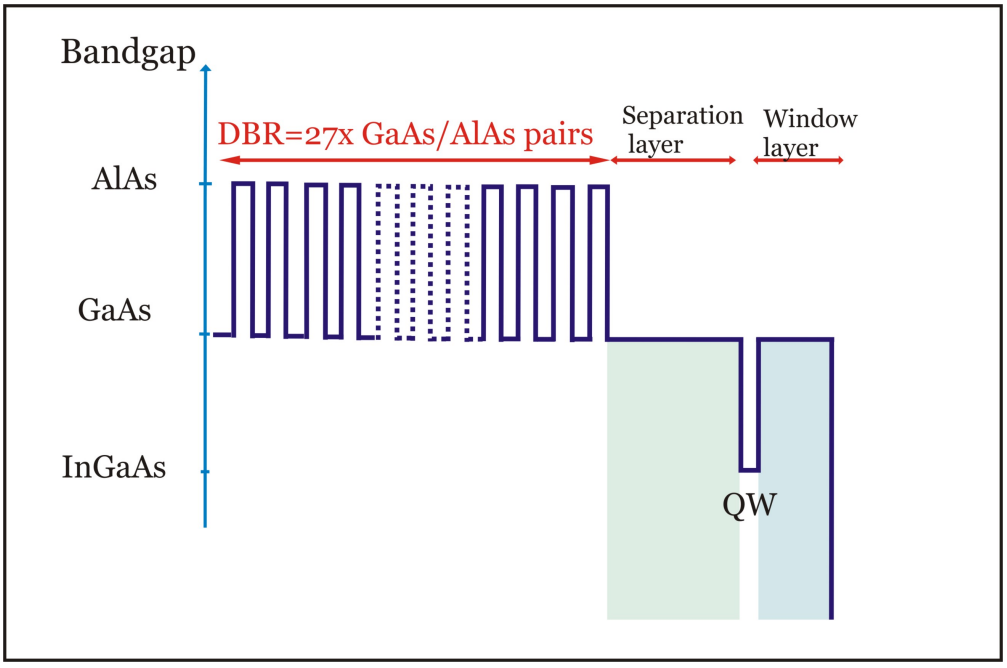

FIGURE 2.13: A schematic of the layers of a SESAM

The properties of a SESAM can be summarised as shown in Fig 2.14. The figure shows how the reflectivity of a SESAM sample changes with pulse fluence which can be defined as the pulse energy incident on its surface per unit area. The characteristics that can describe a SESAM include the saturation fluence (F_{sat}), modulation depth (ΔR), non-saturable loss (ΔR_{ns}) and the recovery time (τ). The saturation fluence of a SESAM is the pulse fluence needed to reduce the saturable loss to 1/e of its initial value. The modulation depth is the maximum change of reflectivity that can be induced by an incident light beam. The recovery time of a SESAM shows how fast the absorption of the SESAM recovers after being bleached. SESAMs with fast recovery time are theoretically able to produce shorter pulses. Finally, the non-saturable losses are the residual losses from incident pulse fluence. These parameters can all be evaluated through a non-linear reflectivity measurements (F_{sat}, ΔR_{ns}, ΔR) and a pump-and-probe experiment (τ).

Our collaborators from ETH Zurich grew our designs using MBE growth techniques. The next objective was to characterise it in our laser cavities and see if it is suitable for

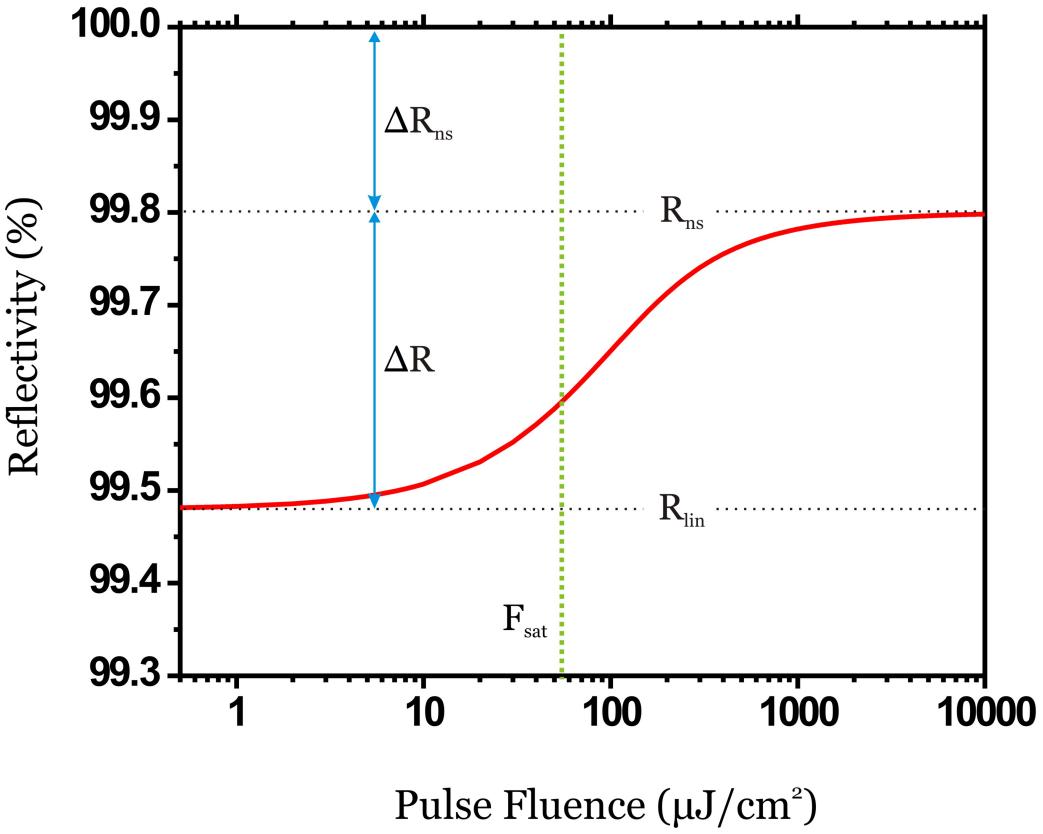

FIGURE 2.14: Reflectivity of a typical SESAM plotted against a logarithmic scale of pulse fluence to highlight the parameters that will dictate the properties of this SESAM

the YDFA. Table 2.1 lists all the measured characteristic of the SESAM sample done using a non-linear reflectivity at Zurich described in [42].

Sample	F_{sat}[J/cm^2]	Δ R	ΔR_{ns}	**absorber**
ES155	13	0.81	0.12	InGaAS

TABLE 2.1: Saturable Absorber Mirror sample grown at ETH Zurich that were characterised.

2.4.2 SESAM-mode-locked VECSEL

Cavities used in mode-locking a VECSEL are designed with the help of a model based on ABCD matrices of beam propagation. A Mathcad program is used to implement these matrices and its output is shown in Fig 2.15. The angles between the arms of the cavity are kept small to avoid astigmatism. Once a cavity repetition rate is chosen,

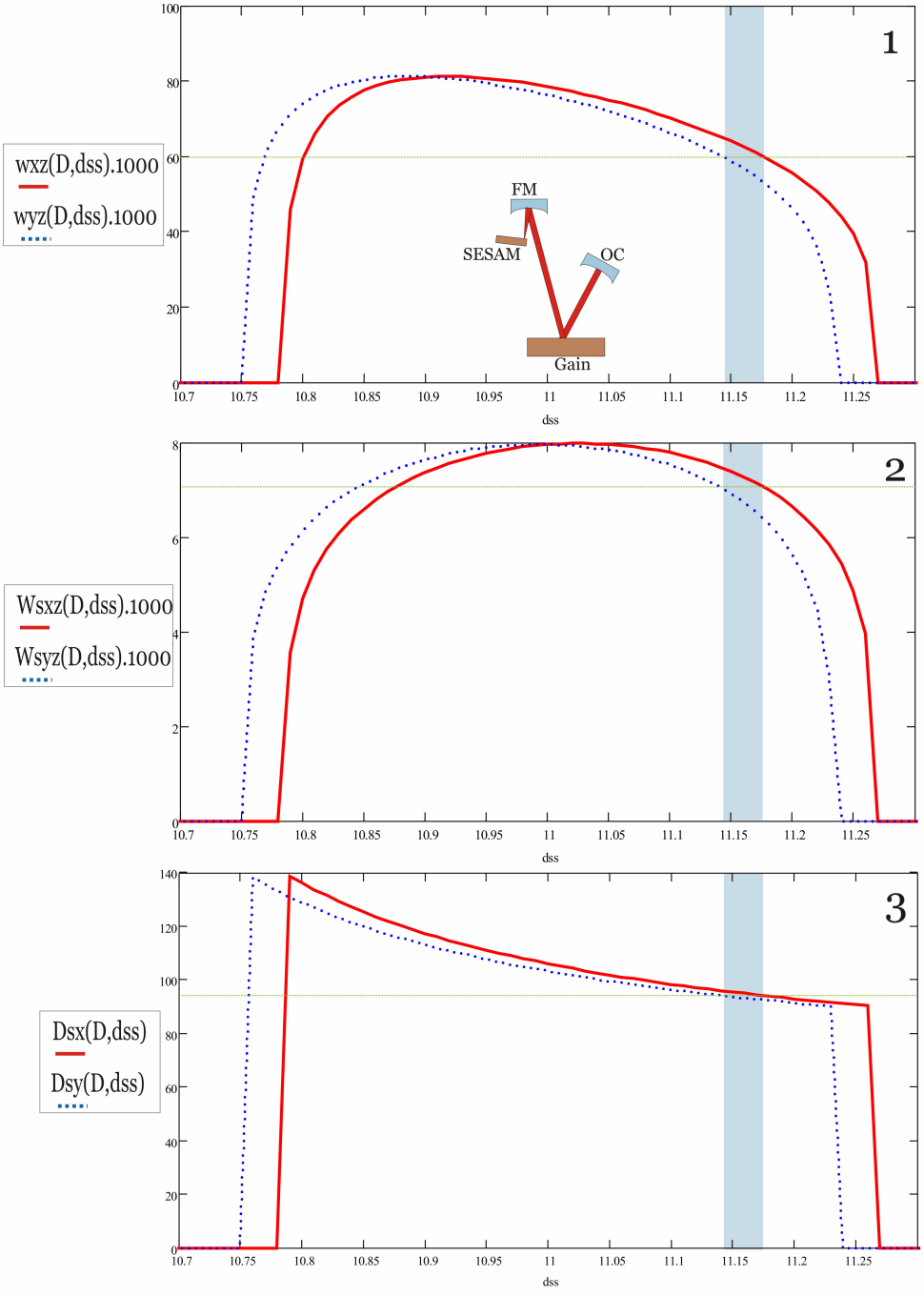

FIGURE 2.15: The output plots of a Mathcad program for designing Z-cavities. FM: Focussing mirror, OC: Output coupler, dss: Distance SESAM-FM, D: Long cavity arm length (OC-Gain-FM), w: spot size. 1)- Mode spot radi (wxz, wyz) on the gain plotted against length of SESAM-FM arm. 2)- Mode spot radi (Wsxz,Wsyz) on the SESAM against length of SESAM-FM arm. 3)- Length of long arm Dsx and Dsy against length of SESAM-FM arm.

the length of the long arm D is set with a suitable OC. Since the cavity mode needs to match the pump spot on the gain, the focussed spot on the gain needs to be 120 μm diameter as highlighted in Fig 2.15-1. The corresponding length of the small arm, dss, is then used to find the spot size on the SESAM from Fig 2.15-2 and also the length of the long arm D from Fig 2.15-3.

The program allows for the correct ratio between beam spots on the gain chip and the SESAM to be accurately set because it is a critical value for mode-locking to be observed. It is important that the cavity should be designed to give larger pulse fluence on the SESAM than on the gain. In the case of the gain spot size, it is limited by the focussing of the pump beam; however one can increase the fluence on the SESAM by focussing hard enough. The SESAMs need to be saturated faster than the gain because it is necessary for a gain window to exist before a pulse is formed.

With a SESAM included in the cavity, the output of the laser may show characteristic properties associated with mode-locking. A host of laboratory equipment is at hand to characterise the output from a VECSEL. The optical spectrum analyser contains a EG& G Princeton Applied Research 0.25-m grating spectrometer plus a 1024-element Si-photodiode array detector with a resolution of around 0.05 nm (model number 1471A). In mode-locked operation, this usually shows a broad stable peak at the emission wavelength. A Femtochrome FR-103 XL dispersion-free intensity autocorrelator with rotating mirrors is used to obtain an autocorrelation trace of the mode-locked pulses. This has various resolution settings with the highest one at 1 fs and utilises a 1 mm thick Lithium Niobate crystal for the second harmonic generation by the pulsed output of the VECSEL. It can also detect multiple pulsing for pulses less than 175 ps apart. An R3273 Advatest RF spectrum analyser alongside a New Focus 1414 IR photo detector with a bandwidth of 25 GHz are used to probe the laser reptition rate and cavity modes. An Infinium DCA-J 86100C fast scope with a resolution of 5.6 ps in sampled mode was also at hand which allowed for the train of pulses to be seen on a time scale. This was used to check whether the laser was operating in a multi-pulsing regime.

An intensity autocorrelation of a typical mode-locked pulse obtained using a SESAM is shown in Fig 2.16. The pulse was 5.81 ps long and was produced at room temperature with the output power from the laser measured to be 20 mW. The optical spectrum of the pulses is also included. It shows a clean Gaussian-like pulse shape with a FWHM of 0.42 nm at a wavelength of 1060.77 nm with a time-bandwidth product of 1.4. The laser cavity has a repetition rate of 1.02 GHz as shown on the RF spectrum included with the autocorrelation.

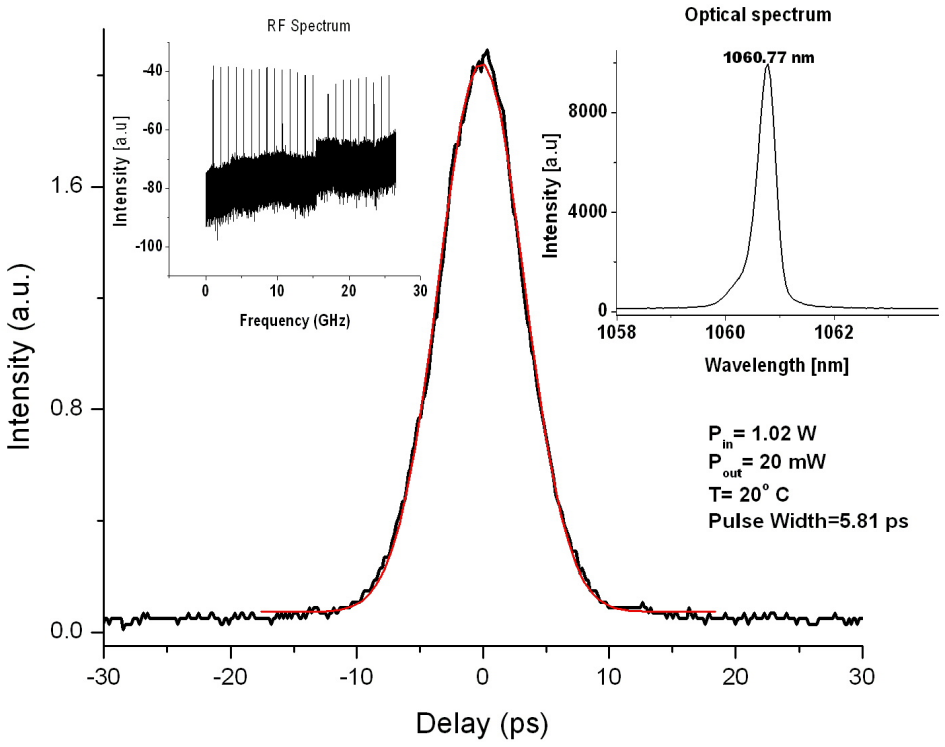

FIGURE 2.16: An intensity autocorrelation of a typical Gaussian pulse from a VECSEL mode-locked using a SESAM along with the optical spectrum (top right) that shows the emission wavelength and the RF spectrum (top left) that shows the pulse train and gives the repetition rate.

2.5 Conclusion

In this chapter, the experimental methods used in this thesis to design and construct CW and mode-locked VECSELs have been shown. In going through the process step by step, the different elements of a VECSEL sample were described and their functions highlighted. An experimental investigation of QT1872D was included to highlight the processes of top and edge PL as well as reflectivity measurements. CW lasing was tested successfully for various pump powers and different temperatures.

Passive mode-locking with a saturable absorber was then discussed. Various cavity designs were made using a computer software and the criteria for obtaining the right spot ratios at the gain and the SESAM was highlighted. Finally, SESAM characteristics have also been discussed and an example of a successful mode-locking was shown with 5.6 ps pulses. These proved not useful in acting as seed pulses since they are not sub-picosecond long but it allowed for a full laser investigation to be carrier out.

Chapter 3

Model Theory of the Stark SESAM

3.1 Introduction

It has been shown that is it is possible to passively mode-lock an InGaAs-based VECSEL with a Semiconductor Saturable Absorber Mirror (SESAM) which contains a single InGaAs quantum well, and to generate transform-limited pulses shorter than 500fs [28]. Since then, a lot of effort has gone into analyzing this result and trying to figure out the mechanism behind the production of these short pulses. A mode-locked VECSEL giving stable transform-limited 260-fs pulses using a SESAM with high modulation depth was demonstrated in [30]. More recently, a 70-fs VECSEL at 1040 nm was reported by Wilcox et al in [31]. This laser had an output that was stable over around 10^{10} roundtrips.

The principle of operation of a SESAM is that pulses with sufficiently large fluence, i.e. energy per unit area, deplete the population of the valence band, bleaching the interband absorption. A great deal of theoretical work has been done on saturable absorbers and the way they shape pulses. The approach introduced by Haus [43, 44, 45] to describe the modelocking process assumes that close to equilibrium, changes to the pulse properties per round trip are small. This approximation is satisfied particularly well by mode-locked VECSELs due to their low gain.

The characteristics of mode-locked VECSELs emitting pulses of 500 fs or shorter indicate that different mechanisms operate compared to those in the picosecond regime, as will be described in Chapter 4. It was postulated by Garnache et al in [28], that the behaviour

of the laser arose from operation of a specially designed SESAM with an intrinsically fast self-absorption modulation in the 'optical Stark regime'.

The Stark effect can be interpreted as the blue shift of an absorbing resonance induced by an intense optical frequency electric field. The magnitude of the optical Stark effect in semiconductor quantum wells has been calculated by Koch in [46, p. 190-195]. He reports that the Stark shift is stronger for the continuum states than the exciton bound states and therefore the excitons becomes more strongly bound.

It was first experimentally reported by Mysyrowicz et al [47] from working with GaAs-based multi-quantum well structure (MQWS). They observed large shifts in the exciton resonances of MQWS when pumped non-resonantly. Tsuda et al reported the differing operating regimes in their work with SESAM-modelocked solid-state lasers. To help understand the different operating regimes, Fig 3.1 taken from Tsuda's work in [48] is presented here. In this figure, the time and wavelength dependence of the transient change in reflectivity of a Saturable Bragg Reflector (SBR), in other words a SESAM, taken from a pump and probe experiment done using a Ti-Sapphire laser is plotted on a 3-D plot. The SBR's quantum well absorption plot is also shown in the figure.

Tsuda reported that each of the pump and probe traces at the five wavelengths have two components, a fast and a slow one. The ratio between the two components varies depending on the excitation wavelength. Below the exciton absorption wavelength, the slow component dominates whereas at wavelengths close or above the exciton absorption, the fast component dominates the responce of the SBR. This behaviour is often seen in mode-locked VECSELs as reported by Garanache et al.

The theoretical analysis of data in [47, 48] describes a non-degenerate pump and probe experiment where intense pump fields strongly detuned to the red of the band gap. This is therefore not directly applicable to our situation. To gain insight into possible mechanisms governing the mode-locking behaviour that we observe, we undertook modelling of intense pulses propagating through an absorbing medium detuned to low energy of the absorbing resonance.

In this chapter, I will lay out the ground work to investigate the behaviour of SESAMs and VECSELs with the help of a numerical model [49, 50]. The focus of the this model is mainly on the light-matter interaction, where the semiconductor absorption is represented in the simplest possible way, as a homogeneous ensemble of two-level atoms with same resonance frequency, ω_r, and the same dephasing time T_2. We treat this ensemble primitively semi-classically and we approximate that the population of the

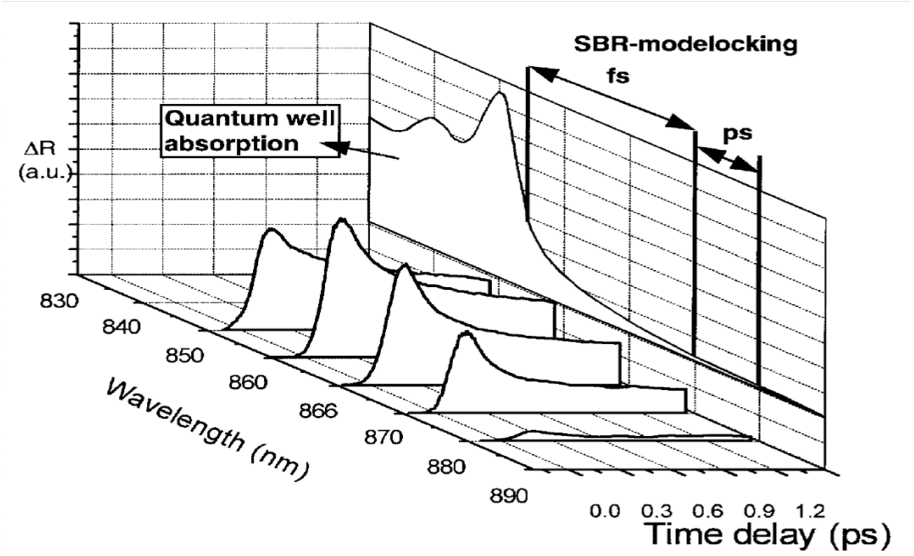

FIGURE 3.1: Transient change in reflectivity, ΔR, of a SESAM as a function of time delay for different pump wavelengths [48]. SBR: Saturable Bragg Reflector.

excited state as negligible. A more sophisticated model would make use of semiconductor Bloch equations but this would highly complicate the model whereas our approach is perfectly fine for transits through an absorber but it is unrealistic for a semiconductor. The primitive nature of the model makes it easily tractable where one can propagate pulses in an instant compared to the huge processing powers needed for running the highly sophisticated finite elements models.

I will then describe some of the experimental results we achieved in our group which are directly connected to this model and present some numerical results obtained from this model and compare them to what we see experimentally.

3.2 Semi-Classical Two Level Atom

At this point I should mention that most of the theoretical work presented in this chapter was developed by Dr G J Daniell at the University of Southampton.

3.2.1 Notation Used

ω_p plasma frequency; effectively it is the number density of 'atoms'

ω_r resonance frequency

$E(t)$ The real physical electric field at a point in space and time

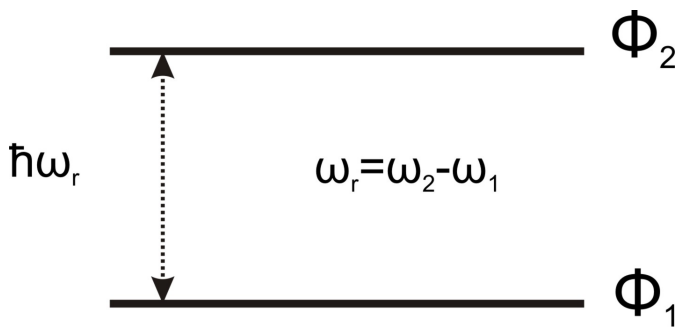

FIGURE 3.2: Diagram of the two level atom configuration used in our model.

$\mathscr{E}(\omega)$ The Fourier spectrum of E. $\mathscr{E}_n$ is used when the spectrum is discrete.

$e(t)$ The complex pulse envelope: $E = \Re[e(t)\ \exp(\mathrm{i}\Omega t)]$.

$\varepsilon(\omega)$ The spectrum of e: $\varepsilon(\omega) = \mathscr{E}(\Omega + \omega)$

Note that large letters refer to the physical field and small letters to the pulse envelope and that ordinary letters are used for functions of time and curly letters for the corresponding spectra.

Similar symbols will be used for the polarisation: $P(t)$, $\mathscr{P}(\omega)$, $p(t)$ and $\wp(\omega)$.

Subscripts '0' and '1' are used for the values of a quantity in the linear theory and the non-linear correction respectively.

Superscripts 'i' and 'o' indicate inputs and outputs of an optical component and '1' and '2' for the direction of incidence of the wave.

3.2.2 Polarisation of a two-level atom

Let $\phi_1(\mathbf{r})$ and $\phi_2(\mathbf{r})$ be the spatial wavefunctions of the two levels as shown in Fig 3.2. The wavefunction for the system can be written

$$\psi(\mathbf{r}, t) = c_1(t)\phi_1(\mathbf{r})\mathrm{e}^{-\mathrm{i}\omega_1 t} + c_2(t)\phi_2(\mathbf{r})\mathrm{e}^{-\mathrm{i}\omega_2 t}$$

Let the Hamiltonian of the atom be $\mathcal{H}_0$ and the potential of the electric field $-ezE(t)$ where $E(t)$ is the real physical electric field in the z direction and e the charge of the charged species on which E acts (e will be negative for electrons).

$\psi(\mathbf{r},t)$ satisfies Schrödinger's time-dependent equation, from which these equations for the time evolution of the complex coefficients $c1$ and $c2$ can be derived:

$$\frac{\mathrm{d}c_1}{\mathrm{d}t} = \mathrm{i}\frac{\mu}{\hbar}\,E(t)\,\mathrm{e}^{-\mathrm{i}\omega_r t}c_2 \tag{3.2.1}$$

$$\frac{\mathrm{d}c_2}{\mathrm{d}t} = \mathrm{i}\frac{\mu}{\hbar}\,E(t)\,\mathrm{e}^{+\mathrm{i}\omega_r t}c_1 \tag{3.2.2}$$

where the optical dipole matrix element is given by

$$\mu = \int \phi_1^*(ez)\phi_2\,\mathrm{d}^3\mathbf{r}$$

The expectation value of the dipole moment of the atom is

$$p = \int \psi^*(ez)\psi\,\mathrm{d}^3\mathbf{r} = \mu[c_1^*c_2\mathrm{e}^{-\mathrm{i}\omega_r t} + c_1c_2^*\mathrm{e}^{+\mathrm{i}\omega_r t}] = p_1 + p_2 \tag{3.2.3}$$

where p_1 and p_2 describe the dipole moments of the the two levels. We also define the population inversion

$$n = c_2c_2^* - c_1c_1^*. \tag{3.2.4}$$

From the equations for the evolution of c_1 and c_2 we get

$$\dot{p_1} = \mu[\dot{c_1}^*c_2 + c_1^*\dot{c_2} - \mathrm{i}\omega_r c_1^*c_2]\mathrm{e}^{-\mathrm{i}\omega_r t} = -\mathrm{i}\omega_r p_1 - \mathrm{i}\frac{\mu^2 E(t)}{\hbar}n$$

Since $p_2 = p_1^*$

$$\dot{p_2} = +\mathrm{i}\omega_r p_2 + \mathrm{i}\frac{\mu^2 E(t)}{\hbar}n$$

The evolution of the dipole moment satisfies

$$\dot{p} = \dot{p}_2 + \dot{p}_1 = \mathrm{i}\omega_r(p_2 - p_1)$$

At this stage we need to introduce damping. We use the same notation, p_1, p_2 and n for ensemble averages as previously applied to single atoms. We make p relax to zero on a timescale T_2. The population inversion will relax on the much longer timescale T_1. This is so long compared with the pulse we are considering that its effect during the pulse can be ignored; however it is not long compared with the time between pulses. It follows that at the start of a pulse the medium is in a Boltzmann equilibrium state with almost all the atoms in the lower level, so effectively $n = -1$. Further work by G. J. Daniell has

removed this restriction but at the expense of a greatly increased computation times as a result of the long T_1 time scales now involved. The work presented here is valid in a regime where the E-field is large enough to produce non-linear effects but not so large to invalidate the $n = -1$ approximation. With this modification we write

$$\dot{p} = \mathrm{i}\omega_r(p_2 - p_1) - \frac{p}{T_2}$$

$$\ddot{p} = \mathrm{i}\omega_r(\dot{p_2} - \dot{p_1}) - \frac{\dot{p}}{T_2} = -\omega_r^2 p - \frac{\dot{p}}{T_2} - \frac{2\omega_r\mu^2 E(t)}{\hbar}n$$

In order to eliminate n we differentiate again to get

$$\dddot{p} = -\omega_r^2\dot{p} - \frac{\ddot{p}}{T_2} - \frac{2\omega_r\mu^2}{\hbar}[\dot{n}E + n\dot{E}]$$

Although we can put $n = -1$ we must not ignore $\dot{n}$ so we calculate

$$\dot{n} = \dot{c_2}c_2^* + c_2\dot{c_2}^* - \dot{c_1}c_1^* - c_1\dot{c_1}^* = \frac{2\mathrm{i}E(t)}{\hbar}(p_2 - p_1) = \frac{2E(t)}{\hbar\omega_r}\left[\dot{p} + \frac{p}{T_2}\right].$$

Substituting the expression for $\dot{n}$ into the expression for $\dddot{p}$ yields the result

$$\dddot{p} = -\omega_r^2\dot{p} - \frac{\ddot{p}}{T_2} - \frac{4\mu^2[E(t)^2]}{\hbar^2}\left[\dot{p} + \frac{p}{T_2}\right] + \frac{2\omega_r\mu^2}{\hbar}\dot{E} \tag{3.2.5}$$

which is independent of n.

The polarisation of the medium with N atoms per unit volume is just $P = Np$. If we ignore the non-linear term in E^2 we get an equation relating P and E of the form

$$\dddot{P} + 2\alpha\ddot{P} + \omega_r^2\dot{P} = \omega_p^2\epsilon_0\dot{E}$$

where we have used the plasma frequency, ω_p, by $\omega_p^2 = 2Ne\mu^2/\hbar\epsilon_0$ as a convenient parameter in place of the number density N and the absorption width is determined by $\alpha = 1/2T_2$. This is just the time derivative of the usual Lorentz equation relating P and E. When we are modelling delocalised carriers in a semiconductor as if they were fixed electrons in a two-level atom, the number density , N, does not correspond to a physical property of the semiconductor but the plasma frequency does relate to the strength of the absorption.

The nonlinear terms in this equation are determined by the magnitude of the electric field relative to E_{stark} where $E_{\text{stark}} = \hbar\omega_r/2\mu$. The generalisation of the Lorentz equation 3.2.5 to include the Stark effect is then given by

$$\dddot{P} + 2\alpha[\ddot{P} + \omega_r^2 \left(\frac{E(t)}{E_{\text{stark}}}\right)^2 P] + \omega_r^2[1 + \left(\frac{E(t)}{E_{\text{stark}}}\right)^2]\dot{P} = \omega_p^2\epsilon_0\dot{E} \tag{3.2.6}$$

where there are now two terms with $(E(t)/E_{\text{stark}})^2$. The first of which is a power broadening term whilst the second one represents a blue shift in ω_r. These two terms collectively represent what we think of qualitatively as the optical Stark effect.

To avoid writing E_{stark} throughout the rest of this chapter we will always measure electric fields in units of E_{stark}. Since this equation is linear in P we can always measure P in units of $P_{\text{stark}} = \epsilon_0 E_{\text{stark}}$ so the modified Lorentz equation that is used in the model is

$$\dddot{P} + 2\alpha[\ddot{P} + \omega_r^2 E(t)^2 P] + \omega_r^2[1 + E(t)^2]\dot{P} = \omega_p^2\dot{E} \tag{3.2.7}$$

3.2.3 Transmission through a thin layer with Stark effect

The optical Stark effect only occurs within a single quantum well, which is thin compared to the wavelength. In our lasers the InGaAs quantum well in the SESAM is 8 nm thick whilst the wavelength inside is about 330 nm. This fact simplifies the treatment of nonlinearity. In this section, we will derive the boundary conditions used in the model. We will extract the transmission and reflection coefficients that will be used to determine the fields inside and outside the Stark layer as shown in Fig 3.3.

3.2.3.1 Boundary Conditions

The thin layer is on-linear so we have to consider inputs from both sides simultaneously. We have to consider first the transmission of a wave through a layer of *linear* dielectric. consider a wave be incident on an interface at $z = 0$ and represented in the form

$$E^{(i1)}(t, z) = \int \mathscr{E}^{(i1)}(\omega)\ \mathrm{e}^{\mathrm{i}(\omega t - k(\omega)z)}\ \mathrm{d}\omega$$

The superscript i means 'input' and the '1' means from the left side. We similarly define $\mathscr{E}^{(i2)}$ for the wave incident from the right and $\mathscr{E}^{(o1)}$ and $\mathscr{E}^{(o2)}$ for the 'output' waves. For $\mathscr{E}^{(i2)}$ and $\mathscr{E}^{(o1)}$ the sign of k is reversed.

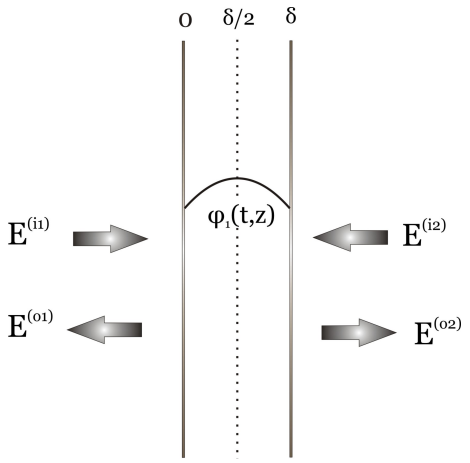

FIGURE 3.3: A schematic figure of the quantum well in the SESAM as a thin absorbing layer. The arrows show an input $\mathbf{E}^{(i1)}$ and output $\mathbf{E}^{(o1)}$ waves from the left side and input $\mathbf{E}^{(i2)}$ and output $\mathbf{E}^{(o2)}$ from the right side. The layers have a thickness δ. The variation of the field inside the layer is $\phi_1(t,z)$.

The E and B fields satisfy the following boundary conditions: The component of the E-field in the plane of the interface and the component of the B-field perpendicular to the plane are continuous. Then, from the Maxwell equation curl$\mathbf{E} = -\dot{\mathbf{B}}$ the second of these can be replaced by the continuity of $\partial\mathbf{E}/\partial z$.

Let us suppose for the time being that the response of the two-level atoms is linear. We define the resulting field inside the layer as $\phi_0(t,z)$, which we also write as a Fourier integral of a spectrum $\Phi_0(\omega,z)$. At $z=0$ the continuity of E gives

$$\mathscr{E}^{(i1)}(\omega) + \mathscr{E}^{(o2)}(\omega) = \Phi_0(\omega,0) \tag{3.2.8}$$

and the continuity of $\partial E/\partial z$ gives

$$-\,\mathrm{i}k\ \mathscr{E}^{(i1)}(\omega) + \mathrm{i}k(\omega)\ \mathscr{E}^{(o2)}(\omega) = \Phi_0'(\omega,0) \tag{3.2.9}$$

where $\Phi_0'(\omega,z) = \partial\Phi_0(\omega,z)/\partial z$.

We can eliminate $\mathscr{E}^{(o2)}$ from equations (3.2.8) and (3.2.9) giving

$$2\mathrm{i}k\ \mathscr{E}^{(i1)}(\omega) = \mathrm{i}k\ \Phi_0(\omega,0) - \Phi_0'(\omega,0) \tag{3.2.10}$$

At the far side of the layer, $z=\delta$,

$$\mathscr{E}^{(o1)}(\omega) + \mathscr{E}^{(i2)}(\omega) = \Phi_0(\omega, \delta) \tag{3.2.11}$$

and

$$-\,\mathrm{i}k\ \mathscr{E}^{(o1)}(\omega) + \mathrm{i}k(\omega)\ \mathscr{E}^{(i2)}(\omega) = \Phi_0'(\omega, \delta) \tag{3.2.12}$$

and together these imply that

$$2\mathrm{i}k\ \mathscr{E}^{(i2)}(\omega) = \mathrm{i}k\ \Phi_0(\omega, \delta) + \Phi_0'(\omega, \delta) \tag{3.2.13}$$

3.2.3.2 Non-linearity and Boundary Conditions

Now imagine that we turn on the non-linearity of the medium, keeping the same values for $\mathscr{E}^{(i1)}$ and $\mathscr{E}^{(i2)}$, and let the field inside the layer change from Φ_0 to $\Phi_0 + \Phi_1$. Because $\mathscr{E}^{(i1)}$ and $\mathscr{E}^{(i2)}$ are fixed from (3.2.10) and (3.2.13) we must have

$$\mathrm{i}k\ \Phi_1(\omega, 0) - \Phi_1'(\omega, 0) = 0 \tag{3.2.14}$$

and

$$\mathrm{i}k\ \Phi_1(\omega, \delta) + \Phi_1'(\omega, \delta) = 0 \tag{3.2.15}$$

3.2.3.3 The approximation of a very thin layer

We are going to expand $\Phi_1(\omega, z)$ in terms of δ/λ. By making use of the fact that the thickness of the layer, δ, is much less than a wavelength, we are limiting it to second order terms so that $\Phi_1'(\omega, z)$ varies *linearly*.

Let $\mathcal{E}_1$, $\mathcal{E}_1'$ and $\mathcal{E}_1''$ denote the field and its derivatives in the *centre* of the layer so that

$$\Phi_1(\omega, 0) = \mathcal{E}_1 - \tfrac{1}{2}\delta\mathcal{E}_1' + \tfrac{1}{8}\delta^2\mathcal{E}_1'' \tag{3.2.16}$$

$$\Phi_1(\omega, \delta) = \mathcal{E}_1 + \tfrac{1}{2}\delta\mathcal{E}_1' + \tfrac{1}{8}\delta^2\mathcal{E}_1'' \tag{3.2.17}$$

$$\Phi_1'(\omega,0) = \mathcal{E}_1' - \tfrac{1}{2}\delta\mathcal{E}_1'' \tag{3.2.18}$$

$$\Phi_1'(\omega,\delta) = \mathcal{E}_1' + \tfrac{1}{2}\delta\mathcal{E}_1'' \tag{3.2.19}$$

Our two equations,(3.2.14) and (3.2.15), now read

$$\mathrm{i}k[\mathcal{E}_1 - \tfrac{1}{2}\delta\mathcal{E}_1' + \tfrac{1}{8}\delta^2\mathcal{E}_1''] = \mathcal{E}_1' - \tfrac{1}{2}\delta\mathcal{E}_1''; \tag{3.2.20}$$

$$\mathrm{i}k[\mathcal{E}_1 + \tfrac{1}{2}\delta\mathcal{E}_1' + \tfrac{1}{8}\delta^2\mathcal{E}_1''] = -[\mathcal{E}_1' + \tfrac{1}{2}\delta\mathcal{E}_1'']; \tag{3.2.21}$$

and adding (3.2.20) and (3.2.21) we get

$$2\mathrm{i}k\mathcal{E}_1 + \tfrac{1}{4}\mathrm{i}k\delta^2\mathcal{E}_1'' = -\delta\mathcal{E}_1'', \tag{3.2.22}$$

which when rearranged gives

$$\mathcal{E}_1'' = \frac{-2\mathrm{i}k\mathcal{E}_1}{\delta(1+\mathrm{i}k\delta/4)} \simeq -\frac{2\mathrm{i}k\mathcal{E}_1}{\delta}\left(1 - \tfrac{1}{4}\mathrm{i}k\delta\right). \tag{3.2.23}$$

Also subtracting equation (3.2.21) from (3.2.20) yields that

$$(2+\mathrm{i}k\delta)\mathcal{E}_1' = 0 \tag{3.2.24}$$

so $\mathcal{E}_1' = 0$, a result we shall need later.

We have so far not used Maxwell's equations inside the layer. The electric field satisfies the wave equation in the form

$$\frac{\partial^2 E}{\partial z^2} = \frac{1}{c^2}\left[\frac{\partial^2 E}{\partial t^2} + \frac{1}{\epsilon_0}\frac{\partial^2 P}{\partial t^2}\right]$$

although P is a non-linear function of E. We split E and P into linear and non-linear parts $E_0 + E_1$ and $P_0 + P_1$ where E_0 and P_0 are related by a simple susceptibility derived from

$$\mathscr{E}_0''(\omega) = -\frac{\omega^2}{c^2}\left(\mathscr{E}_0(\omega) + \mathscr{P}_0(\omega)\right)$$

and E_1 and P_1, which arise from the non-linearity, satisfy

$$\mathscr{E}_1''(\omega) = -\frac{\omega^2}{c^2}\left(\mathscr{E}_1(\omega) + \mathscr{P}_1(\omega)\right).$$

We can apply this equation to the fields at the centre of the layer where we used the symbol $\mathcal{E}_1$ for the change in the electric field and introduced a corresponding polarisation $\mathcal{P}_1$ we have

$$\mathcal{E}_1'' = -\frac{\omega^2}{c^2}(\mathcal{E}_1 + \mathcal{P}_1),$$

and the result of applying this to the boundary conditions from equation (3.2.22), it gives

$$2\mathrm{i}k\mathcal{E}_1 = [-1 + \tfrac{1}{4}\mathrm{i}k\delta]\frac{\delta\omega^2}{c^2}(\mathcal{E}_1 + \mathcal{P}_1).$$

This equation relates the two fields $\mathcal{E}_1$ and $\mathcal{P}_1$ which are also connected by the modified Lorentz equation with the linear field, so we solve them to determine $\mathcal{E}_1$.

In practice δ is sufficiently small and after a Taylor series expansion we approximate to first order that

$$\mathcal{E}_1 = -\frac{\mathrm{i}\delta\omega^2}{2kc^2}\mathcal{P}_1. \tag{3.2.25}$$

3.2.3.4 Calculation of Standard Reflection and Transmission Coefficients

The standard reflection and transmission coefficients for a thin layer will be calculated in this section. This is done to keep a consistent notation throughout the chapter. Using the linear wave equation for $\Phi_1(\omega, z)$ we have a solution of the form

$$\Phi_0(\omega, z) = \mathscr{A}(\omega)\ \mathrm{e}^{-\mathrm{i}k'(z-\delta/2)} + \mathscr{B}(\omega)\ \mathrm{e}^{+\mathrm{i}k'(z-\delta/2)}$$

with the boundary equations

$$2\mathrm{i}k\ \mathscr{E}^{(i1)}(\omega) = \mathrm{i}k\ \Phi_0(\omega, 0) - \Phi_0'(\omega, 0),$$

$$2\mathrm{i}k\ \mathscr{E}^{(i2)}(\omega) = \mathrm{i}k\ \Phi_0(\omega, \delta) + \Phi_0'(\omega, \delta),$$

give

$$2\mathrm{i}k\ \mathscr{E}^{(i1)} = \mathrm{i}k\ (\mathscr{A}\ \mathrm{e}^{+} + \mathscr{B}\ \mathrm{e}^{-}) - \mathrm{i}k'\ (-\mathscr{A}\ \mathrm{e}^{+} + \mathscr{B}\ \mathrm{e}^{-}),$$

$$2\mathrm{i}k\ \mathscr{E}^{(i2)} = \mathrm{i}k\ (\mathscr{A}\ \mathrm{e}^{-} + \mathscr{B}\ \mathrm{e}^{+}) + \mathrm{i}k'\ (-\mathscr{A}\ \mathrm{e}^{-} + \mathscr{B}\ \mathrm{e}^{+}),$$

where we have introduced the abbreviations $\mathrm{e}^{\pm} = \exp(\pm \mathrm{i}k'\delta/2)$.

These lead to expressions for $\mathscr{A}$ and $\mathscr{B}$:

$$\mathscr{A} = \frac{2k(k+k')\ \mathrm{e}^{+}\mathscr{E}^{(i1)} - 2k(k-k')\ \mathrm{e}^{-}\mathscr{E}^{(i2)}}{(k+k')^2 \exp(+\mathrm{i}k'\delta) - (k-k')^2 \exp(-\mathrm{i}k'\delta)}$$

$$\mathscr{B} = \frac{2k(k+k')\ \mathrm{e}^{+}\mathscr{E}^{(i2)} - 2k(k-k')\ \mathrm{e}^{-}\mathscr{E}^{(i1)}}{(k+k')^2 \exp(+\mathrm{i}k'\delta) - (k-k')^2 \exp(-\mathrm{i}k'\delta)}$$

At this stage it is convenient to introduce the quantities

$$T_0 = \frac{4kk'}{(k'+k)^2 \exp(+\mathrm{i}k'\delta) - (k -' k)^2 \exp(-\mathrm{i}k'\delta)} \tag{3.2.26}$$

$$R_0 = \frac{2\mathrm{i}(k^2 - k'^2)\sin(k'\delta)}{(k+k')^2 \exp(+\mathrm{i}k'\delta) - (k-k')^2 \exp(-\mathrm{i}k'\delta)} \tag{3.2.27}$$

so that

$$\mathscr{A} = \frac{T_0}{2k'}\left[(k+k')\ \mathrm{e}^{+}\mathscr{E}^{(i1)} - (k-k')\ \mathrm{e}^{-}\mathscr{E}^{(i2)}\right]$$

$$\mathscr{B} = \frac{T_0}{2k'}\left[-(k+k')\ \mathrm{e}^{-}\mathscr{E}^{(i1)} + (k-k')\ \mathrm{e}^{+}\mathscr{E}^{(i2)}\right]$$

The output fields are

$$2k\ \mathscr{E}^{(o1)} = \mathrm{i}k\ \Phi_0(\omega,\delta) - \Phi_0'(\omega,\delta) = (k+k')\mathscr{A}\ \mathrm{e}^{-} + (k-k')\mathscr{B}\ \mathrm{e}^{+}$$

$$= \frac{T_0}{2k'}\left[(k+k')^2\mathscr{E}^{(i1)} - (k^2-k'^2)\mathrm{e}^{-2}\mathscr{E}^{(i2)} - (k-k')^2\mathscr{E}^{(i1)} + (k^2-k'^2)\mathrm{e}^{+2}\mathscr{E}^{(i2)}\right]$$

$$\mathscr{E}^{(o1)} = T_0\mathscr{E}^{(i1)} + R_0\mathscr{E}^{(i2)} \tag{3.2.28}$$

$$2k\ \mathscr{E}^{(o2)} = \mathrm{i}k\ \Phi_0(\omega,0) + \Phi_0'(\omega,0) = (k-k')\mathscr{A}\ \mathrm{e}^{+} + (k+k')\mathscr{B}\ \mathrm{e}^{-}$$

$$= \frac{T_0}{2k'}\left[(k^2-k'^2)\mathscr{E}^{(i1)}\mathrm{e}^{+2} - (k-k')^2\mathscr{E}^{(i2)} - (k^2-k'^2)\mathscr{E}^{(i1)}\mathrm{e}^{-2} + (k+k')^2\mathscr{E}^{(i2)}\right]$$

$$\mathscr{E}^{(o2)} = T_0\mathscr{E}^{(i1)} + R_0\mathscr{E}^{(i2)} \tag{3.2.29}$$

so T_0 and R_0 are the linear transmission and reflection coefficients of the layer. Note that the phase reference for $\mathscr{E}^{(i1)}$ and $\mathscr{E}^{(o2)}$ is the left hand side of the layer whereas for $\mathscr{E}^{(o1)}$ and $\mathscr{E}^{(i2)}$ it is the right hand side. In the case where $k' = k$ then $T_0 = \exp(\mathrm{i}k\delta)$.

3.2.3.5 Non-linear corrections

The corrections to these expressions, equations (3.2.28) and (3.2.29), allowing for non-linearity are

$$\mathscr{E}^{(o1)} = T_0\mathscr{E}^{(i1)} + R_0\mathscr{E}^{(i2)} + \tfrac{1}{2}\left[\Phi_1(\omega,\delta) - \frac{1}{\mathrm{i}k}\Phi_1'(\omega,\delta)\right],$$

$$\mathscr{E}^{(o2)} = R_0\mathscr{E}^{(i1)} + T_0\mathscr{E}^{(i2)} + \tfrac{1}{2}\left[\Phi_1(\omega,0) + \frac{1}{\mathrm{i}k}\Phi_1'(\omega,0)\right].$$

Using equations (3.2.16) through to (3.2.19) gives

$$\mathscr{E}^{(o1)} = T_0\mathscr{E}^{(i1)} + R_0\mathscr{E}^{(i2)} + \tfrac{1}{2}[\mathcal{E}_1 + \tfrac{1}{2}\delta\mathcal{E}_1' + \tfrac{1}{8}\delta^2\mathcal{E}_1''] - \frac{1}{2\mathrm{i}k}[\mathcal{E}_1' + \tfrac{1}{2}\delta\mathcal{E}_1'']$$

and

$$\mathscr{E}^{(o2)} = R_0\mathscr{E}^{(i1)} + T_0\mathscr{E}^{(i2)} + \tfrac{1}{2}[\mathcal{E}_1 - \tfrac{1}{2}\delta\mathcal{E}_1' + \tfrac{1}{8}\delta^2\mathcal{E}_1''] + \frac{1}{2\mathrm{i}k}[\mathcal{E}_1' - \tfrac{1}{2}\delta\mathcal{E}_1''].$$

Using the results above $\mathcal{E}_1' = 0$ and

$$\mathcal{E}_1'' = -\frac{2\mathrm{i}k\mathcal{E}_1}{\delta}\left(1 - \tfrac{1}{4}\mathrm{i}k\delta\right)$$

we get

$$\mathscr{E}^{(o1)} = T_0\mathscr{E}^{(i1)} + R_0\mathscr{E}^{(i2)} + (1 - \tfrac{1}{2}\mathrm{i}k\delta)\mathcal{E}_1,$$

$$\mathscr{E}^{(o2)} = R_0\mathscr{E}^{(i1)} + T_0\mathscr{E}^{(i2)} + (1 - \tfrac{1}{2}\mathrm{i}k\delta)\mathcal{E}_1$$

To a reasonable approximation we can use the zero-thickness layer again, we can neglect terms linear in, δ, then we get

$$\mathscr{E}^{(o1)} = T_0\mathscr{E}^{(i1)} + R_0\mathscr{E}^{(i2)} + \mathcal{E}_1 \tag{3.2.30}$$

$$\mathscr{E}^{(o2)} = R_0\mathscr{E}^{(i1)} + T_0\mathscr{E}^{(i2)} + \mathcal{E}_1 \tag{3.2.31}$$

The calculation of $\mathcal{E}_1$ needs the field at the centre of the layer

$$\mathcal{E}_0 = \Phi(\omega, \tfrac{1}{2}\delta) = \mathscr{A} + \mathscr{B} = \frac{T_0}{2k'}\left[(k+k')\mathrm{e}^{+} - (k-k')\mathrm{e}^{-}\right](\mathscr{E}^{(i1)} + \mathscr{E}^{(i2)}) \tag{3.2.32}$$

On substituting T_0 this becomes

$$\mathcal{E}_0 = \frac{2k}{(k+k')\mathrm{e}^{+\mathrm{i}k'\delta/2} + (k-k')\mathrm{e}^{-\mathrm{i}k'\delta/2}}(\mathscr{E}^{(i1)} + \mathscr{E}^{(i2)}) \tag{3.2.33}$$

For the zero-thickness layer this becomes

$\mathcal{E}_0 = \mathscr{E}^{(i1)} + \mathscr{E}^{(i2)}$.

3.2.3.6 Summary of the calculation

- The linear reflection and transmission coefficients are given by R_0 and T_0 in equations 3.2.26 and 3.2.27.
- The unperturbed electric field at the centre of the layer is $\mathcal{E}_0 = \mathscr{E}^{(i1)} + \mathscr{E}^{(i2)}$.
- The non-linear contributions to the field at the centre are related by

  $$\mathcal{E}_1 = -\frac{\mathrm{i}\delta\omega^2}{kc^2}\mathcal{P}_1$$

  and the modified Lorentz equation 3.2.7.

3.2.3.7 Modification for pulse propagation

If we represent the electric field of a pulse as the product of a carrier frequency which is a single Fourier component and a slowly varying envelope function, then the Fourier transform of the envelope function is then the same as the Fourier transform of the pulse only shifted to the carrier frequency. This is known as the Fourier Shift Theorem.

When we consider the propagation of a pulse and are not interested in the carrier we shift the centre of all spectra to the carrier frequency. We replace ω by $\Omega + \omega$ so that now ω refers to the Fourier components of the pulse envelope. The symbol ε will be used for these shifted spectra.

The physical electric field is then given by

$$E(t,z) = \Re\left\{\int \varepsilon(\omega)\mathrm{e}^{\mathrm{i}[(\Omega+\omega)t-k(\Omega+\omega)z]}\,\mathrm{d}\omega\right\}$$

The equations relating the input and output fields showing the explicit frequency dependence, using equations (3.2.30) and (3.2.31), are

$$\varepsilon^{(o1)}(\omega) = T_0(\Omega+\omega)\varepsilon^{(i1)}(\omega) + R_0(\Omega+\omega)\varepsilon^{(i2)}(\omega) + \varepsilon_1(\omega), \tag{3.2.34}$$

$$\varepsilon^{(o2)}(\omega) = R_0(\Omega+\omega)\varepsilon^{(i1)}(\omega) + T_0(\Omega+\omega)\varepsilon^{(i2)}(\omega) + \varepsilon_1(\omega), \tag{3.2.35}$$

where we have written $\varepsilon_1(\omega) = \mathcal{E}_1(\Omega+\omega)$. By the same convention, we also have the formula

$$\varepsilon_0(\omega) = \mathcal{E}_0(\Omega+\omega) = \varepsilon^{(i1)}(\omega) + \varepsilon^{(i2)}(\omega) \tag{3.2.36}$$

and from equation (3.2.25) we get

$$\varepsilon_1(\omega) = -\frac{\mathrm{i}\delta(\Omega+\omega)^2}{2kc^2}\wp_1(\omega). \tag{3.2.37}$$

The linear Lorentz equation that relates ε_0 and $\wp_0$

$$\wp_0(\omega) = \chi(\Omega+\omega)\varepsilon_0(\omega), \tag{3.2.38}$$

whilst the modified Lorentz equation is

$$\dddot{P} + 2\alpha\ddot{P} + \omega_r^2\dot{P} + \omega_r^2 E(t)^2[2\alpha P + \dot{P}] = \omega_p^2\dot{E}$$

Because we are dealing with non-linear effects we must use real quantities, so we write

$$E = \Re[e(t)\mathrm{e}^{\mathrm{i}\Omega t}] = \tfrac{1}{2}[e(t)\mathrm{e}^{\mathrm{i}\Omega t} + e(t)^*\mathrm{e}^{-\mathrm{i}\Omega t}] \tag{3.2.39}$$

$$P = \Re[p(t)\mathrm{e}^{\mathrm{i}\Omega t}] = \tfrac{1}{2}[p(t)\mathrm{e}^{\mathrm{i}\Omega t} + p(t)^*\mathrm{e}^{-\mathrm{i}\Omega t}] \tag{3.2.40}$$

Note that the term $E(t)^2[2\alpha P + \dot{P}]$ is real, so we write it in the form

$$E(t)^2[2\alpha P + \dot{P}] = E(t)^2 Q(t) = \tfrac{1}{2}[X\mathrm{e}^{\mathrm{i}\Omega t} + X^*\mathrm{e}^{-\mathrm{i}\Omega t}] \tag{3.2.41}$$

The physical quantity E^2Q is given by

$$E^2Q = \tfrac{1}{8}[e(t)\mathrm{e}^{\mathrm{i}\Omega t} + e(t)^*\mathrm{e}^{-\mathrm{i}\Omega t}]^2[q(t)\mathrm{e}^{\mathrm{i}\Omega t} + q(t)^*\mathrm{e}^{-\mathrm{i}\Omega t}] \tag{3.2.42}$$

where the relation between q and p is $q(t) = 2\alpha p(t) + \dot{p}(t)$.

Because of the non-linearity the spectrum of ε and $\wp$ will include harmonics of the carrier frequency Ω but their amplitudes should be small and we are not interested in them. We can therefore equate coefficients of $\mathrm{e}^{\mathrm{i}\Omega t}$ in equations (3.2.41) and (3.2.42) giving

$$X = \tfrac{1}{4}(e(t)^2 q(t)^* + 2e(t)\, e(t)^* q(t)) \tag{3.2.43}$$

Taking the inverse Fourier Transform gives

$$\mathrm{i}(\Omega+\omega)\frac{\omega_p^2}{\chi(\Omega+\omega)}\wp(\omega) + \mathfrak{F}^{-1}\left\{\tfrac{1}{4}\omega_r^2[e^2q^* + 2e\, e^*q]\right\} = \mathrm{i}(\Omega+\omega)\varepsilon(\omega) \tag{3.2.44}$$

where $\mathfrak{F}$ is the Fourier transform operator.

Now let $\wp(\omega) = \wp_0(\omega) + \wp_1(\omega)$ where

$$\wp_0(\omega) = \chi(\Omega+\omega)\varepsilon_0(\omega)$$

and the correction $\wp_1(\omega)$ satisfies

$$\wp_1(\omega) = \frac{\chi(\Omega+\omega)}{\mathrm{i}(\Omega+\omega)}\frac{\omega_r^2}{\omega_p^2}\,\mathfrak{F}^{-1}\left\{\tfrac{1}{4}[e^2q^* + 2e\, e^*q]\right\} \tag{3.2.45}$$

and

$$\varepsilon_1(\omega) = -\frac{\mathrm{i}\delta(\Omega+\omega)^2}{kc^2}\wp_1(\omega) \tag{3.2.46}$$

3.2.4 Summary

The key results of the analysis described in this chapter are the following equations;

$$q^{(n)} = \mathfrak{F}\left\{(2\alpha + \mathrm{i}(\Omega+\omega))(\wp_0 + \wp_1^{(n)})\right\} \tag{3.2.47}$$

$$\varepsilon_1^{(n)} = -\frac{\mathrm{i}\delta(\Omega+\omega)^2}{kc^2}\wp_1^{(n)} \tag{3.2.48}$$

$$\varepsilon^{(n)} = \varepsilon_0^{(n)} + \varepsilon_1^{(n)} \tag{3.2.49}$$

$$e(t) = \mathfrak{F}\varepsilon^{(n)} \tag{3.2.50}$$

$$\wp^{(n+1)} = \frac{\chi(\Omega+\omega)}{\mathrm{i}(\Omega+\omega)}\frac{\omega_r^2}{\omega_p^2}\,\mathfrak{F}^{-1}\left\{\tfrac{1}{4}[e^2 q^{(n)*} + 2e\,e^* q^{(n)}]\right\} \tag{3.2.51}$$

These equations can be solved numerically by the iteration displayed in 3.2.51. We set the initial pulse with a Gaussian shape in the time domain. We then Fourier transform it onto the frequency domain where all the pulse propagation is coded. A TRANSMIT function is created which takes the pulse field and calculates the corresponding polarisation. Then we use equation 3.2.47 to find the operator $q^{(n)}$, defined in 3.2.42, and the polarization array $\wp^{(n+1)}$ from equation 3.2.51. We then find the array $\varepsilon_1^{(n)}$ which represents the nonlinear part of the electric field inside the layer using equation 3.2.48. The coefficients from 3.2.26 and 3.2.27 are used to calculate the transmitted electric field arrays.

Chapter 4

Numerical and Experimental Results of the Model

4.1 Introduction

In this chapter, we use the model discussed to show the effect on a pulse of repeated transit of a thin weakly absorbing slab of a medium where the field intensity is strong enough. In order to do this, we need realistic values for the model parameters: ω_p, E_{stark} and the gain bandwidth. I shall present experimental results I achieved in trying to find these parameters that would help produce a picture of how sub-picosecond pulses are formed in a mode-locked VECSEL cavity. Some of the results achieved by other members is briefly described and also referenced.

4.2 Experimental Characterisation of Pulse Formation Mechanism

4.2.1 Gain Bandwidth Determination for a CW VECSEL

The effective gain bandwidth of a VECSEL can be determined experimentally using the spectro-temporal techniques described in this section. The experiments are based on intra-cavity laser absorption spectroscopy (ICLAS) techniques developed by Baev et al in [51]. They used rate equations to describe the temporal dynamics of the laser. Although their technique was applied to a four-level laser system, it can also be applied

to a semiconductor laser, which is a two level system, with adjusted probability rates for stimulated and spontaneous emissions [52].

From the analysis done by Baev et al in [51] we will use Equation 4.2.1. This equation forms the basis of the spectrotemporal experiment, as it allows for measuring the gain bandwidth by measuring the spectral bandwidth, $\Delta\nu_{BW}$, of the laser output at various times after steady state. Eventually, the laser output will settle to a final steady state linewidth. This occurs when spectral condensation is compensated for by the broadening effects due to spontaneous emission.

$$\Delta\nu_{BW} = \frac{c}{2L}\sqrt{\frac{ln2}{\gamma t'}} \cdot Q \tag{4.2.1}$$

Spectral condensation then is initiated as the gain compensates the loss of the cavity at the central mode and a 'condensation' of the optical spectrum is observed. The number of photons increases exponentially before settling to a steady state. The time it takes the photons number to saturate is given by τ_{ss}. The narrowing of the spectrum can be related to the generation time by Eq 4.2.1. The generation time, t', is the time from when the photon number becomes stationary i.e. $t' = t - \tau_{ss}$.

where γ is the broadband cavity loss which is given by $\gamma = -c\ln[R_{OC}(1-l_i)^2]/2L$ where R_{OC} is the output coupler reflectivity, l_i is the internal loss and L is the cavity length. The spectral width of the gain is Q at half width half maximum (HWHM). The generation time, t', is the time from when the photon number becomes stationary i.e. $t' = t - \tau_{ss}$.

Hoogland and Garnache made the first attempt to measure the bandwidth available from the InGaAs-based gain [53, 28]. They used a VECSEL operating in continuous wave mode in a W-cavity with a repetition rate of 328 MHz [41]. The gain structure contained 7 8-nm strain-balanced $In_{0.23}Ga_{0.77}As$/GaAsP quantum wells grown over a 27.5 pair AlAs/GaAs Bragg mirror centered at the 1030 nm design wavelength. The wells are distributed between GaAs spacer layers in a 2-1-1-1-0-1 pattern at successive antinodes of a 7xλ/2-thick pump-absorbing layer. An AlAs window layer was grown on top so that the optical thickness of the microcavity is 15xλ/41.03 (i.e. close to anti-resonant). The gain structure was pumped by a 1 W 830 nm diode and used as a folding mirror in a W-cavity with 328 MHz longitudinal mode spacing.

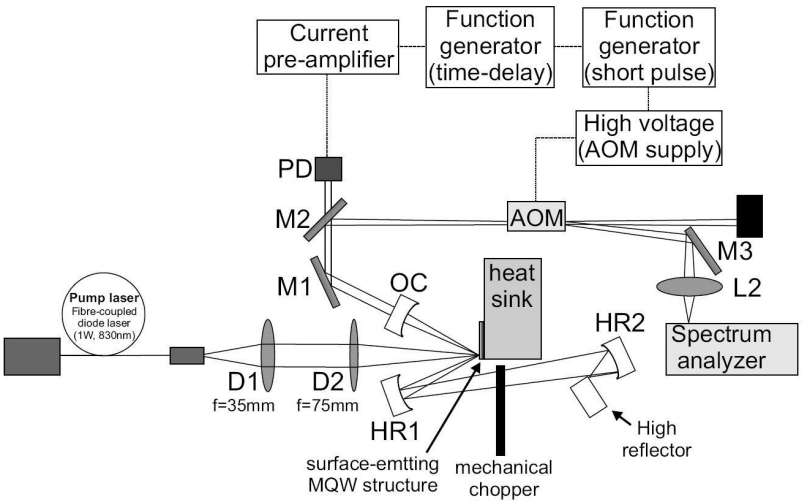

FIGURE 4.1: Schematic diagram of the setup used to determine the effective gain bandwidth in the VECSEL cavity. D1,D2 and L2 are lenses, OC is an output coupler, HR1 and HR2 are high reflectors, M1-3 are mirrors and PD is a photodiode.

Fig 4.1 shows the experimental setup Hoogland used. A mechanical chopper is used to modulate the Q-factor of the cavity. The output of the VECSEL is then sent to an optical multichannel analyser after going through an acousto-optic modulator (AOM). The chopper also acts as a trigger for the deflection by the AOM of the beam path towards the spectrum analyser. This deflection only occurs after a certain delay controlled by a function generator. A number of spectra were recorded and their widths plotted against the corresponding generation time as shown in Fig 4.2. The slope of the data is used to calculate the effective gain bandwidth in the VECSEL cavity. From 4.2.1, we can rewrite the gain bandwidth in terms of wavelength as

$$\Omega_g = \frac{\lambda^2}{c}\sqrt{\frac{\gamma}{ln(2)\cdot slope}}. \tag{4.2.2}$$

We estimate the broadband losses, γ, to be around $3.6 \times 10^7\ s^{-1}$ whilst the slope from Fig 4.2 is 2.4×10^{19} s. This yields a gain bandwidth of 30 ∓ 3 nm. This bandwidth, if completely mode locked, can give pulses shorter than 100 fs.

4.2.2 Spectrotemporal Measurements of a Mode Locked VECSEL

The spectrotemporal experiment was technically more difficult in the mode-locked case since the cavity used was shorter than in the CW case and the cavity loss was higher since a SESAM was used which meant everything was much faster. But it was interesting

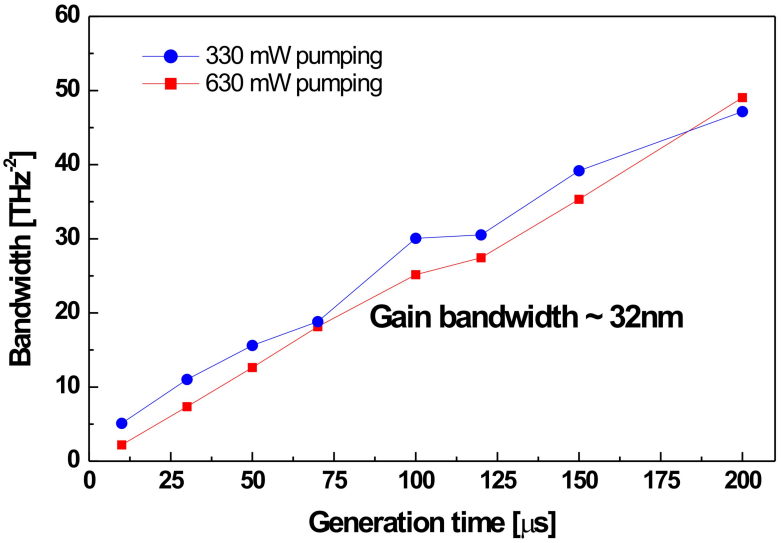

FIGURE 4.2: Inverse of bandwidth squared plotted against generation time for two pumping powers. Circular dots are for 330 mW pumping and square dots are for 630 mW input power. A linear fit of the data yields a slope of $2.4 \times 10^1 9$ s.

to see the effective gain bandwidth of laser including the filtering by the slow response time of carrier recombination in the saturable absorber.

A SESAM with a single absorbing InGaAs quantum well grown over a 27.5-pair GaAs/AlAs DBR was used to mode-lock the 1.17 GHz VECSEL. The well is positioned within 2 nm of the air surface and is designed for fast absorption recovery by surface recombination [28]. The cavity used had the Z-configuration where the SESAM is placed on one end. This cavity was better suited to mode-locked operation, ensuring that the intervals between arrival of pulses on the gain structure were shorter than the carrier lifetime, and that the pulses did not saturate either gain or SESAM too strongly. The aim of it was to see how fast the steady state between all the effects that influence pulse formation is reached. Spectral condensation occurs faster in the shorter cavity but the process has similar characteristics as for the longer cavity.

This laser could be operated at a wavelength of 1042 nm where it gives pulses of 480 fs and at 1033 nm with 2.5 ps pulses. Spectrotemporal measurements on the two regimes were performed and will be discussed here. Keith Wilcox did the measurements on the sub-500 fs pulses and he reported his work in his thesis [54]. The gain bandwidth he reported from this experiment was 35 nm.

I did the experiment on the mode-locked VECSEL operating the regime with the longer pulses at 1033 nm. Mode-locking, in this case, is due by band-filling of the resonant interband transition in the quantum well. The optical gain bandwidth available was found not to be affected by the presence of the SESAM in the cavity and the optical spectrum bandwidth was found to be roughly independent of the degree of saturation of the absorber and the gain. Fig 4.3-A shows the resulting spectral condensation process taken after different generation times while Fig 4.3-B shows the inverse bandwidth squared plotted against generation times. The slope of the data in Fig 4.3-B is around $2 \times 10^{-20}\ rad^{-2}s$ which gave a gain bandwidth of 35 nm.

As the results have shown, we have not seen any evidence to suggest that the effective bandwidth is reduced in the presence of a SESAM. Even when we drive the SESAM at resonance at 1030 nm, where absorption is bleached and only recovers once carriers have recombined on a timescale close to 30 ps, no evidence of filtering of the gain bandwidth can be found.

4.2.3 Mode-Locking Onset Time

The technique used to determine the mode-locking onset time involved and was done by Wilcox in his thesis [54]. In the experiment, Wilcox probed the two contrasting regimes of operation for the mode-locked VECSEL using a technique called mode-locking onset experiment. This involved measuring the change in intensity with time of both the fundamental laser light and its frequency doubled second harmonic. Here, I report an interpretation of his data that has not been reported in his thesis and show that the 480 fs pulses are consistent with a pulses from a fast saturable absorber [44]. We can estimate the value of E/E_{stark} from this data where E_{stark} can be found from the value of the saturation intensity I_{stark} through $E_{\text{stark}} = \sqrt{I_{stark}}$.

The laser used in the mode-locking onset experiment used QT1544 and QT1627 respectively as gain and SESAM structures, with an output power of 20 mW, output coupler transmission of 0.7%, and mode waist spot sizes of 60 μm and 11 μm on gain and SESAM respectively. For this 1-GHz repetition frequency laser $T_R = 1$ ns, and the steady-state pulse duration was 500 fs. A Lithium Niobate crystal was used as the nonlinear crystal and an Si photodiode was used to detect its output. Figure 4.4 shows the resulting data. The black curve shows the fundamental laser signal. At time -12 μs, the laser field starts to grow from amplified spontaneous emission (ASE) noise and it grows slowly over 28 μs reaching a steady state value at 16 μs. The green curve represents

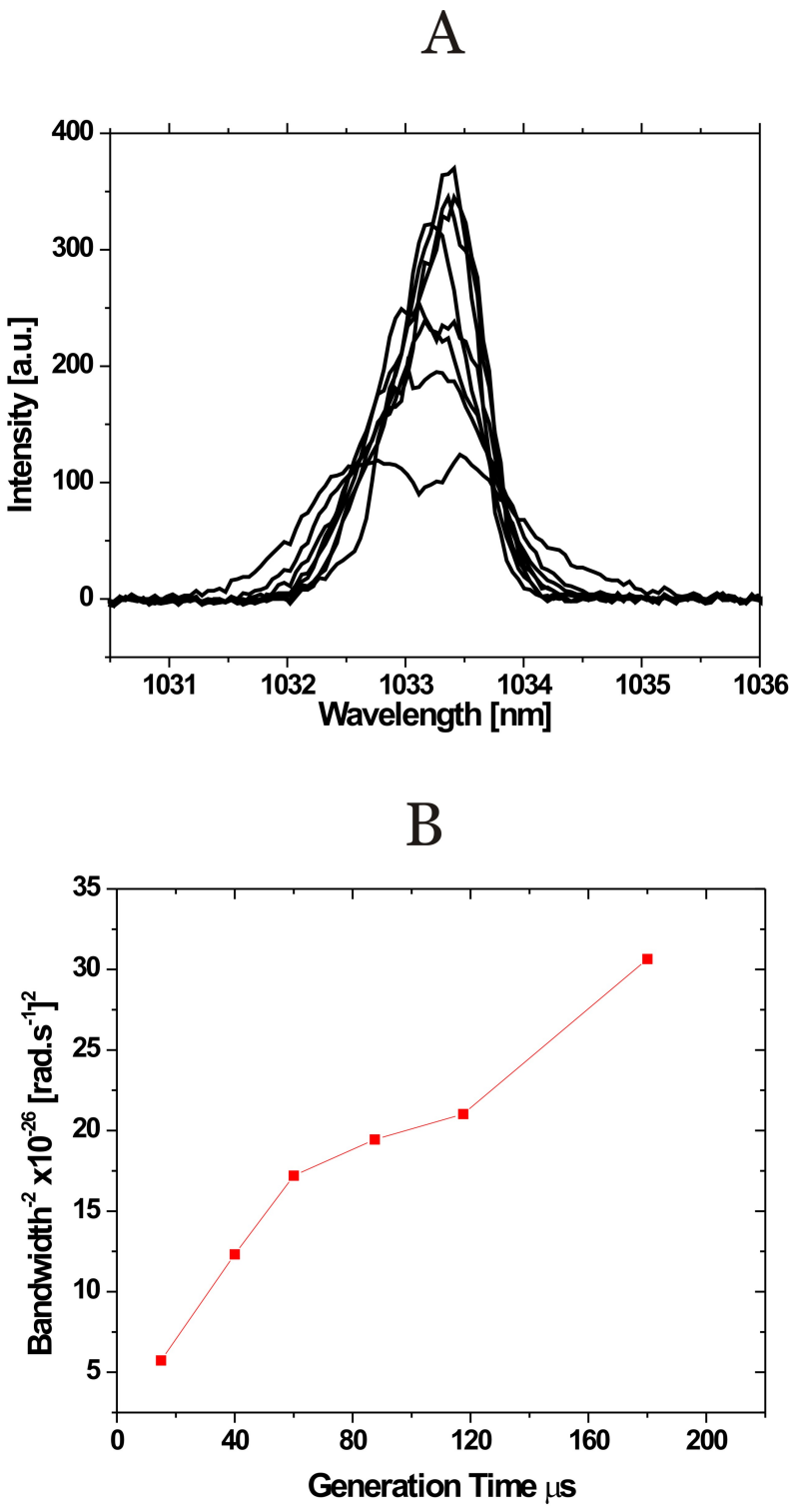

FIGURE 4.3: A- Spectral condensation of modelocked pulses spectrum with generation times starting from 15 μs for the broadest bandwidth to 40, 60, 87, 117, 180, 340 and 700 μs. B- Inverse of bandwidth squared plotted against generation time. The rate of spectral condensation is slower compared to the CW experiment due to the presence of a SESAM, but it yields the same effective gain bandwidth of 35 nm.

the second harmonic signal detected. The curve does not start to grow until around -5 μs indicating that pulses have started to form inside the cavity and have large enough peak power to generate second harmonic frequencies. The mode-locking onset time can be thought of as the time difference between the beginning of the two processes and is indicated by the two vertical dashed lines. Pulses of 481-fs and 2500-fs duration were used in this particular experiment. The 2.5 ps pulse regime is attributed to comventional bleaching of the SESAM absorption whilst the sub-500 fs pulse regime is the one due to the fast saturable absorption. The first conclusion is that we have two very different mode-locking regimes in one of which has a much longer onset time and a much slower mode-locking buildup time.

In order to extract a value for two important parameters for our model, further analysis of the data shown in Fig 4.4 was done. The values of the Stark field E_{stark} and pulse change per roundtrip $\delta\tau/\tau$ can be experimentally found using the following analysis. We assume that the fast time profile of the pulse is represented by

$$I(t,T) = I_0 sech^2\left(\frac{t}{\tau}\right), \tag{4.2.3}$$

where intensity I_0 and the pulse length, τ, are functions of the slow time T, and the pulse fluence is given by

$$U(T) = \int I(t,T)dt = 2I_0\tau. \tag{4.2.4}$$

Consider a SESAM that acts as a fast saturable absorber with saturation intensity I_{stark} and modulation depth ΔR. We can write the pulse intensity as

$$I(t,T+T_R) = I(t,T)\left(1-\Delta R\left(1-\frac{I(t,T)}{I_{Stark}}\right)\right), \tag{4.2.5}$$

whence

$$I(t,T+T_R) = I_0(1-\Delta R)^2\left(\frac{t}{\tau}\right) + \frac{I_0^2\Delta R}{I_{Stark}}^4\left(\frac{t}{\tau}\right). \tag{4.2.6}$$

To first order in small quantities, the change in the duration of the pulse caused by one pass of the absorber is given in [44] as

$$\frac{\Delta\tau}{\tau} = -\frac{I_0}{I_{Stark}}\Delta R = -\frac{U\Delta R}{2I_{Stark}\tau} \tag{4.2.7}$$

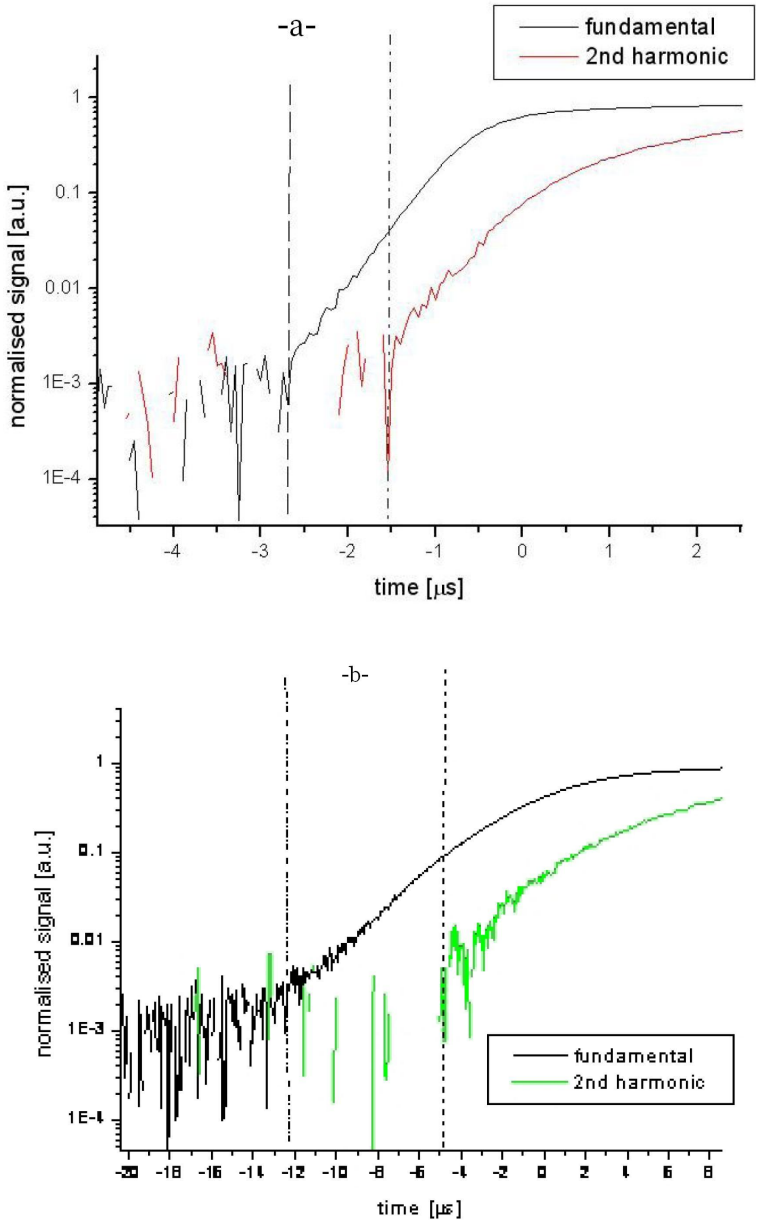

FIGURE 4.4: Mode-locking onset with the fundamental and second harmonic signals shown. The pulses with which the experiment was performed were: a) 2.5 ps at 1033 nm and b) 481 fs long at 1042 nm. The vertical lines indicate the starting points of the mode-locking process for the two cases.

where $U = 2I_0\tau$ is the pulse energy. The fast saturable absorber also changes the pulse energy. By integrating equation 4.2.5, we get:

$$U(T+T_R) = U(T)(1-\Delta R) + \frac{4}{3}\frac{I_0^2 \Delta R \tau}{I_{Stark}} = U(T)(1-\Delta R) + \frac{U^2 \Delta R}{3 I_{Stark}\tau}, \tag{4.2.8}$$

We assume that the gain imposes a time-independent filter on the amplitude of the pulse in the frequency domain with transmission. The rate of pulse shortening taken from Svelto's Principles of Lasers [55, p. 571-575] is given by

$$\frac{\Delta\tau}{\tau} = +\frac{2g_0}{\Omega^2\tau^2} \tag{4.2.9}$$

where g_0 is the intrinsic single pass gain. In terms of pulse energies,

$$U(T+T_R) = U(T)\left(1 + g_0 - \frac{1}{3}\frac{2g_0}{\Omega^2\tau^2}\right) \tag{4.2.10}$$

$$\Delta U = T_R\frac{dU}{dT} = \left(g_0\left(1 - \frac{2}{3\Omega^2\tau^2}\right) - \Delta R\right)U + \frac{\Delta R}{3 I_{Stark}\tau}U^2$$

$$\Delta\tau = T_R\frac{d\tau}{dT} = -\frac{\Delta R}{I_{Stark}}U + \frac{2g_0}{\Omega^2\tau}$$

We can combine these equations into a form that can be integrated:

$$T_R\frac{dU}{dT} = (g_0 - \Delta R)U + \frac{U}{3\tau}\left[-T_R\frac{d\tau}{dT}\right]$$

whence

$$\frac{3}{U}\frac{dU}{dT} + \frac{1}{\tau}\frac{d\tau}{dT} = -\frac{3\gamma}{T_R},$$

where $\gamma = g_0 - \Delta R$. Hence

$$U^3\tau = A\exp\left(-\frac{3\gamma T}{T_R}\right),$$

showing that the pulse energy settles to the steady state more rapidly than the pulse duration. In the steady state we have $U = U_0$ and $\tau = \tau_0$, where

$$\tau_0 = \frac{2(g_0/\Omega^2)I_{Stark}}{U_0\Delta R}.$$

Consider the evolution of the pulse when the laser is sufficiently close to the steady state that we may assume $U \approx U_0$. Then

$$\frac{d\tau}{dT} = -S\left(1 - \frac{\tau_0}{\tau}\right),$$

where

$$S = \frac{U_0 \Delta R}{I_{Stark}}.$$

If we introduce the variable

$$\epsilon = \frac{\tau - \tau_0}{\tau_0}$$

we find that

$$T_R \tau_0 \frac{d\epsilon}{dT} = -S\frac{\epsilon}{1+\epsilon}.$$

To 1st order in ϵ we can neglect the ϵ term in the denominator, allowing us to integrate the equation for τ:

$$\tau(T) = \tau_0\left(1 + \epsilon_0 \exp\left(-\frac{S}{\tau_0}\frac{T}{T_R}\right)\right).$$

Fig. 4.5 shows rise time data from 4.4 (black V_1 and red V_2 plus a plot of V_1^2/V_2. In these rise time experiments the fundamental signal V_1 is proportional to U, and the second harmonic signal, V_2 is proportional to U^2/τ. In the figure the fundamental and second harmonic signals are normalised to steady-state values of 1. In Fig. 4.5 the fundamental signal, V_1, and the second harmonic signal, V_2, are plotted as a function of the slow time, T. Also plotted on this graph is V_1^2/V_2, which is equal to τ/τ_0, provided that we have a single pulse in the cavity which gets shorter while keeping the same functional form of its profile. This curve fits closely to a single exponential decay for times after about 10 μs.

The fitting curve of V_1^2/V_2 satisfies a single exponential with time constant of about 7.8 μs. We infer that for this laser

$$\frac{\tau_0 T_R}{S} = 7.8\ \mu\text{s},$$

corresponding to $S = 0.0064$ fs. In other words, it takes 15 to 16 round trips to take away 1 fs off the pulse. In the steady state, the gain dispersion stretches the pulse by exactly this amount each round trip. The value of S reveals the ratio I_0/I_{Stark} in this laser:

$$S = \frac{U_0 \Delta R}{I_{Stark}} = 2\tau \Delta R \frac{I_0}{I_{Stark}}.$$

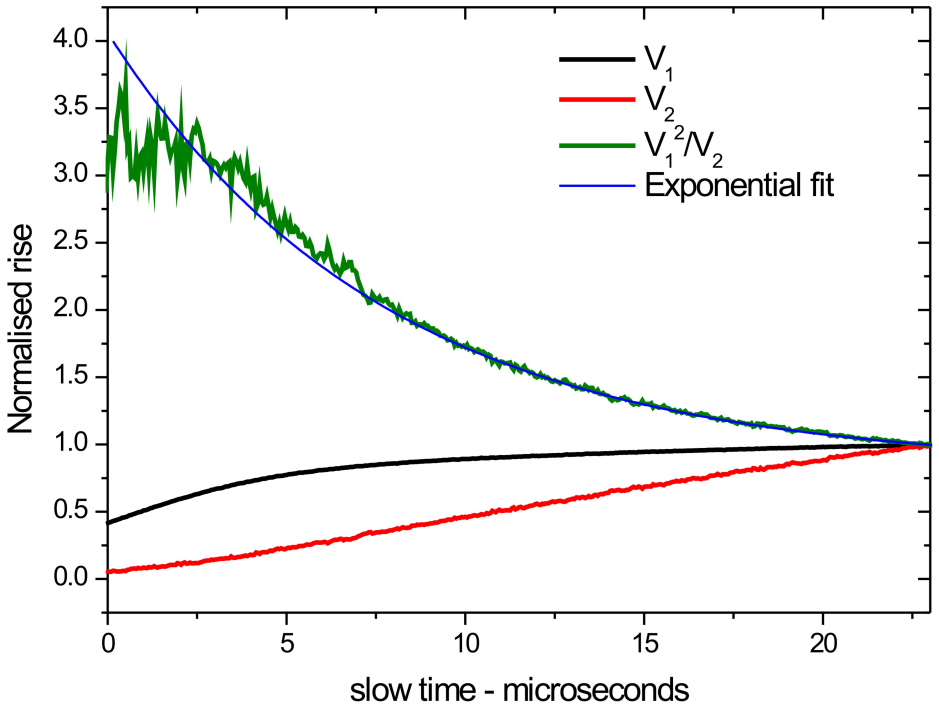

FIGURE 4.5: Plot of V_1 (black), V_2 (red), V_1^2/V_2 (green) and exponential fit with 7.76 μs lifetime (blue) as a function of slow time T.

The steady-state intracavity pulse energy in this laser is 2.9 nJ, corresponding to a pulse fluence on the SESAM $U_0 = 750$ μJ cm^{-2}. Hence

$$\frac{\Delta R}{I_{Stark}} = \frac{S}{U_0} = 8.5 \times 10^{-6} \text{ fs}(\mu\text{J cm}^{-2})^{-1}.$$

The experimental parameter that we know least well is the modulation depth, ΔR; An absorption of the order of 1% and a longitudinal confinenmemnt factor of around 0.1 gives a modulation depth of the order of 10^{-3}. Then

$$I_{Stark} = \frac{U_0 \Delta R}{S} \approx 10^{11} \text{ W cm}^{-2}.$$

In our laser

$$I_0 = \frac{U_0}{2\tau_0} = 750 \ \mu\text{W cm}^{-2},$$

suggesting that it operates with $I_0/I_{Stark} \approx 0.008$, or $E_0/E_{Stark} \approx 0.09$.

4.2.4 Summary

- The effective bandwidth available from our gain sample is around 32 nm indicating, theoretically, that it is possible to achieve sub-100 fs pulses from this particular gain sample.
- The onset time for mode-locking occurs around 1 μs for a picosecond VECSEL whilst it is about 7 μs for sub-500 fs VECSEL. These numbers correspond to a few thousand round-trips in a 1 GHz laser cavity.
- $E_0/E_{Stark} \approx 0.09$
- The rate of pulse shortening due to gain filtering and the fast saturable absorption under these conditions is approximately 0.0064 fs per round trip.

4.3 Numerical Results

The investigation of the mechanism of mode-locking was done by implementing the theory provided in Chapter 3 using a computer program. Python software was picked as it was favored due to the existence of ready-made fast Fourier transform libraries that are useful in this project. A list of parameters was investigated from all the experiments and evidence seen so far while working with the sub-500 fs VECSELs.

4.3.1 Parameters Used in the Numerical Solutions

The model simply takes a Gaussian pulse of a certain length and propagates it through a 'Stark layer'. This represents the InGaAs quantum well inside the SESAM. The Lorentz differential equation 3.2.7 that describes the semi-classical relationship between an ensemble polarisation P and an incident E-field is solved using the iterations described in 3.2.4.

The plasma frequency ω_p is one of the important parameters that needs to be included in solving the equation. It represents the number density of available carriers in the saturable absorber. The method we used to determine its value was to investigate the profile of the imaginary part of the refractive index of the medium. We know from experimental observation that we get, roughly, a 1% absorption per pass through the SESAM. By changing the plasma frequency, we can vary the absorption in the medium.

We can write the refractive, n, index in terms of the real part, n', and the imaginary part, n'', as follows;

$$n = n' + in''$$

The electric field inside a medium can be expressed as;

$$E(z,t) = E_0 e^{i(\omega t + kz)}$$

Using the relationship between the wavenumber, k, the carrier frequency, ω, the propagation distance, z and the refractive index given by

$$\omega = \frac{ck}{n}$$

We can write the E-field as

$$E(z,t) = E_0(t) e^{i\omega n' z/c} e^{-\omega n'' z/c}$$

where $E_0(t) = E_0 e^{i\omega t}$ is the time dependent part of the electric field. We know the optical intensity, I, is proportional to

$$I \propto E^* E \propto e^{-2n''\omega z/c} \approx 1 - \frac{-2n''\omega z}{c}$$

The expression has the form of a Beer and Lambert law for absorption. So, we can get a pretty good estimate of the plasma frequency if we can match the absorption we see experimentally. This was done using a numerical program that plots the real and imaginary parts of the refractive index as shown in Fig 4.6. The medium response to a very weak electric field (the real and imaginary parts are in blue) and a strong electric field (the real and imaginary parts are in red) are shown. The resonance wavelength of the absorber(around 1030 nm) and the carrier wavelength (1042 nm) are also indicated. The absorption of the layer is indicated by the change in the value of the imaginary part. The value of the plasma frequency was set to $\omega_p = 1.4 \times 10^{14}$ Hz as an input in the code that was used to plot this figure and was then changed in order to get a 1% absorption per pass through the quantum well.

The dipole matrix element, μ, also appears in equation 3.2.7 where it is part of E_{stark}. To find its value, an atomic physics discussion is done starting from electron-light field **A** interaction described by the Hamiltonian

$$H = \frac{e}{2m} (\mathbf{p} \cdot \mathbf{A} + \mathbf{A} \cdot \mathbf{p}) \tag{4.3.1}$$

In a 2-level atom model, we use the electric dipole approximation from [56, p. 42-44]:

$$\left\langle \phi_1 \left| \frac{e}{m} p_x \right| \phi_2 \right\rangle = i\omega_0 \left\langle \phi_1 \left| ex \right| \phi_1 \right\rangle = i\omega_0 \mu \tag{4.3.2}$$

From [40], we have

$$\left| \left\langle \phi_1 \left| \frac{e}{m} p_x \right| \phi_2 \right\rangle \right|^2 = \left(\frac{e}{m} \right)^2 |M|^2 \times |\langle v| \, c\rangle|^2 \tag{4.3.3}$$

where $|M|^2$ is a constant characteristic of a specific III-V material, and $\langle v|c\rangle$ is an overlap integral for the bound valence and conduction band states, which can be approximated to unity. For an $In_xGa_{1-x}As$ system, the value of

$$\frac{2\,|M|^2}{m_0} = 28.8 - 6.6x \text{ [eV]} \tag{4.3.4}$$

can be quoted from [40]. Hence $|M|^2 = 27.3$ eV. The value of the μ can then be extracted from the following;

$$|\mu| = \frac{e}{\omega_0} \sqrt{\frac{|M|^2 \, e}{2m_0}} = 1.3 \times 10^{-28} \text{ Cm}$$

Another parameter in this model is the threshold value of the electric field above which nonlinear effects start to play a role in the pulse propagation dynamics. The value is given the parameter name of E_{stark} in equation 3.2.6 where $E_{\text{stark}} = \hbar\omega_0/2\mu$. At a wavelength of 1 μm we have $\hbar\omega_0 = 2 \times 10^{-19}$ J and hence $E_{\text{stark}} = 0.8 \times 10^9$ Vm^{-1}. For SESAMs we use in our labs, the quantum well is positioned close enough to the surface that the E-field is about the same on the well as it is in the air outside. This Stark field therefore corresponds to a peak intensity in the air of

$$I = \frac{1}{2} \epsilon_0 c \, |E_{\text{stark}}|^2 = 8.5 \times 10^{14} [W m^{-2}]$$

This compares favourably with the value obtained from Section 4.2.1.2. For a circular spot of radius 10 μm on the SESAM, and a pulse of duration 500 fs, this would imply an intracavity pulse energy of 130 nJ. With 1% output coupling and 1 GHz repition rate, we would have a laser operating at 1.3 W. In practice, our lasers operated at average

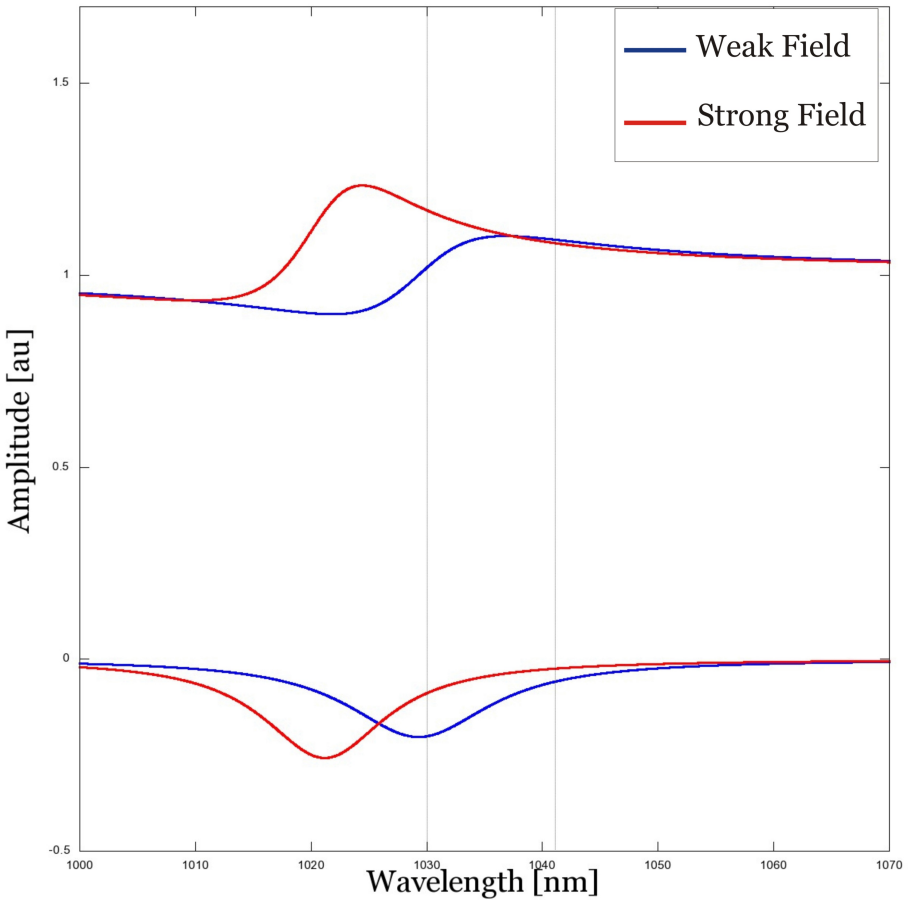

FIGURE 4.6: The instantaneous response of the refractive index of a quantum well embedded in a SESAM to a CW electric field. The real parts of the refractive index are the top two graphs and bottom two are the imaginary parts. The response to a weak field is in blue whilst the response to a strong field is in red. The vertical dotted lines indicate the resonance wavelength of the quantum well and the output wavelength of the laser.

powers ranging from 0.5-8% of this. Hence, the E-field on the well is very roughly 7 to 25% of the E_{stark} value.

Parameters	Value
μ: The Dipole Element	1.3×10^{-28} Cm
ω_p: The Plasma Frequency	1.4×10^{14} Hz
ω_r: The Resonance Frequency	2.94×10^{15} Hz
ω_0: The Carrier Frequency	2.88×10^{15} Hz
T_2: Dephasing Time	40 fs

TABLE 4.1: Numerical Model Parameters

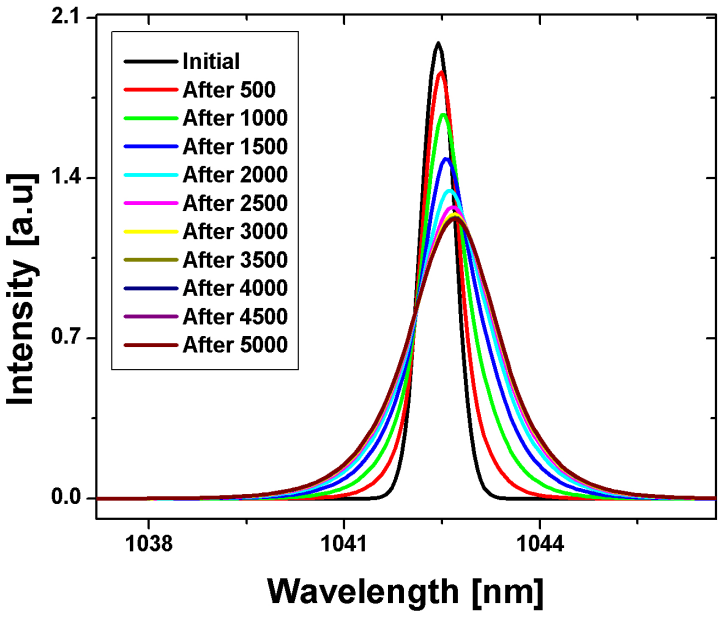

FIGURE 4.7: Numerical propagation of an 800 fs pulse to 250 fs pulse in the wavelength domain as a result of Stark effect shortening.

4.3.2 Model Results

Fig 4.7 shows the spectra of the pulses on a wavelength scale and Fig 4.8 shows the temporal intensity profiles of those pulses. The weak initial pulse is initially Gaussian, transform-limited, 800-fs-long and centred at 1042 nm, being shaped by repeated transits of an absorber centered at 1030 nm with T_2 = 40 fs. The evolution of the temporal pulse and spectrum is shown for 5000 round trips of the model. The pulse evolves from a 800-fs-pulse to a sech-squared-profile 260-fs-pulse, with a steady state being reached after 3000 round trips. The Stark nonlinearity broadens the pulse spectrum. This latter is also slightly asymmetric possibly because the linear absorption is attenuating one side a little bit more.

Figure 4.9 shows the variation of the pulse duration plotted with time along with an exponential fit of the data. It can be seen that initially the pulse shortens rapidly, but as the number of round trips increases the shortening effect reduces as the balance point of the competing fast saturable absorption and the parabolic gain filter function is approached. The gain bandwidth of this laser was measured to be 40 nm FWHM, implying that gain dispersion will lengthen the pulses by around 10^{-3} per round trip. This model allows us to numerically find the strength of the Stark effect that is present in our laser to balance this to be $0.1 \times E_{stark}$.

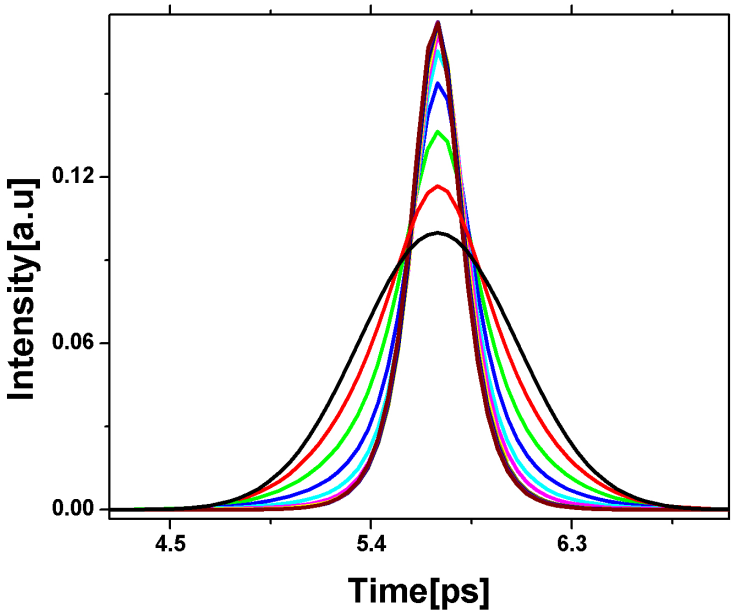

FIGURE 4.8: Numerical propagation of an 800 fs pulse to 250 fs pulse in the time domain as a result of Stark effect shortening. The colors of the graphs correspond to the same annotations on the previous figure.

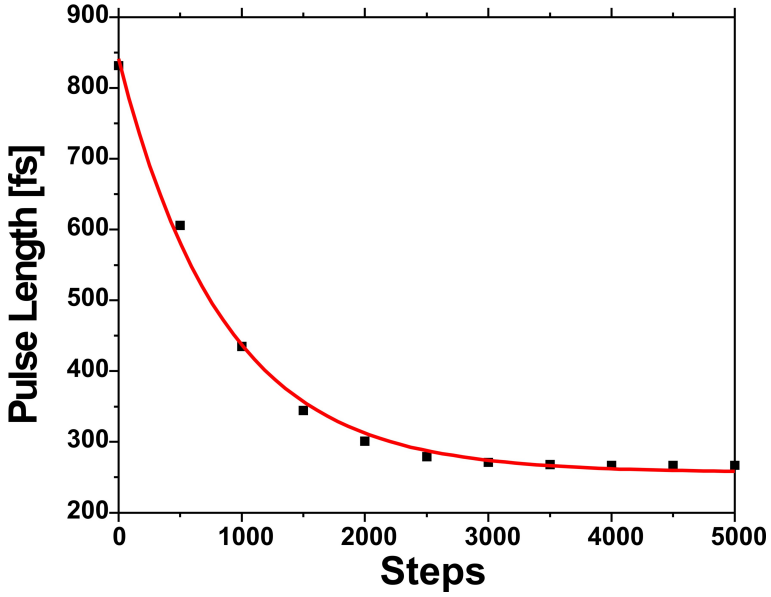

FIGURE 4.9: Pulse length vs. round-trip number. An exponential fit of the data points is shown in red.

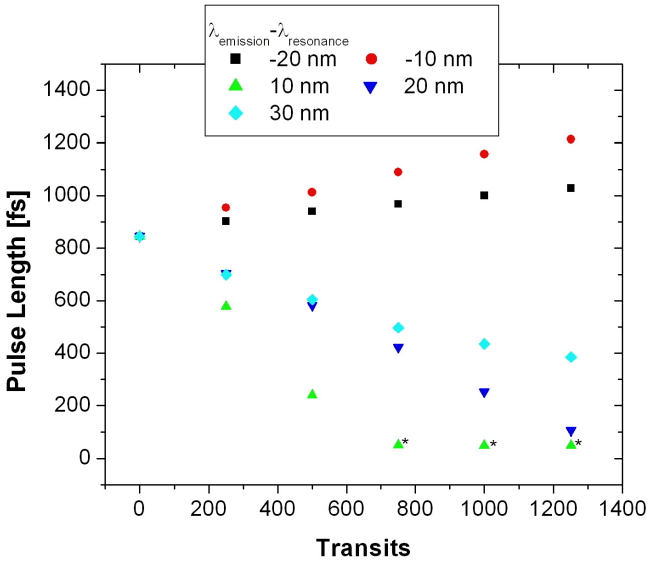

FIGURE 4.10: Pulse length vs. round-trip number for various detuning of the laser emission wavelength from resonance. The absorption profile had a halfwidth half maximum of about 15 nm. The star signs on the last data points for 10 nm detuning indicate a numerical artefact from the program.

One other parameter that we can tweak on the program is how far the laser emission is detuned from the resonance of the quantum well. The model was tested for a number of detunings by keeping the resonance frequency value the same and varying the carrier frequency. For each detuning value, an initial pulse with a length of 800 fs was propagated through the absorber for 1250 transits. The length of the pulse was recorded after each 250 transits and is plotted on Fig 4.10.

For negative detunings, i.e. when the laser is operating to the blue side of the resonance, the pulses always get longer. The closer the emission is to the resonance the faster the rate of pulse lengthening. For positive detunings, however, the propagating pulse always gets shorter and this effect is stronger when the laser is operating closer to the absorber resonance.

With this model we were able to probe the limits of short pulse formation by testing the code for much shorter initial pulses than the 800 fs shown in Fig 4.8 . Broadly speaking it is to do with how strong a value of E/E_{stark} can be in shaping pulses. Fig 4.11 shows pulse propagation in the time domain for four different initial pulses. It is possible to see that when the initial pulse is above 70 fs, pulse shortening occurs. However, when the initial pulse is below 70 fs, pulses are broadened.

The only parameter on this scale in the model is the decoherence time T_2, the relaxation time of the dipole moment. We only see effects like absorption and the Stark effect on

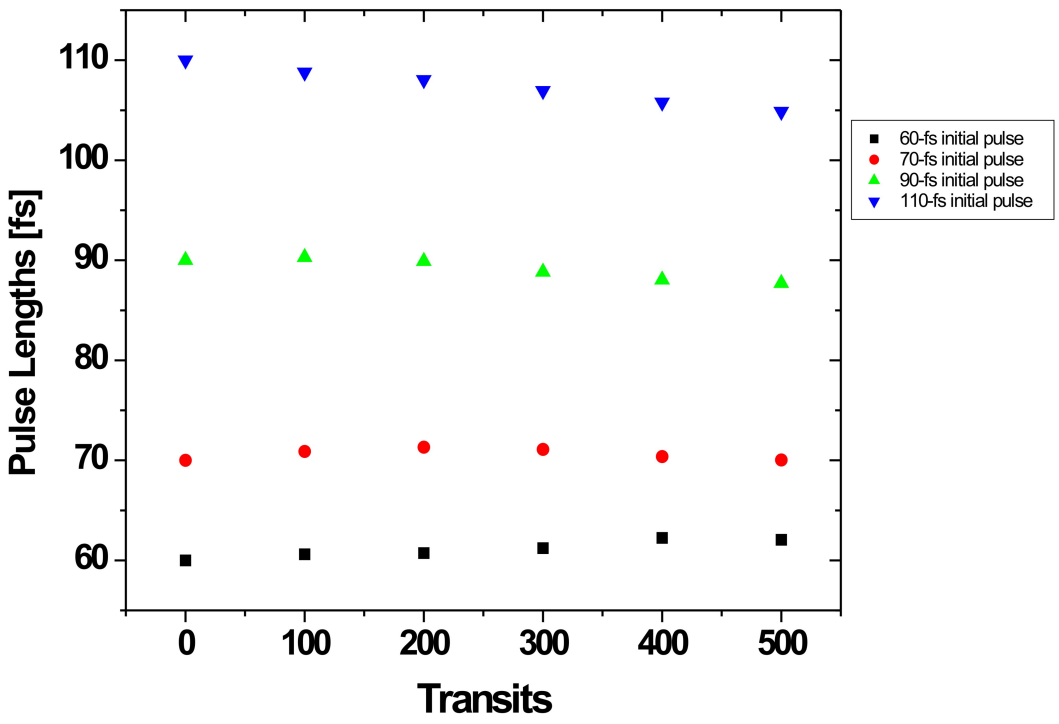

FIGURE 4.11: Pulse propagation after various round trips with different initial pulses of 60, 70, 90 and 110 fs

timescales longer than the coherence time while below it we observe coherence effects. For these very short pulses it is clear that coherent effects starting to play a role but with this model we have artificially suppressed them by putting the population $n = -1$ in section 3.2.2 and in future work this will be changed to accommodate population changes in the two-level atom.

Very recent results work at our group have demonstrated transform-limited 70 fs pulses in a VECSEL as shown on the autocorrelator output in Fig 4.12 from Quarterman et al [57] (awaiting publication). The repetition rate of the laser is 1 GHz; the central wavelength is 1032 nm; the bandwidth is more than 20 nm FWHM, and the average power is 20 mW. The pulses of this laser are shaped by self-absorption modulation caused by the optical Stark effect. Instead of producing a single pulse each round trip, the laser produces a group of ultrashort pulses regularly spaced at 1 ps or less; the total length of the train is several picoseconds. Only one of the pulses shown on the figure on the right is an autocorrelation whereas the rest are cross-correlations. The asymmetry of the pulse in the output is due to the slow response time of the autocorrelator detector.

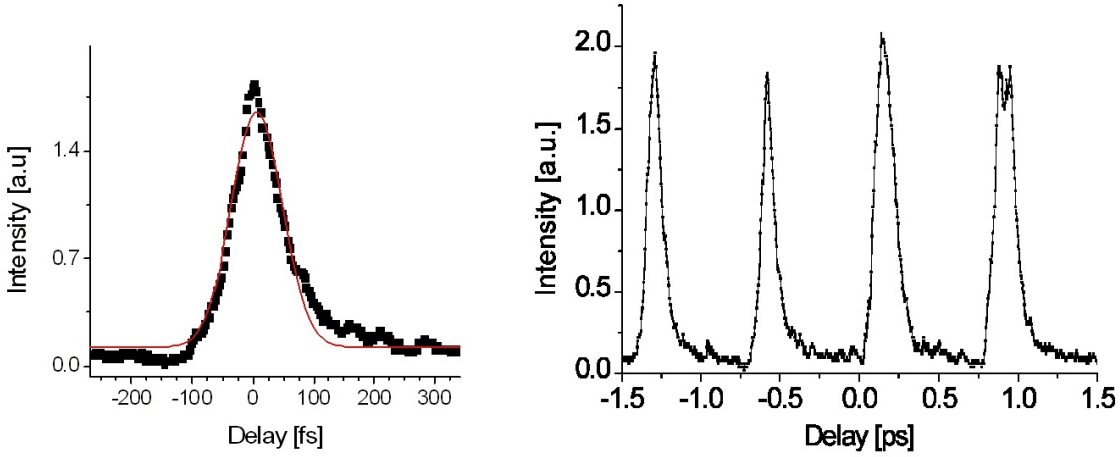

FIGURE 4.12: Autocorrelation of the laser pulse with a gaussian fit with FWHM of 65 fs on the left side. The right side figure is an autocorrelation of the train of 70 fs pulses separated by 750 fs.

We used a high modulation-depth SESAM, identical to the one used in [30], which was grown by standard molecular beam epitaxy with high crystalline quality, and has low non-saturable loss of less than 0.3%. It incorporates a standard DBR below a GaAs spacer layer containing a single 8-nm $In_{0.25}Ga_{0.75}As$ quantum well (QW) positioned 2 nm below the air interface to benefit from fast surface state carrier recombination. The difference relative to our earlier structures, which gave 480 fs pulses, lies in the thinness of the spacer layer; which at 13.5 nm sets the QW a distance $0.3\lambda/4$ from the anti-node at the DBR interface. The designed value of modulation depth is 0.7%, double that of earlier designs with the 40-nm spacer layers.

4.3.3 Conclusion

Our semi-classical two-level atom absorber in intense field exhibits a weak pulse shaping mechanism that is of comparable magnitude to that observed experimentally in VECSELs operating in the femtosecond regime. In the analytical model, the nonlinear terms are proportional to $|E|^2 / |E_{\text{stark}}|^2$, so that nonlinearity may be described as an optical Stark effect giving rise to power broadening and blue shifting of the resonance. This correspondence strongly suggest that a non-linear effect of this type contributes to the mode-locking effect we observe.

The bandwidth of the effect is comparable to the bandwidth of the absorbing resonance, and although the pulse shortening per pass is small, the cumulative effect in a low-loss cavity may in principle be sufficient to generate 100 fs pulses if cavity dispersion can be precisely controlled. The phenomenon is general, and might be applied to other types of absorber, such as carbon nanotubes or quantum dots. We have shown that the main competing effects in our laser which set pulse duration are the filtering from the gain bandwidth and the optical Stark effect. Future work will investigate the stable pulse energy range and pulse splitting, and the phase structure of Stark mode-locked pulses - our current model is produced in such a way as to make this a simple addition. An extension of the model to include semiconductor Bloch equations will allow investigation of pulse formation at durations comparable with carrier relaxation times. We will consider this possibility as a way of representing the physics of the gain medium more realistically and to incorporate gain filtering and many body effects.

Chapter 5

Terahertz Time Domain Spectroscopy

5.1 Introduction

The terahertz (THz) band of the electromagnetic radiation spectrum lies between 0.1 THz and 10 THz. It sits in the unexplored gap between optical frequencies on one end and high speed electronics at the other end. It is in this THz region that the 'fingerprint' resonances of large molecules are found, which indicates the importance of terahertz radiation. A few commercial THz spectrometers have now been manufactured, but they are bulky and not very portable. The strong absorption of water molecules in this part of the spectrum limited early attempts to use the THz band so more powerful sources and sensitive detection were needed [58].

THz development started from both ends of its spectrum, but has been slow compared to that of optical or microwave frequencies. The slow frequency response of electronic devices limits their usefulness in the THz region, due to the finite carrier mobility and size of these devices. Furthermore, the photon energy corresponding to 1 THz is 4 meV. This, in general, is smaller than any electronic or vibrational laser transition of an atom or molecule, while even narrow band semiconductors such as CdHgTe have orders of magnitude higher bandgaps. One common source for this scale of energy is black body radiation but this is a very low power source. Fig 5.1 shows a picture of the electromagnetic spectrum and highlighted is the THz frequency range. It also shows the black body radiation curve at room temperature. Also shown are the common transitions associated with both the THz gap and its surrounding frequencies. There

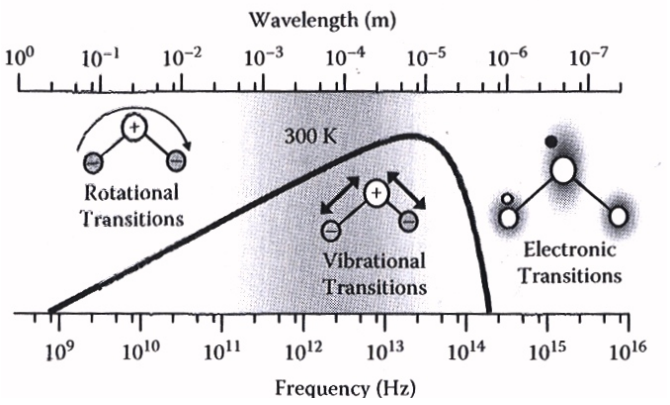

FIGURE 5.1: Electromagnetic spectrum with the THz gap highlighted. The curve represents black body radiation frequency span

are many applications for THz in life sciences and in chemical species detection, since many molecules typically have resonances in this range [59, 60].

Ever since Fork's work on sub-100 fs mode-locked pulses from dye lasers in 1981, the doors became wide open for the generation of picosecond electromagnetic pulses with terahertz frequencies [61] [62] [63]. In 1984, Auston was successful in coherently generating and detecting THz pulses propagating through free space [62] using Terahertz Time Domain Spectroscopy (THz-TDS) techniques described in the next section. Since then a lot of headway was made in this research area but nothing had a more profound effect than the introduction of the Ti-sapphire laser in 1986 [64]. Dye lasers were being phased out in the 1990s by the commercially versatile solid state laser which became commercially available and took the entire research community by storm.

THz-TDS systems based on mode-locked ultrafast lasers are commercially available for applications in pharmaceutical research, quality control and homeland security. Recently, applications in bio-molecule detection and medicine using novel integrated detection schemes such as micro-fluidics, micro-strip lines and evanescent field detection have been receiving significant attention [65] [66] [67] [68].

The development of mode locked vertical external cavity surface emitting lasers (ML-VECSELs) now offers an all-semiconductor source of femtosecond pulses, with the potential to be a cost-effective, compact alternative to Ti:Sapphire and fibre-based THz systems that could address a wider application range.

In 2002, VECSELs have been passively mode-locked with a saturable absorber based on the optical Stark mechanism to produce sub-500-fs pulses at 1040 nm [28]. Since then, mode-locked pulses have been getting shorter and shorter with the latest results showing

70 fs train at 1 GHz repetition rate [31]. We previously demonstrated THz imaging using an ML-VECSEL with an LTG(low-temperature-grown)-GaAsSb antenna; the radiation was detected using a cryogenic bolometer [69].

The work I am reporting here is the first demonstration of a THz-TDS setup using an optical Stark mode-locked VECSEL and photoconductive antennae producing radiation over the range 0.1 - 0.8 THz [70].

5.2 THz Pulse Generation

The generation and detection of terahertz uses a nonlinear response of a fast-response-time material to an incident optical pulse. The methods of doing this are split into two categories, one based on photoconductive antennae, and the other using optical rectification in a nonlinear crystal. The latter relies on nonlinear frequency mixing and is a non-resonant process using the ultrafast change of $\chi^{(2)}$ nonlinearly in some materials by a femtosecond laser pulse. A wide range of materials has been used in this method such as zinc telluride ZnTe at $< 100 >$ orientation and $LiNbO_3$. Our approach, however, uses the Auston switch method [61] which is based on a photoconductive semiconductor antenna. These antenna are made of a semiconductor material with two electrodes of certain shape deposited on top of it. Various examples of these structures that have been used for THz-TDS are shown in 5.2. In this work we use a bow-tie shaped antenna as shown in Fig 5.2-a. The semiconductor material most commonly used is low-temperature(LT)-grown GaAs but other materials with high mobility can also be used.

5.2.1 THz Emission

The process of THz generation and detection involves interaction of optical radiation with the material, generation of hot carriers and their cooling mechanisms, carrier movement under a bias field and screening effects, the shape and size of the antennae electrodes which ultimately dictates the bandwidth and strength of the radiated THz and a host of other effects. A simplified version of the theory will be described in this part of the thesis which is available from various sources as in

On the THz emitter, when a laser pulse is focused onto a gap of the structure in between the two electrodes, carriers are generated in the conduction band provided $h\nu \geq E_{gap}$.

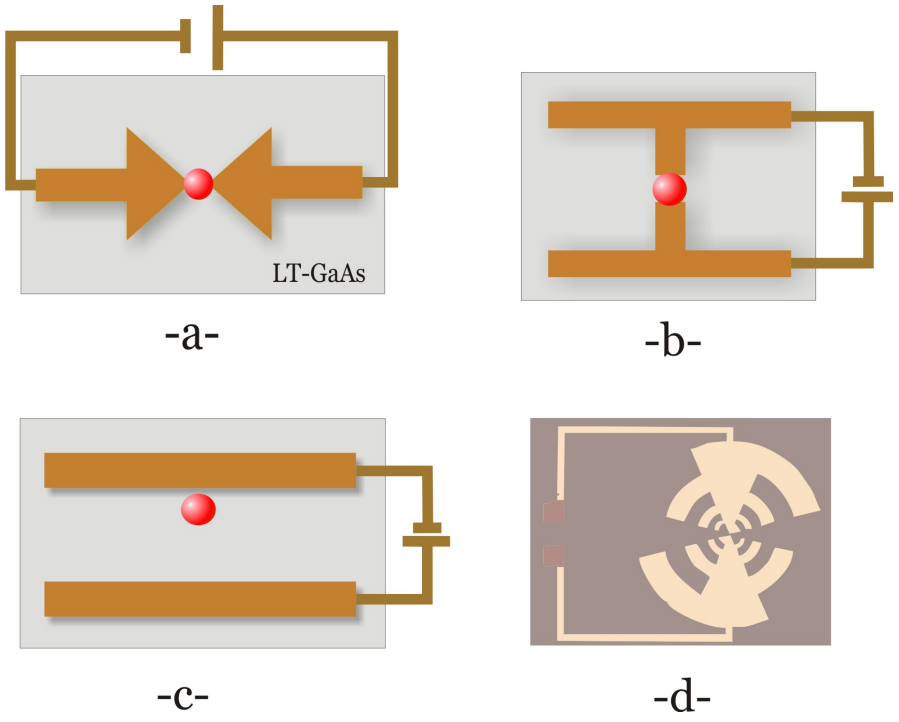

FIGURE 5.2: Some examples of the antenna shapes that have been used for generating and detecting Terahertz: a- Bow tie,b- Dipole, c- Strip line and d-Log-periodic. The application in which TDS is needed dictates the shape of the antenna structure. The red spot represents the focused laser spot.

A bias field of the order of 2.5×10^6 V/m is then applied to the structure. This antenna can be thought of as an energy storing capacitor with a few pF of capacitance.

The photo current density $j(t)$ can be described as the convolution of the pulse shape of the femtosecond pulse $I(t)$ and the response of the antenna

$$j(t) = I(t) \otimes [n(t)qv(t)] = \sigma(t)E \tag{5.2.1}$$

where $n(t)$ is the carrier density , $v(t)$ is their velocity, q is their charge, E is the incident electric field and $\sigma(t)$ is the time dependent conductivity which is given by

$$\sigma(t) = N(t)e\mu \tag{5.2.2}$$

where μ is the carrier mobility. The charge density, $n(t)$, produced at this stage is proportional to the intensity profile of the pulse at low excitation fluences [71, p.1-40]. From the Drude model of free carriers, the time evolution of carrier velocity is given by

$$\frac{dv(t)}{dt} = -\frac{v(t)}{\tau_s} + \frac{q}{m*}E(t) \tag{5.2.3}$$

where τ_s is the scattering time of carriers. It relates the velocity profile of the carriers to the initial acceleration and to the effective mass m^*. The parameter τ_s is characterised by carrier scattering and phonon scattering.

Due to the charge separation of the electron-hole pairs, a 'macroscopic' polarisation is created, given by

$$P(t) = n(t)qr(t), \tag{5.2.4}$$

where $r(t)$ is the separation distance between the clusters of charges. The time evolution of this polarisation can then be extracted from:

$$\frac{dP(t)}{dt} = -\frac{P(t)}{\tau_s'} + n(t)qr(t) \tag{5.2.5}$$

This will ultimately lead to an electric field due to this charge separation being created that opposes and screens the DC field applied to the structure. The effective applied electric field is therefore a combination of these effects and is given by

$$E(t) = E + \frac{P(t)}{\epsilon\alpha}, \tag{5.2.6}$$

where α is a geometry-dependent parameter and E is the applied DC electric field. These equations dictate the time evolution of the current density created by the optical pulse.

The "transient" current element is responsible for generating a terahertz pulse as described by Maxwell's equations. In the far field, a time-dependent current gives rise to a time-dependent electromagnetic radiation field which is given by

$$E_{THz}(t)\alpha\frac{dJ(t)}{dt}, \tag{5.2.7}$$

where J(t) is the time-dependent surface current. Changes in the current distribution in the antenna induced by a femtosecond laser pulse occur on a sub-picosecond timescale, whilst the recovery to the initial state takes typically hundreds of picoseconds [72].

Critical to the temporal response of the antenna and therefore to the temporal profile of the THz radiation is the photoconductive material used in these devices. Photoconductive materials with sub-picosecond response times have been used as terahertz emitters. Their dynamic response depends mainly upon the carrier lifetime, the carrier mobility and the dark resistivity. Short carrier lifetimes are achieved by a generation of a large

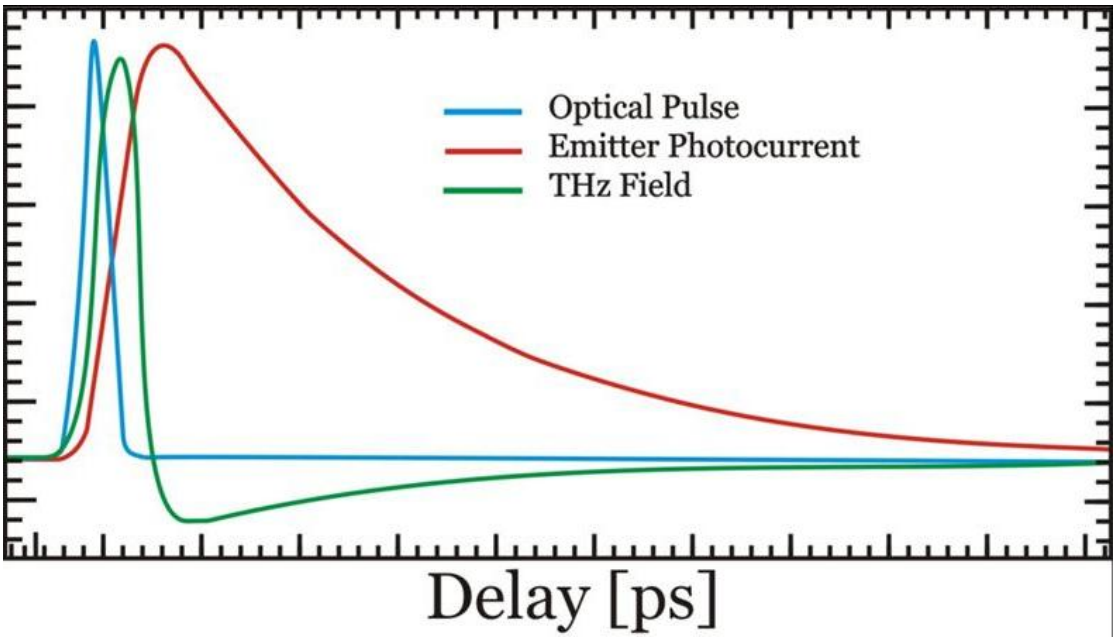

FIGURE 5.3: Temporal picture of the sequence of events leading to the generation of THz radiation field.

density of defects either through an ion bombardment or using specific growth conditions. The corresponding defect energy levels in the band gap then act as carrier traps or recombination centers. Another critical condition for the material of the substrate is to have high dark resistance that minimizes current flow and heating effects locally and protects the device from electromigration where the antenna is short-circuited and rendered useless [73, p.192]. Fig 5.3 taken from [74] shows the relationship between the three ingredients in the process of generating THz; the optical pulse creating electrons and holes, and the generated current and the emitted THz field are determined by the time derivative of the current [75]. It is worth noting from the figure that most of the THz radiation is generated during the carrier rise time. The positive peak in the THz field graph can be interpreted as radiation due to carrier generation where the negative peak is due to carrier decay. This has been shown by Tani et al in [76].

5.2.2 THz Detection

Once a terahertz pulse is generated, it travels through a certain thickness of the semiconductor material. The THz pulse will be collimated due to the fact that most semiconductors have high refractive indices at terahertz frequencies. Good directionality of the THz beam helps in improving the efficiency of a THz spectrometer [77].

The detection of THz radiation is based on the same principles as the generation process described above. In order to detect the electric field, the response time of the detector material must be very short and its mobility must be high. A femtosecond laser pulse is focused onto the antenna gap to create carriers, but no static bias is applied to the gap, and therefore no current is flowing. These antennas typically have dark resistance (when no pulses are focused onto them) of the order of several megaohms. The creation of carriers leads the resistance to drop to few megaohms, or even a few hundred ohms depending on the material properties. The electric field of the emitted THz pulse can provide a transient bias voltage across the gap, and if the arrival time of this pulse is timed to coincide with the arrival of the femtosecond pulse, a photocurrent is induced that is proportional to the THz pulse's electric field. Since the laser pulse is narrower than the THz pulse, the former can act as a sampling signal provided the receiving antennae is fast enough. The time domain signal, $i(t)$, will be the convolution of the THz pulse electric field and the detector response represented by its conductivity $\sigma(t)$;

$$i(t) = \frac{1}{T}\int_0^T E_{THz}(\tau)\sigma(t-\tau)d\tau \tag{5.2.8}$$

where T is the laser repetition rate. Ideally, in order to sample the electric field efficiently, a delta-function-like photoconductor response is required with a similar delta-function-like pulse. However, in real life a tradeoff is made between short lifetime and semiconductor mobility, because in order to have short carrier lifetimes more defect states are needed which leads to reducing the mobility and hence the material conductivity. The most common materials used in THz detection are low temperature grown GaAs (LT-GaAs), where the low growth temperature determines the carrier lifetime due to the number of defects, and silicon on sapphire where ion implantation is used to reduce lifetimes.

5.3 Coherent Generation and Detection of THz

5.3.1 Experimental Setup

The ML-VECSEL comprised of an optically pumped, surface-emitting, near anti-resonant gain structure containing 6 InGaAs/GaAs quantum wells, forming one folding mirror of the Z-shaped external cavity. A 50-mm radius 0.7% transmitting output coupler completed one end of the cavity; and a 25-mm radius highly reflecting folding mirror focused the cavity mode onto the optical Stark semiconductor saturable absorber mirror

(SESAM) at the other end. A schematic diagram of a ML-VECSEL is shown in Fig 5.4 and a detailed description of the gain structure can be found in [28]. The laser cavity length corresponded to a fundamental repetition rate of 1.2 GHz. The gain structure was optically pumped with 1.3 W at 830 nm, from a commercially available fibre-coupled diode. The laser mode and pump spot on the gain structure had radius 60 microns and the laser mode had a radius of 15 microns on the SESAM. The laser produced pulses of duration 480 fs shown in the intensity autocorrelation of the output pulse train from the ML-VECSEL in Fig 5.5. The optical spectrum of width 3.2 nm at full-width-half-maximum was centered at 1044 nm; the pulses were 1.9-times-transform-limited at an average output power of 34 mW.

The experimental setup used in this project was that of a conventional time domain spectrometer. Fig 5.6 shows schematically the arrangement used for most of the experiments. The output of the mode-locked VECSEL described is split in two with a beam splitter (BS). One part of the beam is focused with a 4 mm-focal-length lens onto the centre of a bow-tie shaped THz emitter. The emitter is connected to a function generator used to bias the emitter by an oscillating voltage of 10 V with a frequency of 20 KHz. The other part of the laser beam goes through a mechanical delay line and is focused onto a receiver antenna by a 4 mm-focal-length lens. The electrodes from this antenna are connected to a lock-in amplifier which together with the delay line are controlled by a computer. The amplifier is used to measure the weak signal (pAmps) detected by the receiving antennae through a lock-in frequency set by the frequency generator. This should be set well away from dc noise frequency. An alternative option to this configuration was to use a DC power supply to provide the bias for the emitter and use a chopper to cut off the emitter laser beam path. Not a huge difference was observed in terms of noise levels with either of the two configurations.

Being invisible, the VECSEL beam proved to be difficult to use for alignment, so the THz beam path was aligned with the help of a He-Ne laser. A small pinhole was used in front of one of the lenses and its diameter was set so that a circular diffraction pattern can be seen filling the whole parabolic surface of the first mirror. The latter was positioned one focal length of the mirror away from the focus of the lens, so that the reflected red laser light was collimated in the far field. A second parabolic mirror was then placed in the path of the beam and positioned so that it produced a perfectly circular focus one focal length distance away from it. After that another parabolic mirror was positioned one focal length away to collect and collimate the diverging radiation and finally one last mirror was positioned so that it focused this radiation onto the receiving antenna.

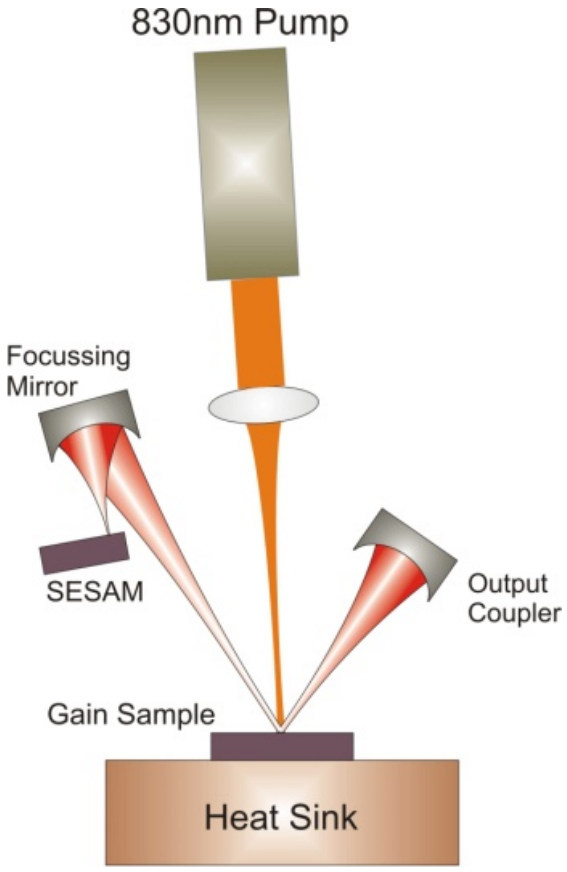

FIGURE 5.4: Schematic diagram of a mode-locked VECSEL

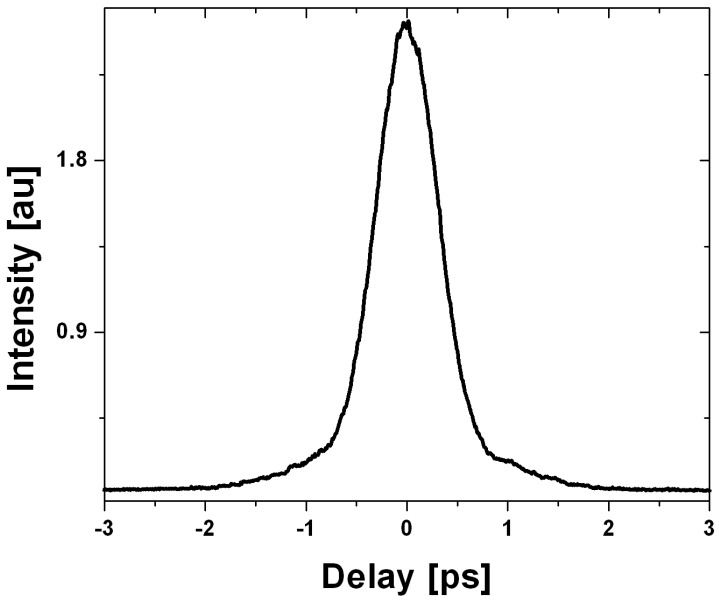

FIGURE 5.5: An autocorrelation of a pulse from the VECSEL

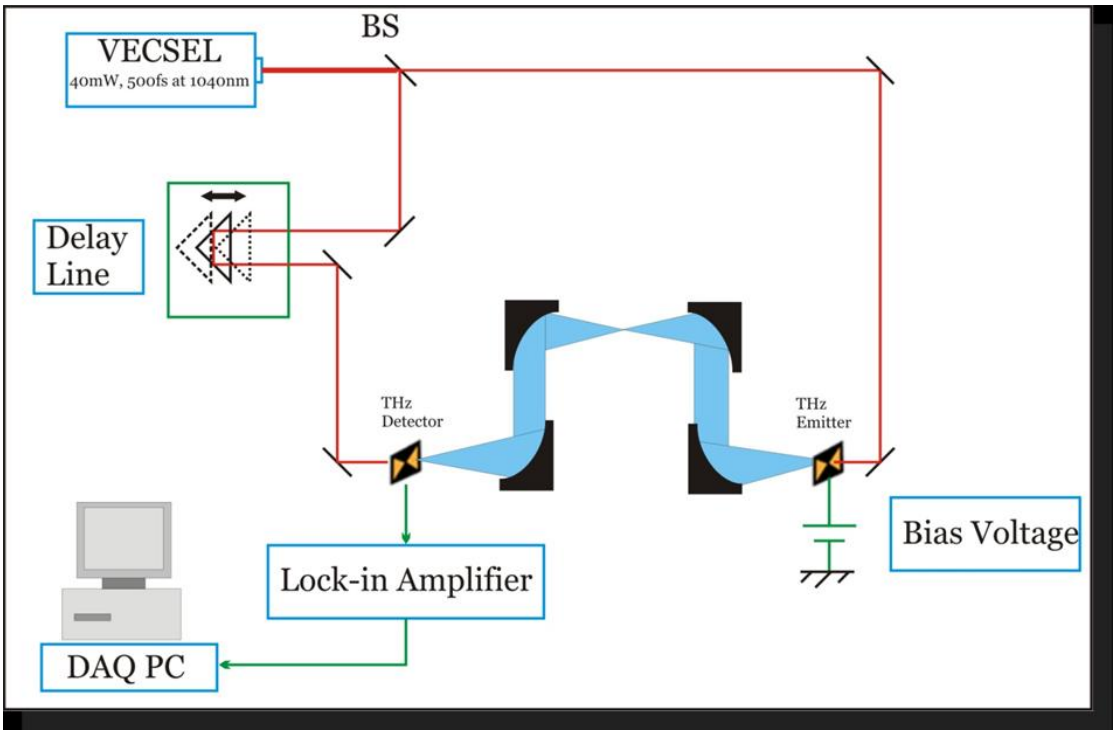

FIGURE 5.6: A schematic of the THz-TDS setup

5.3.1.1 GaAsSb Antenna

Our first attempt at coherently generating and detecting THz was using low-temperature-grown gallium arsenide antimonide (LT-GaAsSb). It was thought at the time that GaAs-based material does not make efficient photoconductive antenna with excitation wavelengths above 860 nm, so we were exploring materials with smaller bandgap that could be pumped by the 1040 nm VECSEL.

The work done on GaAsSb was in collaboration with Prof. Koch's group at Braunschweig University and Prof. Hartnagel's group at Darmstadt University. The material had already been shown to work in THz imaging [69] using the same VECSEL laser. An LT-$GaAs_{0.81}Sb_{0.19}$ layer was grown on top of a GaAs substrate by molecular beam epitaxy (MBE) at 490^{o}C. The composition was recommended as corresponding to a bandgap wavelength of 1060 nm. However, the measured reflectivity spectrum is not consistent with this model. Figure 5.7 shows the transmission spectrum of a 500-μm thick layer of LT-$GaAs_{0.81}Sb_{0.19}$. At the operating wavelength of the THz spectrometer we built, the antennae sample is highly reflective. The antenna structure used in the initial experiment was similar to Fig 5.2-d. The log-periodic design with the different arms gives, theoretically, a broader bandwidth. Each two arms act as a dipole having a different resonance frequency unlike, for example, a parallel strip-line antenna which

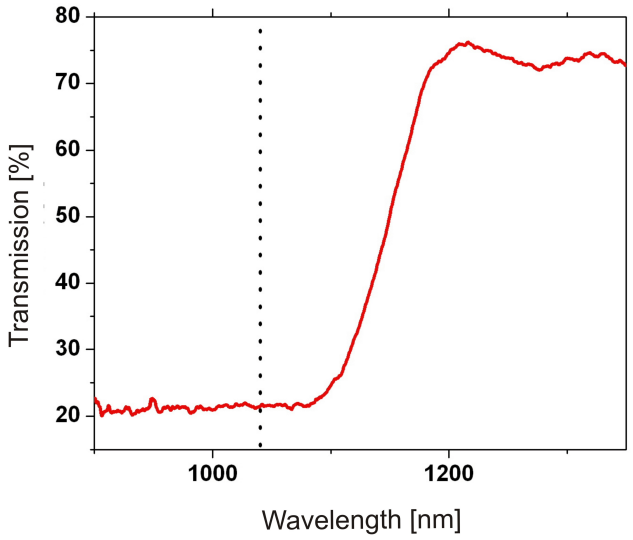

FIGURE 5.7: Measured transmission spectrum of an LT-GaAsSb layer. The dotted line represents the wavelength of the laser used in the THz experiment.

has a single resonance frequency defined by the separation between the lines [78, 79]. The centre of the antennae contains interdigitated small arms in a gap of about 2 μm. The efficiency associated with this design comes at a price as it makes it fragile in the presence of a strong bias voltage and electrostatic discharge. In fact this structure was destroyed just two days into the initial testing.

A new H-structure was grown on the GaAsSb material with 4 mm long strip lines separated by 40 μm and with a centre gap of 8 μm. This structure showed about 45 MΩ dark resistance and 92 kΩ resistance when 30 mW of incident power. This resistance proved too small to generate any terahertz and none of the terahertz scans taken showed any signs of the radiation being detected.

5.3.1.2 LT-GaAs & LT-InGaAs Combination

Our second attempt was using an LT-GaAs antenna as an emitter and an LT-InGaAs antenna as a receiver [80]. LT-InGaAs and LT-GaAs with lifetimes 0.55 [80] and 0.2 ps respectively were compared in the setup; surprisingly, there was not a significant difference in their performance. The advantage of shorter carrier lifetime in LT-GaAs may compensate for its lower absorption efficiency. We chose the LT-GaAs antenna as an emitter because of its durability and robustness. The below-band-gap absorption most likely arises from mid-gap defect states in the antenna material, as reported for SI-GaAs [81], and for low temperature grown GaAs [76], where a two-step photoabsorption

mediated by mid-gap states is the dominant process for photoconductivity [76]. These antenna technologies were developed by the University of Cambridge in conjunction with TeraView Ltd.

5.3.2 Results

The antennae was illuminated with 10 mW optical power each, and a bias voltage of 20 V was applied to the emitter antenna. The bias voltage was electrically modulated at 20 kHz, and a lock-in amplifier was used to detect the photocurrent on the receiver at the chopping frequency. Both antennae were patterned with a gold bow-tie shaped electrode with a gap of 5 microns. The emitter and receiver antennae had dark resistances of approximately 10 MΩ and 30 MΩ respectively; which fell by nearly a factor of 10 when illuminated by the output of the VECSEL. Emitted radiation was collected and focused using a combination of two silicon (Si) lenses positioned behind the emitter and in front of the receiver. The mechanical delay line was used to vary the arrival time of the probe pulse versus the THz pulse and hence the photocurrent recorded is proportional to the THz electric field. A Fast Fourier Transform (FFT) was performed on this time domain trace to obtain the amplitude of the frequency response of the system. The average receiver current is shown as a function of pulse arrival time in Fig. 5.8, where the echo is believed to originate from a reflection off the Si lens. The lock-in time constant used for the scans was 300 ms. THz radiation is generated over the bandwidth of 0.1 - 0.8 THz above the noise floor, as can be seen in Fig. 5.9; the frequency resolution of this scan is 13.6 GHz. The water absorption lines in the frequency range are found at 0.555 and 0.751 THz in good agreement with the literature [82].

A Coherent Microlase Nd:YLF served as a reference laser, with pulse width variable from 150 to 800 fs, a 120 MHz repetition rate and 1047 nm central wavelength; it was used to investigate the effect of pulse width on the THz signal. Similar lasers have been used in the literature for the generation of THz pulses for time domain setups [80]. The comparison of the THz spectra from the VECSEL and from the Nd:YLF laser operating with can be seen in Fig 5.10 and Fig 5.11. We can see that the VECSEL creates a lower THz signal and a smaller bandwidth than the Nd:YLF laser working at a comparable pulse length (512 fs). The 1-ns period between pulses in the VECSEL pulse train is orders of magnitude higher than the carrier recombination time (usually around 0.5 ps), therefore long enough for the carrier population to relax. However, the energy per pulse of the VECSEL is 10 pJ whereas the energy per pulse for the Nd:YLF laser is greater

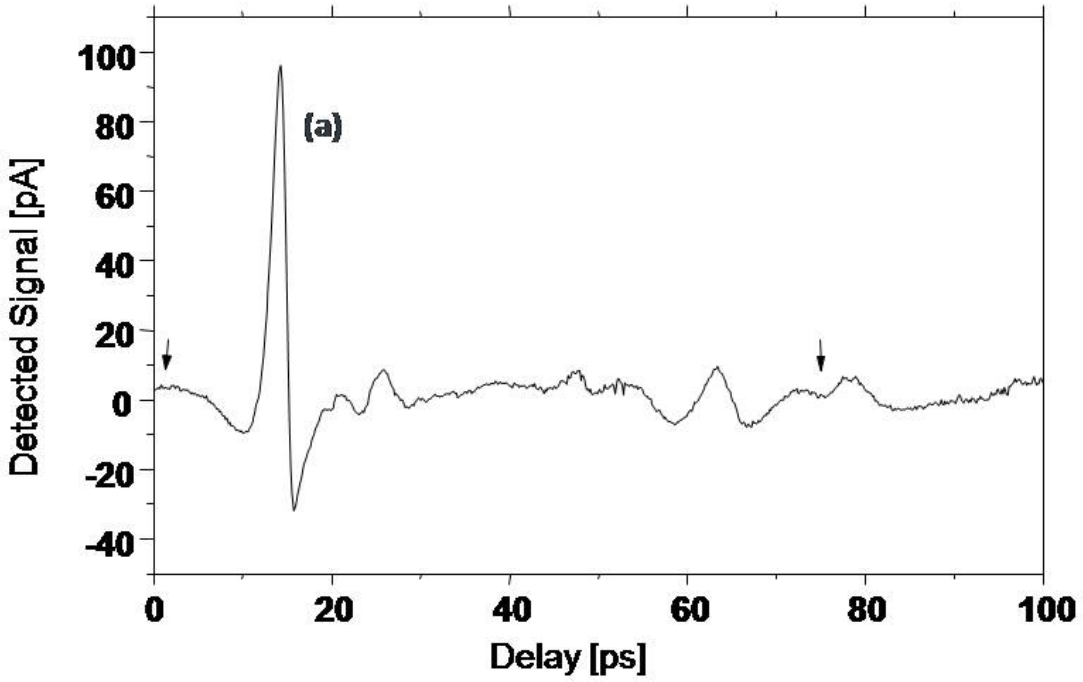

FIGURE 5.8: Antennae current as a function of time delay, pumped by 480 fs pulses from a VECSEL. The arrows indicate the Fast Fourier Transform window.

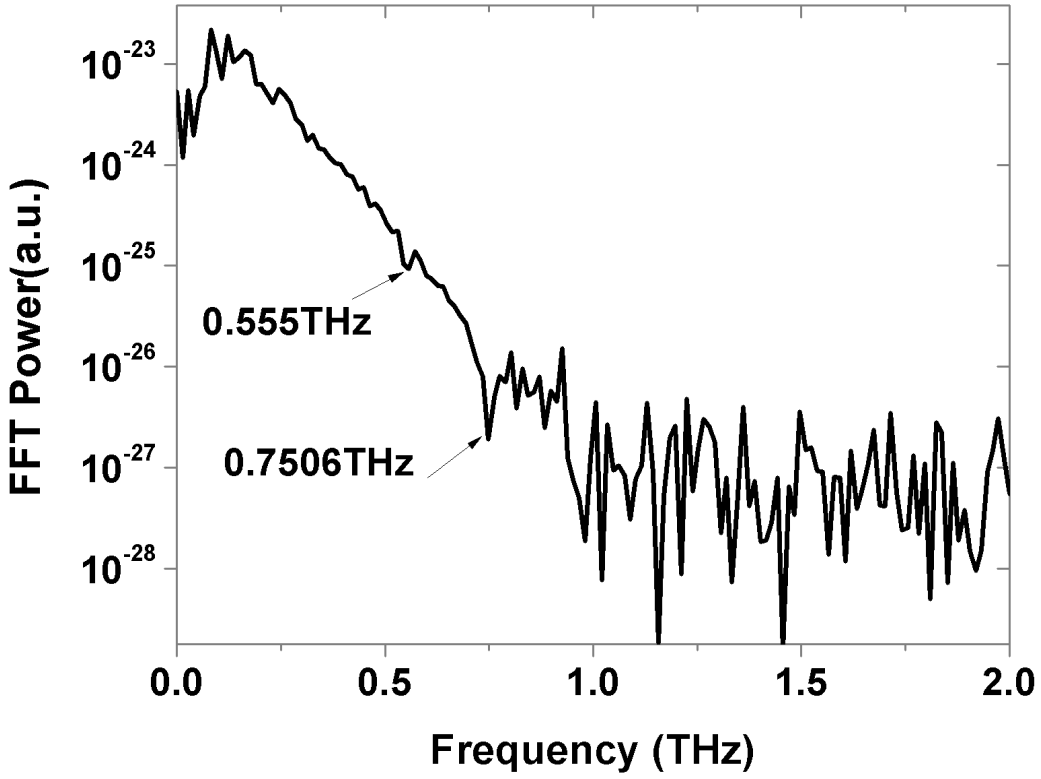

FIGURE 5.9: FFT of the time domain signal in Fig. 5.7. with arrows showing water absorption lines

than 50 pJ. It is likely that the bandwidth is limited by the increase in the noise floor due to the smaller THz transients generated by the VECSEL laser system. This shows that the THz bandwidth is limited by the power and/or the stability of the VECSEL source.

Theoretically, the higher repetition rate should improve the signal to noise ratio, because the noise level increases with the square root of the number of sampling pulses whereas the signal level increases linearly. This is also confirmed experimentally in a THz system according to Mouret et al. [83]. Consequently, by increasing the average power, decreasing the pulse width and improving stability it is expected that the VECSEL will eventually match or surpass the bandwidth and signal-to-noise achieved with the conventional Nd:YLF laser. High repetition rate lasers have been used successfully for THz generation [84], however the dependence of THz signal to laser repetition rate was never thoroughly investigated to our knowledge. The VECSEL is a very convenient platform for such a study since we can vary the repetition rate by varying the length of the cavity while we keep an approximately stable pulse shape.

5.4 Future Work

We have been able to demonstrate the first all-semiconductor room-temperature terahertz time-domain spectrometer. This in itself has some great potential as the way forward for making very compact sources and detectors for THz which creates many possibilities for applications. Mobile detectors can theoretically be made and moved around with no problems compared to the bulky systems that are available which use Ti:Sapphire lasers.

As the system is in its early stages of development, plans are in place to characterise the ideal combination of parameters to make it more efficient and robust. We will use VECSELs with higher average powers and study the dependence on different repetition rates by using ML-VECSELs with different cavity lengths. A recently demonstrated 260 fs ML-VECSEL in our group will be used to extend the bandwidth to 2 THz. Furthermore, the recent demonstration of offset-repetition rate locking of VECSELs can be used to increase stability and thus performance of the system [85]. Fibre amplifiers can also be used to drive wide band antennas for higher power THz sources. These innovations will allow us to produce a highly compact and integrated THz-TDS system.

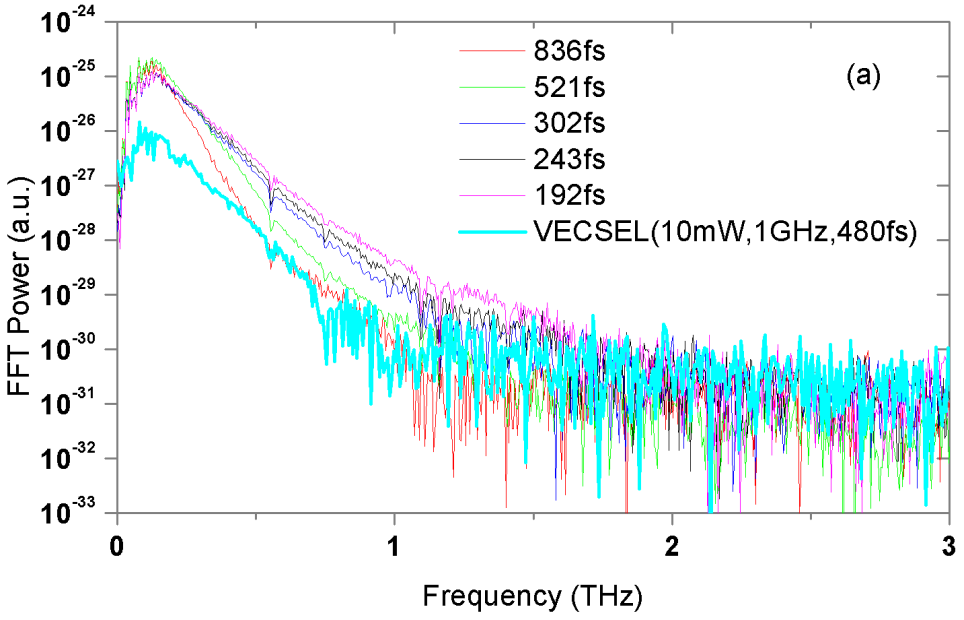

FIGURE 5.10: Comparison of the THz spectra obtained by the VECSEL and by the Nd:YLF laser at different pulse widths

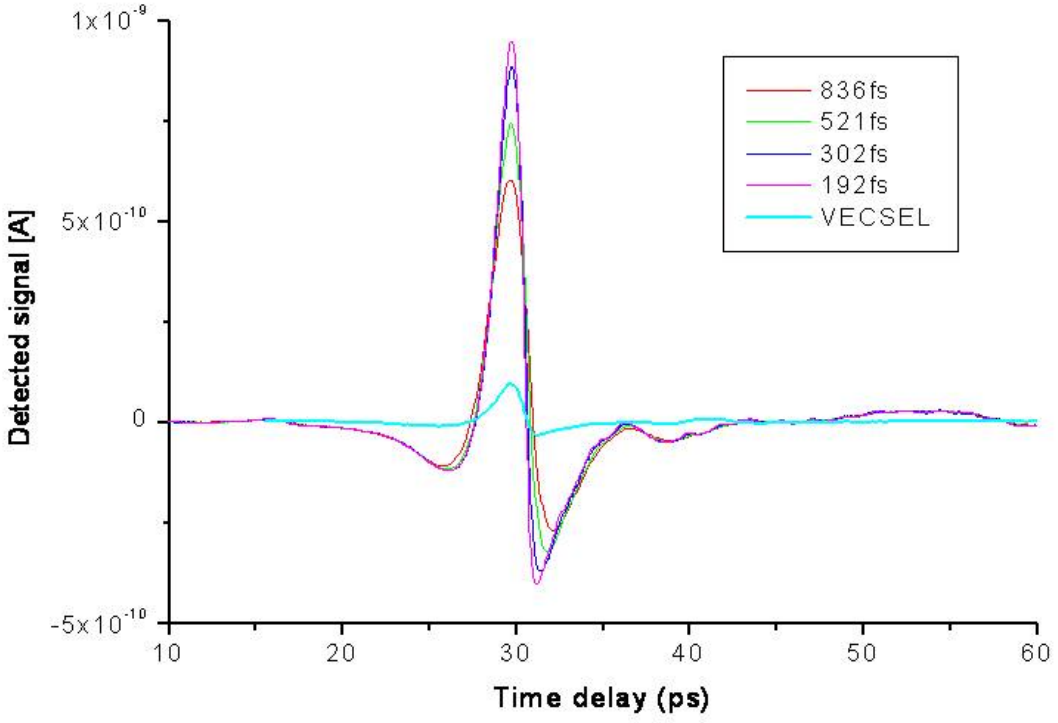

FIGURE 5.11: THz time domain traces

A mode-locked VECSEL producing short pulses at a wavelength of 835 nm is in the early stages of development, which will allow us to fully benefit from LT-GaAs material that is mainly used with Ti:Sapphire lasers. Chapter 6 describes my work on the 835 nm VECSEL which so far has produced 15 ps pulses.

Chapter 6

Compact, High Repetition Rate 830 nm Mode-Locked VECSEL

6.1 Introduction

Different solid state lasers have been mode locked and produced the shortest pulses available. Pulse durations of less than 100 fs are easily achievable from a passively mode locked Ti-Sapphire laser. Pulses shorter than 10 fs are also possible with very high precision dispersion compensation [86, 87]. Development of VECSELs in the 830 nm wavelength region would open the door for an array of applications that emerged since the introduction of the Ti-Sapphire with the added incentives of compactness, cheapness and versatility. Most of the attractive developments in the VECSEL domain are restricted to the near infrared region of the spectrum. We hope to take the advantage of the experience and technology gained in this area and move to the 830 nm region.

In this chapter, the first demonstration of a passively mode locked OP-VECSEL operating at 832 nm, producing pulses of a duration of 15.3 ps, is presented. I will start by describing the gain sample and SESAM designs then I will describe the pump system built specially for this project due to the lack of a commercially available red pump providing more than 1 W of power. I will then show results of the successful lasing of the samples and also results of mode-locking the laser and finally give a summary with future work ideas to take advantage of the very promising initial results. The work presented in this chapter was published in [88].

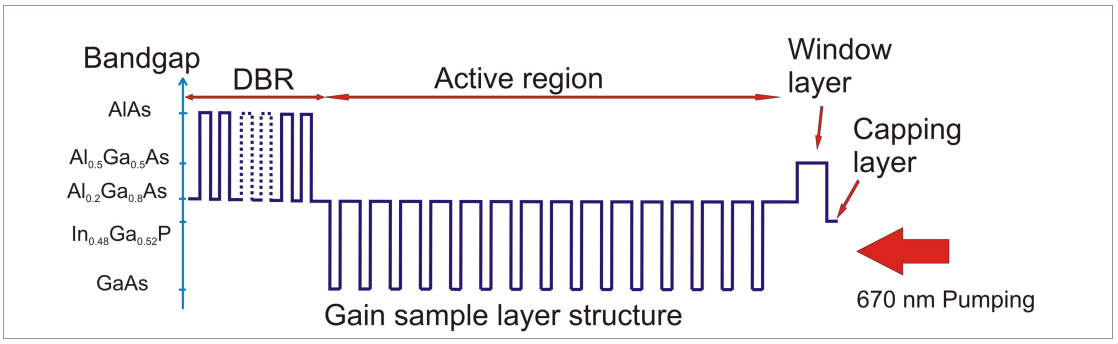

FIGURE 6.1: A schematic of the gain sample layers grown using MOCVD

6.2 Gain And SESAM Sample Designs

The designs of the gain sample and SESAM were made by our group and then sent for growth at NAsP$_{III/V}$ GmbH in Marburg, Germany. The design wavelength for these samples was at 840 nm for the SESAM and 835 nm for the gain. The layer lists are included in appendix A.

For the case of an 830 nm VECSEL, using data from Fig 2.2, the material of choice for the quantum wells was chosen to be GaAs. The pump absorbing layers on either side of each quantum well were chosen to be AlGaAs. For this composition, the best option to take was to build a pumping module at 670 nm. Using the bandgap energy formula for $Al_xGa_{1-x}As$ from [89], E_{gap}(eV)=1.424+1.247x for x<0.45, we can find that the aluminum composition needed to make the material absorb a 670 nm-radiation must be less than about 0.3.

The layers of the gain sample used in this experiment are shown schematically in Fig.6.1 contained 15 x 6 nm-thick GaAs/$Al_{0.2}Ga_{0.8}As$ quantum wells positioned at the antinodes of anti-resonant micro-cavity formed between a 30-pair Bragg reflector and the air surface. The $Al_{0.2}Ga_{0.8}As$ barriers also act as pump absorber layers. A similar structure at Strathclyde University has been used with an intracavity heat spreading plate to demonstrate 0.5 W of continuous-wave power at 850 nm, optically pumped with 2.9 W of 670 nm power [19]. It was not possible to use a heat spreader in this experiment in order to avoid intracavity etalon effects. The gain sample was pumped with the combined output from two 1-W commercial 665 nm diodes.

The SESAM used consisted of an AlAs/$Al_{0.2}Ga_{0.8}As$ DBR, a spacer layer of $GaAs_{0.75}P_{0.25}$, a 4.8 nm GaAs quantum well and a 2 nm-thick capping layer of $GaAs_{0.79}P_{0.21}$. A schematic of the SESAM structure is shown in Fig 6.2. The spacer layer thickness was chosen so that the quantum well was located 0.68 xλ/4 from the interface with the DBR.

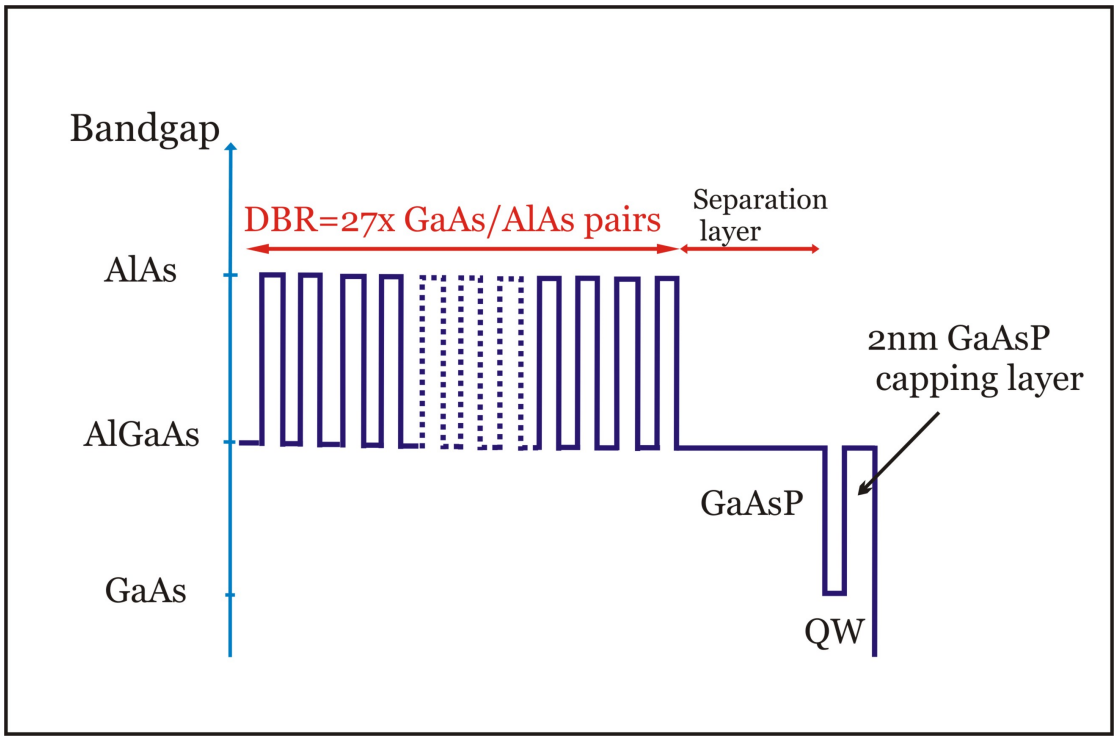

FIGURE 6.2: A schematic of the SESAM layers grown using MOCVD

The GaAsP capping layer is vital for fast carrier recombination in this quantum well system as it allows a high surface concentration of As defect sites, which are primarily responsible for providing the surface recombination states.

Pump probe measurements were performed on the SESAM using a titanium sapphire laser operating at 855 nm to measure the absorption recovery time. This work was done at ETH Zurich by Adrian Quarterman. The pump pulses had an incident fluence on the SESAM of 100 μJcm^{-2}. Fig 6.3 shows the reflected probe signal against delay, revealing the absorption recovery characteristics of the SESAM. The absorption recovery has a bi-temporal shape with a fast component with a recovery time of the order of 1.5 ps, which corresponds to about two thirds of total absorption. Then a slow component is observed with a recovery time of around 200 ps.

6.3 Red Pump Set-up

The VECSEL gain samples for this project were designed to have a CW-pumping wavelength of around 665 nm. Due to the lack of a commercial product that satisfies our need of greater than 1.5 W of power of red laser, we decided to build one using two single-emitter diode lasers from nLight grown using MOCVD techniques. Fig.6.4 shows

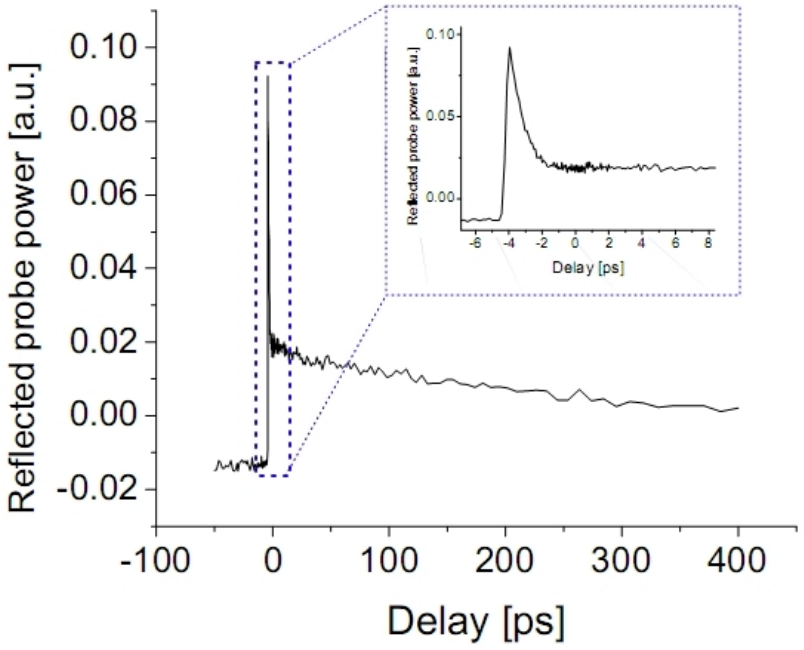

FIGURE 6.3: Pump and probe measurement of reflected probe beam intensity, showing fast recovery time of 1.5 ps; slow component recovers with characteristics time of 200 ps

the schematic picked for combining the output of the two diodes. The pump module that was built is similar to the one described by Dr. Jacob Mackenzie in his PhD thesis[90].

The two diodes emit 1 W of CW-power each at a centre wavelength of 665 nm at 25^oC. They have beam divergences of 42^o for the fast axis and 10^o for the slow axis. Each diode is mounted on a separate block of aluminum that acts as a heat sink and is in contact with a Peltier cooling element to control its temperature. The laser diodes were found to operate down to around 12^oC temperature without causing damage to them. The cooling devices removed waste heat and allowed for extra power to be extracted out of the two diodes. Both diodes were connected in series and a 4.5 A current driver was used as a power supply. The two Peltier elements were also connected in series and their temperature is controlled using a single home-built temperature controller to help keep consistent operating conditions for both diodes. The controller used simple PID principles to set the temperature accurately with the help of feedback from a PT100 temperature sensor.

Similar optical arrangements for collimation were used with both diodes. An n-Light 1 mm-focal-length plano-convex lens was used to collimate the fast axis and a 4 mm-focal length lens was used to collimate the slow axis. These were positioned and later glued with the help of a translation stage, while great care was taken with the slow-axis

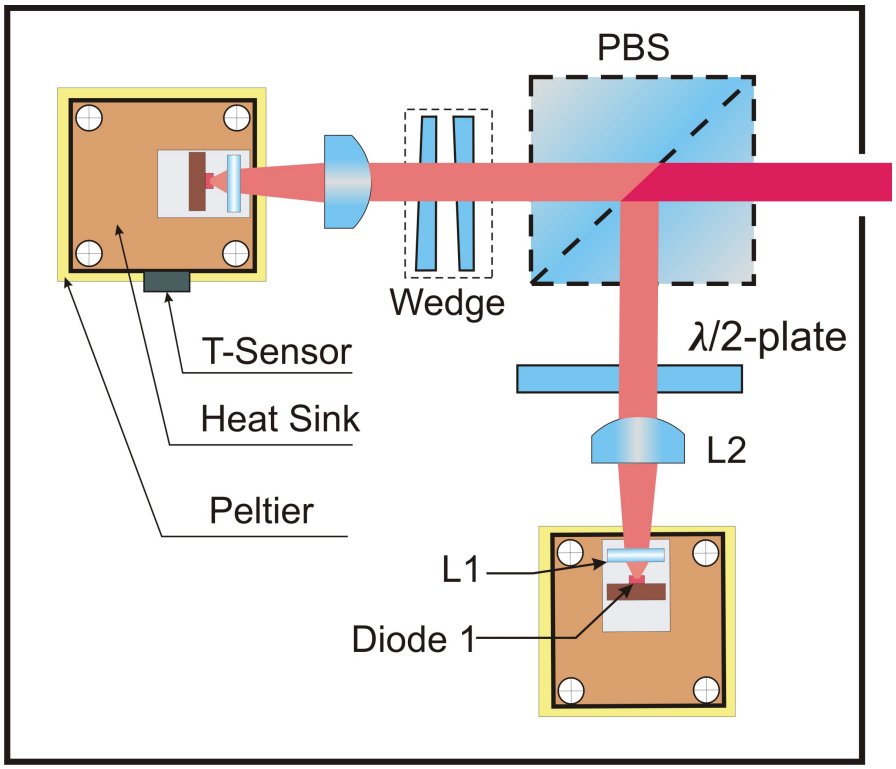

FIGURE 6.4: Schematic of the red diode source setup used for pumping the 832-nm VECSEL. L1 is a 1-mm-focal length cylindrical lens, L2 is a 3.8-mm-focal length cylindrical lens and PBS is a polarising beam splitter

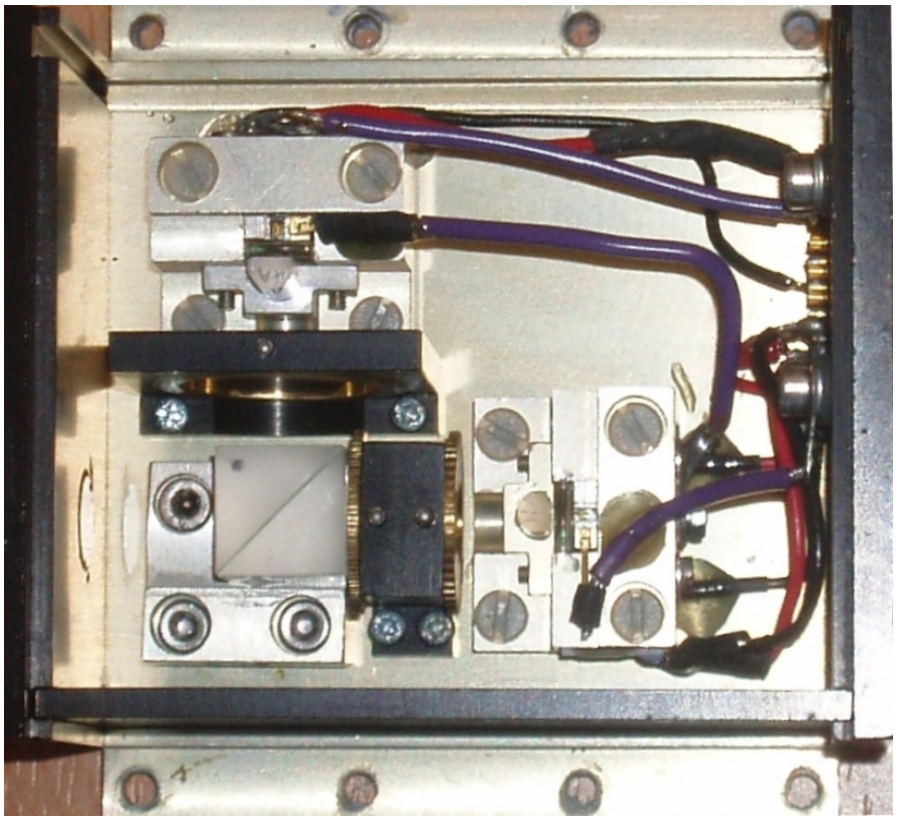

FIGURE 6.5: A picture of the pumping module built in a workshop

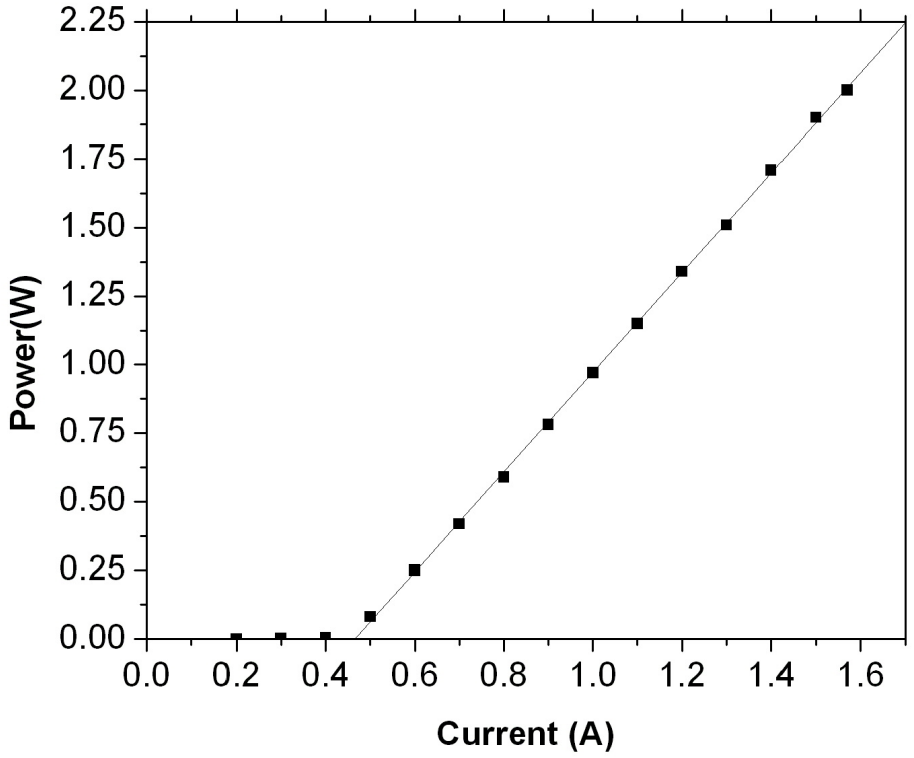

FIGURE 6.6: Output power from the fibre is plotted against the driving current at T=15^o C.

collimator as to not damage the facet of the diodes. The use of glue was later found to be ineffective in holding the lenses in place due to all the heat generated by the diodes so a curable cement was used instead. As both diodes sit in the same configuration on top of the metal blocks, a half-wave-plate was used to rotate the polarisation of one of the diodes. Then the two collimated beams were joined up together using a polarising beam splitter (PBS). Two circular wedges were placed in front of one of the diodes as another degree of freedom to help with beam steering over around 8^o. An anodised box was used to house the pump setup and was made so it was possible to clamp it down for stability. All optical elements inside were anti-reflection coated for 630 nm to prevent losses. Fig 6.5 shows a photo taken of the completed pumping device.

A first attempt to focus the collimated output of the two diodes proved ineffective in getting the required pump spot size on the gain. When focusing in this way, it was observed that there was a mismatch between the two foci laterally. This was realigned by adjusting the screws on the metal block. It was found later that a better way to combine the output of the two diodes was to use an optical fibre. A 4 mm-focal length lens was used to couple the output into a 40 μm-diameter fibre. Up to 2 W was coupled into the

fibre which was enough theoretically to provide more than the threshold requirement of the VECSEL. Another 4 mm-focal length lens was at the other end of the fibre to collimate its output. A 10 cm-focal length lens was then used to focus the fibre output onto the gain sample. A spot size of around 100 x 200 μm was achieved at the focus of the beam. This had an elliptical shape which was taken into account when designing a laser cavity around the gain sample. Fig 6.6 shows the output power of the combined setup as a function of the driving current of each diode. The data were taken whilst the temperature of the diodes was set to 15^o C.

6.4 Experimental Results

The initial characterisation to be done, as with samples in Chapter 2, was the measurement of top and edge photoluminescence (PL) emissions. A small 1 cm x 1 cm piece of gain sample was cleaved from the 2 inch by 2 inch wafer. This piece was then mounted as usual on a heat sink in contact with a Peltier element. Next, the sample is pumped with different powers and at different temperatures set by the Peltier element. Fig 6.7 shows the results for top and edge PL at room temperature which was in this case 20^o C. In this figure, PL intensity is plotted on a log scale against wavelength. To help understand these results, the same data from (a) and (b) in Fig 6.7, which correspond to top and edge PL respectively, are plotted on the same scale in Fig 6.8. The important piece of information to take from this graph is that there is a sizeable difference in the emission wavelengths of top and edge PL. Since the two PLs shift by different rates with pump powers and temperatures, we would have to operate the sample in extreme cold conditions to get the two PLs emissions to overlap and, consequently, for lasing to be initiated. Since our design program was checked rigorously for errors to no avail, a conclusion was drawn to the effect that a mistake in the growth has been made by the grower. Either some layers were missed and not grown at all, or there was an over growth of layers in terms of their thicknesses.

One last attempt to investigate this was done by looking at a cross section of the cleaved sample of a sample under a Scanning Electron Microscope (SEM). Fig 6.9 shows a picture taken of one of the investigated samples. The picture shows two things: A clearly resolved DBR region with its multiple layers highlighted by the different contrast ratios and also the active region of the gain sample along the window layer at the sample/air interface. What is interesting is that we are able to measure the length of the active region and this comes out to be about 812 nm where our design list dictates a length

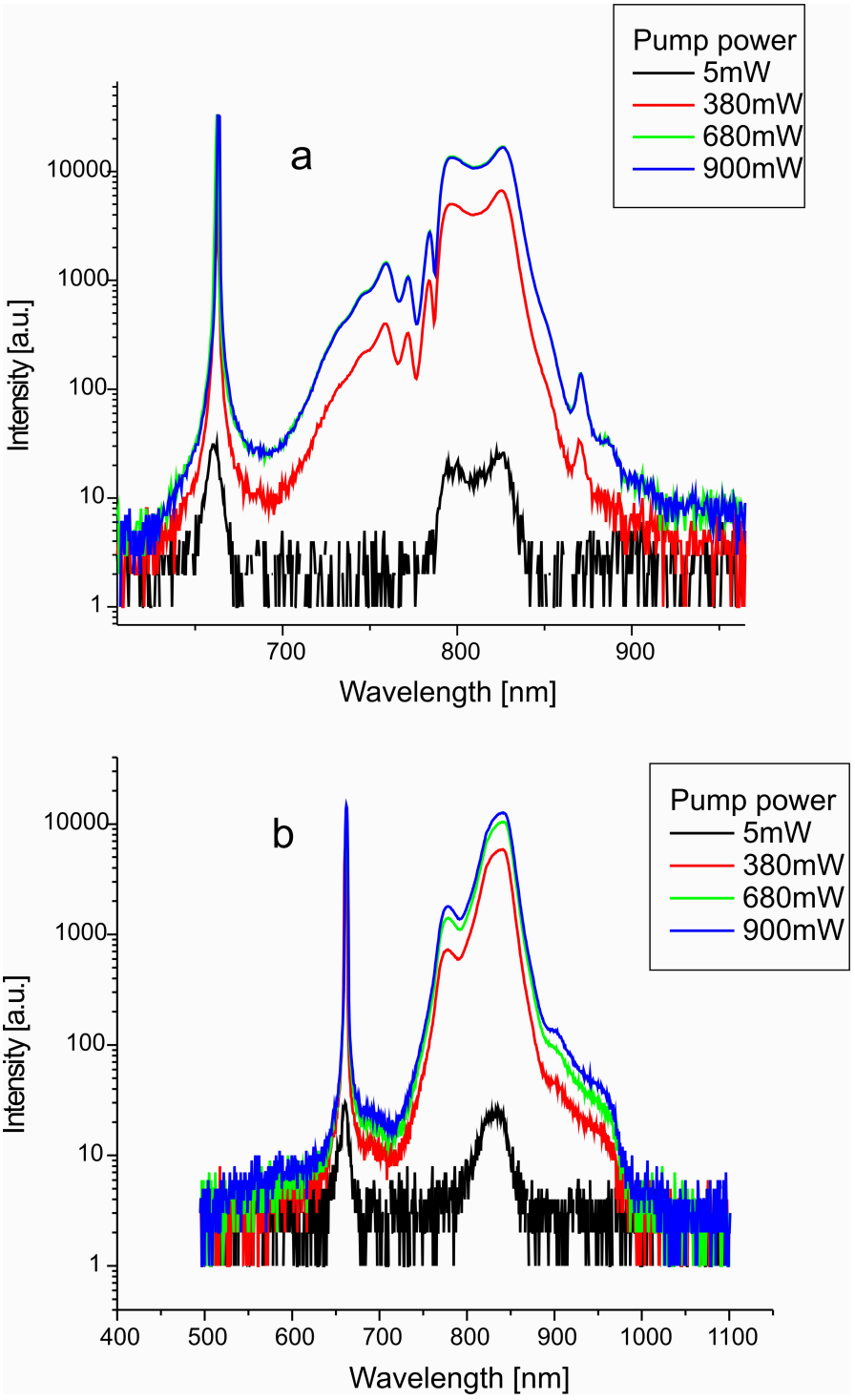

FIGURE 6.7: PL measurements on one of the NAsP samples at 20°C. The top graph (a) is the top PL for four different pump powers while (b) is the edge PL for the same four pump powers.

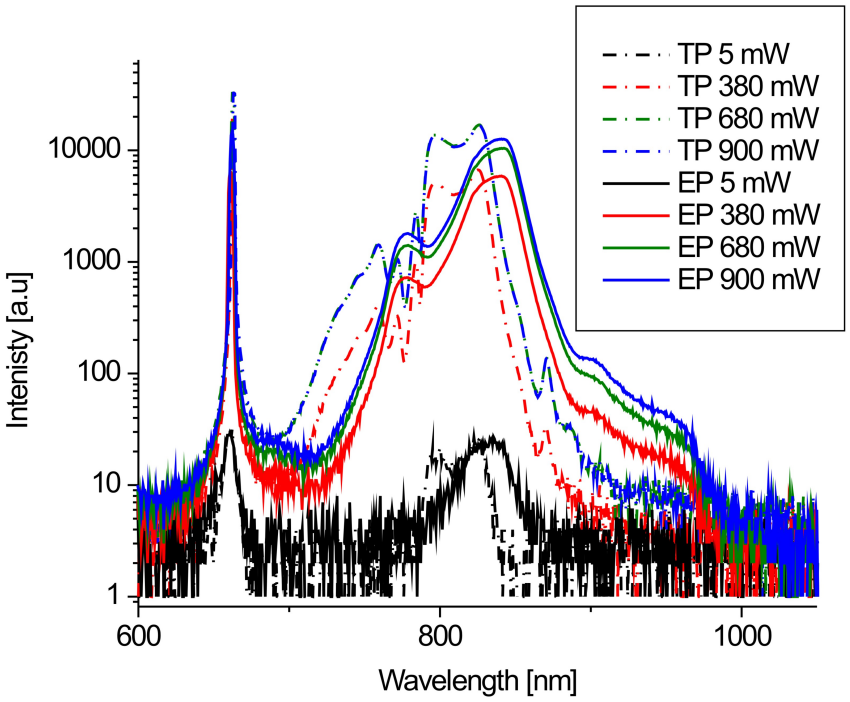

FIGURE 6.8: Top and Edge PL plotted on the same wavelength scale.

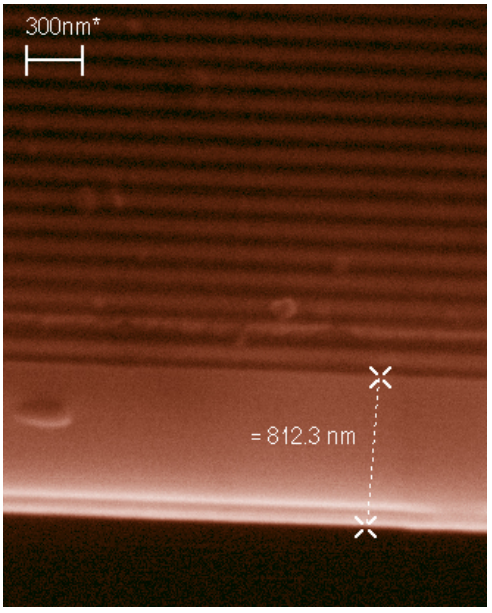

FIGURE 6.9: SEM picture of part of the DBR and the whole of the active region of an 850 nm VECSEL sample

of about 1 μm. We believe that the missing layers are two quantum wells with the surrounding barriers. It was then decided that these samples are not going to be useful for this project.

Not to be deterred by this disappointment, we established a collaboration with the Institute of Photonics (IoP) in Strathclyde and managed to obtain a single piece of gain sample which we used along with one of the SESAMs grown at $NAsP_{III/V}$ GmbH. The results from these experiments are discussed in the rest of this section.

6.4.1 CW Operation

CW lasing characteristics of the gain sample were tested in two configurations. A straight cavity was built consisting of a 50 mm-radius of curvature 0.7% output coupler as one end mirror and the gain sample as the other end mirror. This cavity was used to test the sample and look for optimal pump positions. The gain sample we ended up using was the last surviving piece from a 5 cm x 5 cm wafer which was dropped and broken to pieces. The gain sample was mounted on a Peltier element to control its temperature. At -9^{o}C, we obtained 96 mW of CW output power with about 1.5 W of pump power while the threshold input power reached 550 mW.

The optimum spot position on the gain sample was marked for future use and a second cavity configuration was designed. We switched to a V-shaped cavity where the same output coupler from before was used as one end mirror. A flat high reflector was positioned as the other end mirror and the gain sample acted as a folding mirror. As it was crucial to get an overlap between the pump spot and the intra cavity mode, simple Gaussian beam formula were used to decide on where to place the end mirrors. The output coupler was 47.5 mm away from the gain and the flat reflector was around 2.4 mm away. This gave a cavity mode spot of around 40 μm-radius. The angle formed by the two arms was kept to a minimum to avoid forming an elongated mode.

The V-cavity yielded 40 mW of 830-nm-VECSEL power at a temperature of -33.4^{o}C with around 1.6 W of red-pump power while the threshold pump was 0.56 W. The output of the VECSEL was aligned with a spectrum analyser and a few sets of spectra were recorded at different temperatures and pump powers whilst also recording the output powers. Fig 6.10 shows the laser output power vs. input power whilst Fig 6.11 shows centre wavelength plotted against input power for the case where T=-33.4^{o}C.

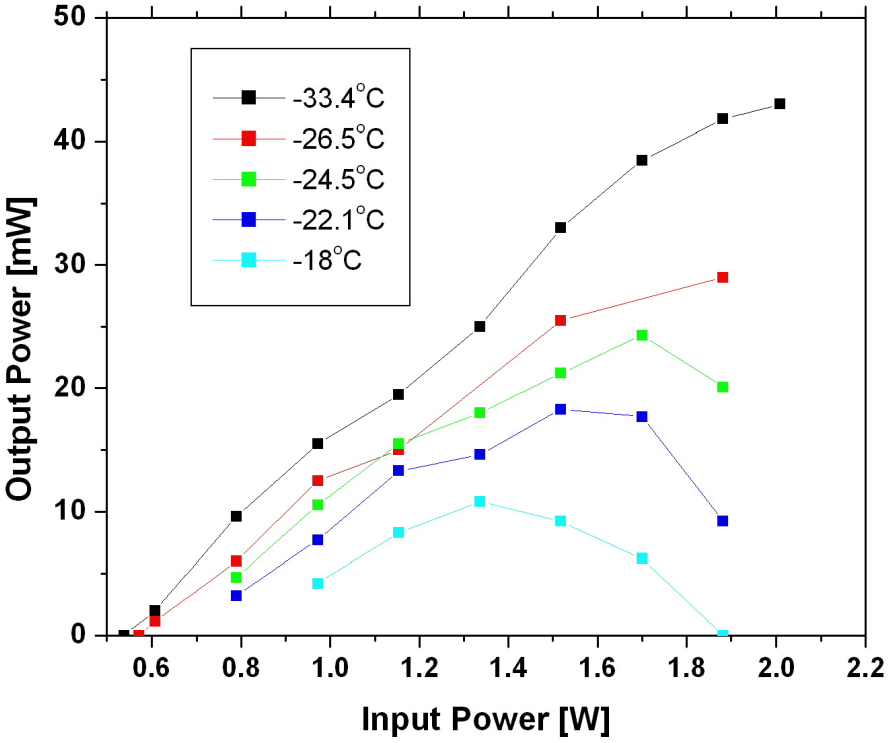

FIGURE 6.10: Power output of 830 nm-VECSEL at different gain sample temperatures. Roll over starts to occur as temperatures increase

The sample's centre wavelength shifts at a rate of about 1.6 nm/W in the early stages of pumping up to around 1.15 W then this rate slows down to about 0.15 nm/W due to thermal roll over. It is worth noting that the sample's degradation over time plays a role in damaging its performance in the long term too. Fig 6.12 shows the centre wavelength shift with respect to the sample temperature when it is pumped with 1.5 W of red power. We can extract the wavelength shift to be about 0.027 nm/K in this case. These numbers differ from rates we expect for samples we usually work with in the 1 micron region due to the higher thermal loads associated with the shorter wavelength pumping.

6.4.2 Mode Locked Operation

A Z-shaped laser cavity with a fundamental pulse repetition frequency of 1.9 GHz was used in this work, consisting of a 25 mm radius of curvature, 0.7% output coupler, the gain sample acting as a folding mirror, a second cavity folding mirror with a radius of curvature of 20 mm and the SESAM as the second end mirror. The mode radii on

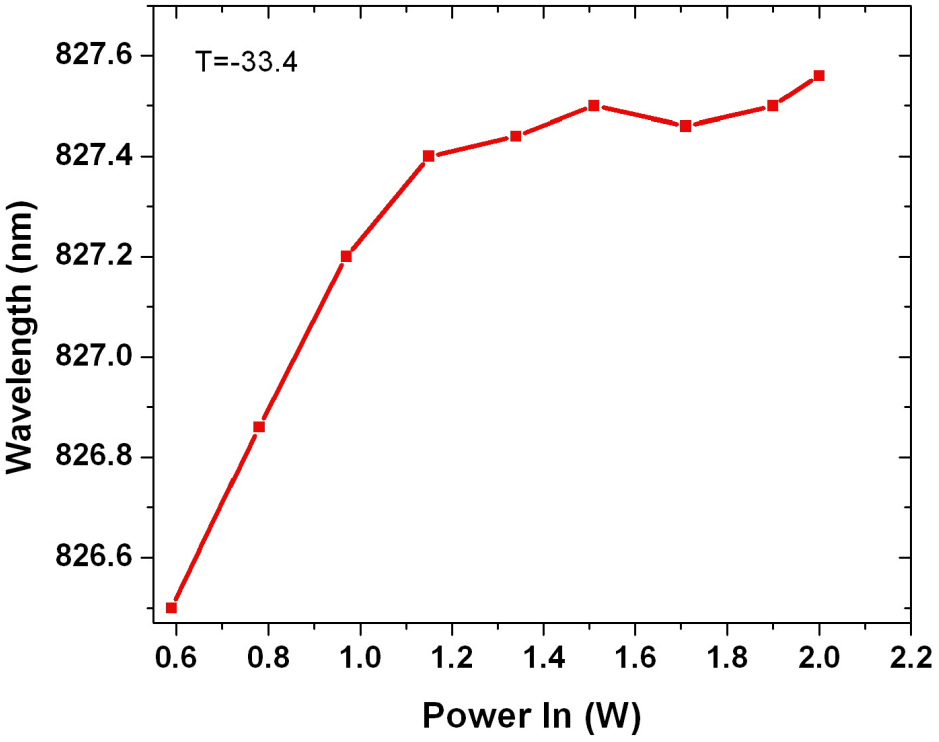

FIGURE 6.11: The shift in the centre wavelength of the 830 nm-VECSEL is plotted against pump power with the gain sample temperature set to T=-33.4^o C

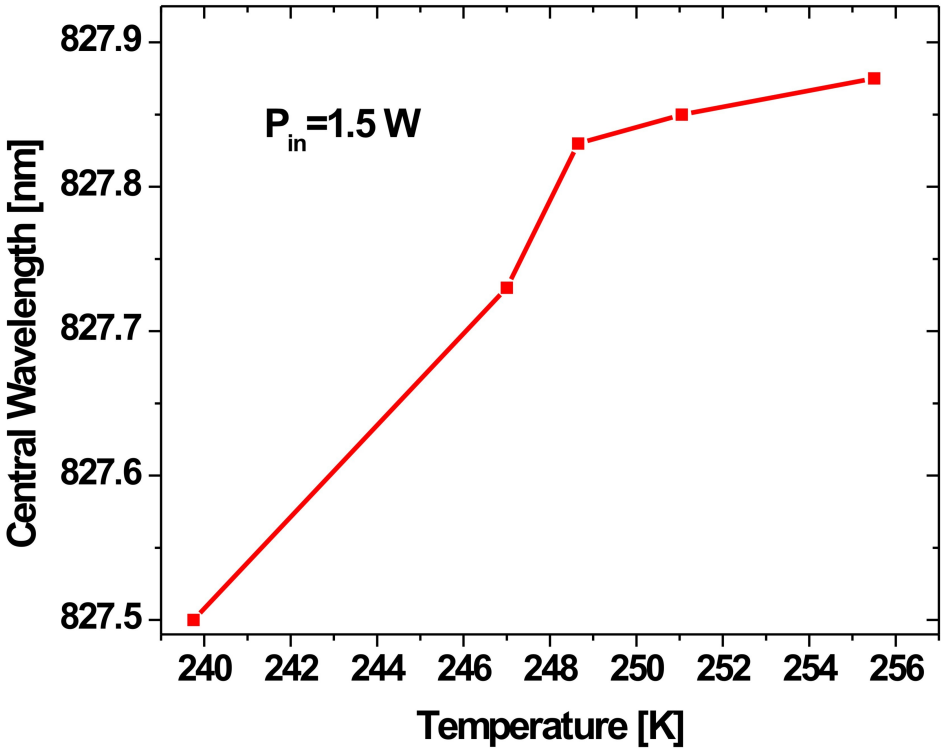

FIGURE 6.12: The shift in the centre wavelength of the 830 nm-VECSEL is plotted against sample temperature with the gain sample pumped with 1.5 W

the SESAM and the gain structure were calculated to be 11.2 and 40 μm, respectively, ensuring that the intra-cavity pulse saturated the SESAM faster than the gain, leading to stable mode locking.

The mode locked pulse train from the OP-VECSEL was characterized using an optical spectrum analyser, autocorrelator and RF spectrum analyser. An optical spectrum and second harmonic intensity autocorrelation of the output pulse train are shown in Fig 6.13 and Fig 6.14 respectively. The inset graph in Fig 6.14 is RF spectrum of the pulse train indicating a repetition rate of 1.9 GHz. The optical spectrum is centred at 832.4 nm and has a width of 0.63 nm FWHM. The autocorrelation gives a pulse duration of 15.3 ps assuming a Lorentzian pulse shape. The pulses are approximately 20 times transform limited, showing that these pulses are highly chirped. The average output power of the laser was measured to be 5 mW, with an incident pump power of 1.1 W.

The low T_0 of GaAs/AlGaAs quantum well systems leads to a high degree of temperature sensitivity and reduced tolerance of temperature increases in the pumped region. The local heating caused by the absorbed pump light in this demonstration was non-optimal owing to the mismatch between the pump spot and the laser mode, which impairs efficiency. Experimentally, the sample mount was temperature controlled to -33^{o}C to improve efficiency and provide optimal output power. As a result of the low operating temperature, the gain structure, designed to be anti-resonant at 20^{o}C, was in fact operating near a micro-cavity resonance. This introduces a large amount of higher order dispersion, leading to the long highly chirped pulses that were observed.

6.5 Conclusion

The first demonstration of a passively mode-locked OP-VECSEL operating at a wavelength of 832.5 nm has been shown. A design characteristic is discussed for obtaining fast surface recombination in the SESAM for use in mode-locked VECSELs at this wavelength based on a GaAs quantum well located 2 nm from the air interface, surrounded by GaAsP barriers. This method is already being used in the near infra-red (1042 nm) VECSEL used in the first chapters of this thesis. However, the additional fast recovery component of the absorption due to the Stark effect is not observed around 832 nm in our samples. Pulses of a duration of 15.3 ps were produced, with an optical bandwidth of 0.63 nm FWHM. These pulses were 20 times transform limited.

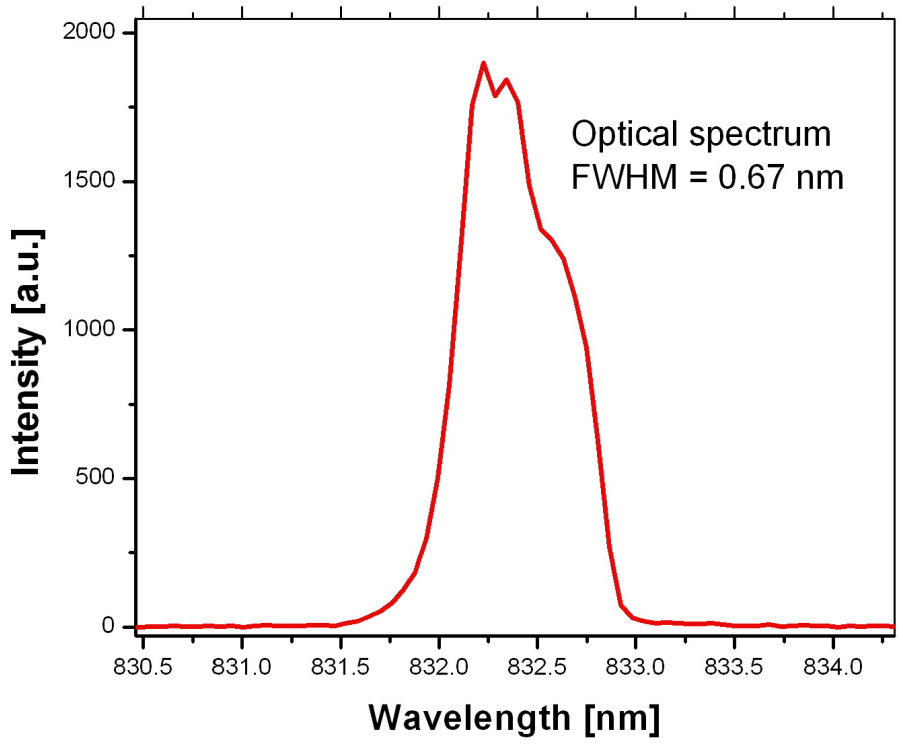

FIGURE 6.13: Optical Spectrum centered at around 832nm of a mode-locked pulse obtained using an anti-resonant gain sample and a SESAM

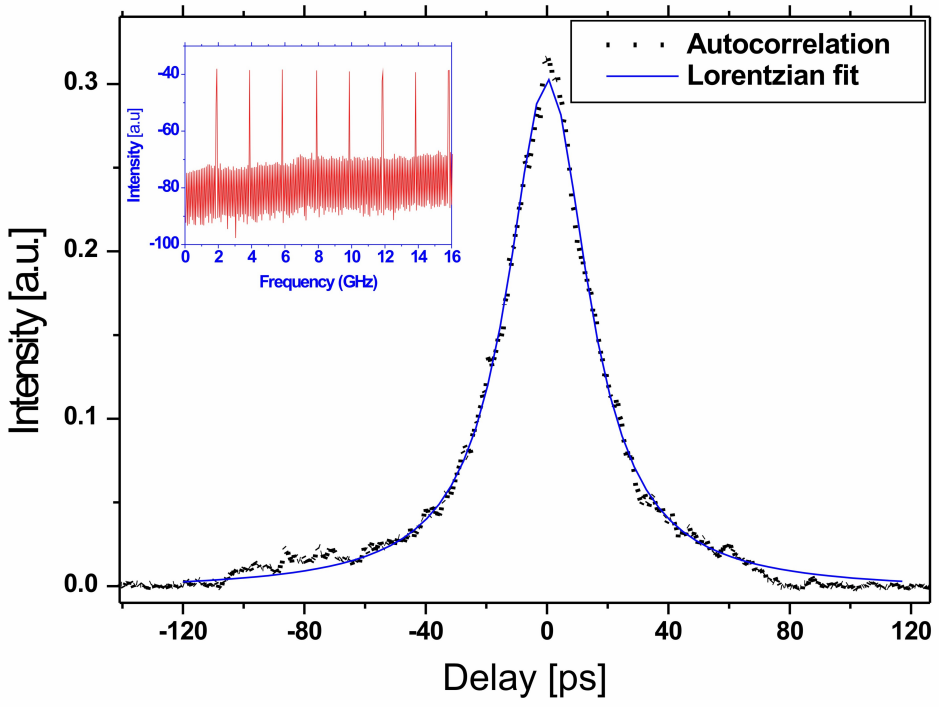

FIGURE 6.14: An intensity autocorrelation of a pulse corresponding to the optical spectrum shown in Fig 6.13. A Lorentzian fit is also plotted. Inset: An RF spectrum of the pulse train.

The main motivation for this work was to discover compact alternatives to Ti:Sapphire lasers in the form of a mode locked VECSEL. Huge efforts have been made to increase the repetition rate of the Ti:Sapphire. This proved to be hard because of Q-switching instabilities among other things. Recently, Gigaoptics reported a 10 GHz repetition rate producing 42 fs in [91]. Thermal issues due to the shorter wavelength pump compared to the 1 μm VECSEL hampers the available output power and operating conditions. The difficulty in obtaining a source for pumping with red wavelength is also a problem, although this is becoming less of an issue as more and more companies are introducing systems with good beam quality and high powers.

Possible work in the future includes the use of a thin anti-reflection coated diamond heat-spreader to improve the heat removal from the active region of the VECSEL, increasing efficiency and increasing the operating temperature. This will lead to higher average powers and shorter pulse durations.

Chapter 7

Conclusion

The work that has been presented in this thesis is all centred on VECSELs, their characterisation, their mode-locking with a saturable absorber, modelling of their pulses and a successful first time application test in generating terhertz radiation. The main target has always been to understand the way in which they operate in order improve their performance, and also to explore possible applications for the plethora of advantages they have over many other lasers.

7.1 VECSEL Development Results

In terms of the process of development of VECSELs, this has been done both with theoretical and experimental work. Chapters 3 and 4 were dedicated to understanding the process of mode-locking in these lasers. It was mainly directed at the saturable absorber side of the laser but it provides a useful tool to improve the performance of the mode-locked VECSEL. It showed the first theoretical demonstration of the Optical Stark Effect mechanism in shortening pulses in a saturable absorber mirror. Although the model omitted all dispersion elements of a real-life VECSEL, which we believe are small, it represents a major step in the understanding of the operation of these devices. Implementing a code for the full VECSEL cavity is the next target of the model which will include gain saturation, dispersion and pulse splitting. This will allow us to understand the phase structure of the pulses and help us predict the pulse duration limit for real systems.

Chapter 6 was dedicated to the making of a VECSEL in the Ti-Sapphire-dominated wavelength region of 830 nm. The foundation of this work was to construct a pumping

module emitting at 665 nm due to the lack of a suitable commercial source. Two diode lasers had their output combined to pump the gain sample with more than 1.5 W of power. The results obtained showed some promise in that it was the first mode-locked VECSEL or semiconductor-based laser at that wavelength. Since most applications of ultrashort pulses have been demonstrated in this wavelength range, the potential is big for this mode-locked VECSEL if a few obstacles are overcome. These include finding a high power red-wavelength pump with good beam quality capable of driving these samples. Thermal issues associated with pumping with lower wavelength are greatly enhanced compared to the 1 μm VECSEL. One way of overcoming this problem is the use of heat-spreaders in front of the sample but this will need to take into account the etalon effects associated with the thin layer of the heat-spreader. These can be solved by the anti-reflection coating of the layer. Substrate removal via chemical etching is another possible way to reduce thermal issues as it is the main source of the heating effects. The VECSEL presented here has a long way to achieve what the Ti-Sapphire achieved since its introduction. There is plenty of room for improvements in all aspects of the operation of the VECSEL.

7.2 VECSEL Application Results

The main application tested in this thesis has been discussed in Chapter 5 where the first all-semiconductor room-temperature terahertz spectrometer was built and characterised. After recent attempts to make such a spectrometer were undermined by the lack of efficient antenna at around 1040 nm, LT-GaAs was found to be a very good emitter with absorption arising from mid-gap defect states in the material. Being based on semiconductor material, the spectrometer can theoretically be made into a very compact and mobile device that can be used in all kinds of environment.

In order to be able to compete with other THz spectrometers, more efficient antenna material needs to be developed. Material with fast recovery time of less than 200 fs in the near infra-red is needed to be able to achieve broader bandwidth radiation. There has been a lot of research done into material that can be pumped by Ti-Sapphire at around the 820 nm wavelength but not much near the 1 μm region. Making shorter pulses from VECSELs is also critical as it complements the speed of the material. Modelling results from Chapter 4 have shown a fundamental limit to pulse shortening of twice the dephasing time which we estimated to be about 35 fs. More recently, we have observed

a regime in which our VECSELs can give pulses of this order. This is currently being investigated and characterised.

Terahertz spectrometers need further development to realize their full market potential; development to bring the cost down and most significantly overcome the water absorption problem. An integrated THz time domain spectrometer in an all-semiconductor configuration would be ideal for chemical and biological sensing applications. Output powers from VECSELs can be optimised further by either the use of multi-gain chip or just pumping a larger spot on the gain. This should be a straightforward way of obtaining more time domain signal. Improving the stability of the laser output will help a great deal in lowering the noise floor and hence increase the signal-to-noise-ratio.

VECSELs can be phase locked to each other electrically by controlling the arrival time of the optical pulses on the THz receiver and detector. This allows the replacement of the mechanical delay line as the phase difference of the laser pulse trains can be electrically controlled giving faster measurements for the same accuracy. This means that the resolution of the THz spectrum will be higher and the data acquisition faster. This apparatus is an attempt to improve the classical THz spectrometer on all aspects: no moving parts (reliability), faster operation, higher spectral resolution, lower cost and portability.

Appendix A

NAsP Designs

Layers lists for the NAsP designs which indicates the material used with the corresponding thickness.

SESAM Design wavelength: 840nm

	Material	Thickness [nm]	
Top	GaAs0.79P0.21	2	0,35*(lambda/4)
	GaAs	4,8	
	GaAs0.75P0.25	14,1	
	AlGaAs-Gradient	6,8	
	AlAs	55,5	
29 X	AlGaAs-Gradient	13,6	
	Al0.2Ga0.8As	48	
	AlGaAs-Gradient	13,6	
	AlAs	55,5	
	AlGaAs-Gradient	6,8	
	GaAs-Substrate		

FIGURE A.1: Layer list for the SESAM sample grown at NAsP

VECSEL Design wavelength: 835nm

	Material	Thickness [nm]	
Top	InGaP	8	
	AlAs	101,1	1,45*(lambda/4)
	Al0.2Ga0.8As	109,4	
	GaAs	5,6	
	Al0.2Ga0.8As	10	
	GaAs	5,6	
	Al0.2Ga0.8As	98,2	
2 X	GaAs	5,6	
	Al0.2Ga0.8As	10	
	GaAs	5,6	
	Al0.2Ga0.8As	98,2	
	GaAs	5,6	
	Al0.2Ga0.8As	10	
	GaAs	5,6	
	Al0.2Ga0.8As	106,4	
	GaAs	5,6	
	Al0.2Ga0.8As	114,7	
	GaAs	5,6	
	Al0.2Ga0.8As	117,7	
	AlGaAs-Gradient	6,8	
	AlAs	55,1	
	AlGaAs-Gradient	13,5	
31 X	Al0.2Ga0.8As	47,7	
	AlGaAs-Gradient	13,5	
	AlAs	55,1	
	AlGaAs-Gradient	6,8	
	GaAs-Substrate		

FIGURE A.2: Layer list for the gain sample grown at NAsP

Appendix B

Selected Conference and Journal Publications

[70] Zakaria Mihoubi, Keith G. Wilcox, Stephen Elsmere, Adrian Quarterman, Rakchanok Rungsawang, Ian Farrer, Harvey E. Beere, David A. Ritchie, Anne Tropper, and Vasileios Apostolopoulos. All-semiconductor room-temperature terahertz time domain spectrometer. *Optics Letters*, 33(18):2125 – 2127, 2008.

[49] G.J. Daniell, Z. Mihoubi, K.G. Wilcox, and A.C. Tropper. Numerical model of the optical stark effect as a mode-locking mechanism for femtosecond vertical-external-cavity surface-emitting semiconductor lasers. 2008 Conference on Quantum Electronics and Laser Science Conference on Lasers and Electro-Optics, CLEO/QELS page CThF3, 2008.

[50] Z. Mihoubi, G.J. Daniell, K.G. Wilcox, and A.C. Tropper. Numerical model of a vertical-external-cavity surface-emitting semiconductor lasers mode-locked by the optical stark effect. 2008 International Conference on Numerical Simulation of Optoelectronic Devices, NUSOD'08 pages 91 – 92, 2008.

[88] K.G. Wilcox, Z. Mihoubi, S. Elsmere, A. Quarterman, H.D. Foreman, S. Hashimoto, T. Sudmeyer, U. Keller, and A. Tropper. Passively modelocked 832 nm vertical-external-cavity surface-emitting semiconductor laser producing 15.3 ps pulses at 1.9 GHz repetition rate. *Electronics Letters*, 44(25):1469 – 1470, 2008.

[30] Keith G. Wilcox, Zakaria Mihoubi, G.J. Daniell, Stephen Elsmere, Adrian Quarterman, Ian Farrer, David A. Ritchie, and Anne Tropper. Ultrafast optical stark mode-locked semiconductor laser. *Optics Letters*, 33(23):2797 – 2799, 2008.

[31] Keith G. Wilcox, Zakaria Mihoubi, Stephen Elsmere, Adrian Quarterman, Ian Farrer, David A. Ritchie, and Anne Tropper. 70-fs transform-limited pulses emitted by InGaAs/GaAs quantum well laser. In *Advanced Solid-State Photonics*, page ME4. Optical Society of America, 2009.

[57] Adrian Quarterman, Keith Wilcox, Vasilis Apostolopoulos, Zakaria Mihoubi, Stephen Elsmere, Ian Farrer, David Ritchie, and Anne Tropper. 70-fs transform-limited pulses emitted by InGaAs/GaAs quantum well laser. *Nature Photonics* awaiting publication.

[85] A.H. Quarterman, K.G. Wilcox, S.P. Elsmere, Z. Mihoubi, and A.C. Tropper. Active stabilisation and timing jitter characterisation of sub-500 fs pulse passively modelocked vecsel. *Electronics Letters*, 44(19):1135 – 1137, 2008.

[53] Sjoerd Hoogland, Arnaud Garnache, Keith G. Wilcox, Zakaria Mihoubi, Stephen Elsmere, Adrian Quarterman, and Anne Tropper. Spectrotemporal gain bandwidth measurement in an InGaAs/GaAsP quantum well vertical-external-cavity surface-emitting semiconductor laser. CLEO / QELS2008 San Jose, USA CWD6.

[24] S.P. Elsmere, Z. Mihoubi, A.H. Quarterman, Pascal Dupriez, J. Nilsson, J.S. Roberts, and A.C. Tropper. High-repetition-rate subpicosecond source of fiber-amplified vertical-external-cavity surface-emitting semiconductor laser pulses. *IEEE Photonics Technology Letters*, 20(8):623 – 625, 2008.

[25] S.P. Elsmere, Z. Mihoubi, A. Quarterman, A.C. Tropper, P. Dupriez, J. Nilsson, and J.S. Roberts. High repetition-rate sub-picosecond source of fibre-amplified vertical-externalcavity surface-emitting semiconductor laser pulses. Conference on Lasers and Electro-Optics Europe. CF10-6. Munich, Germany, 2007.

Bibliography

[1] M. Kuznetsov, F. Hakimi, R. Sprague, and A. Mooradian. High-power (>0.5-W CW) diode-pumped vertical-external-cavity surface-emitting semiconductor lasers with circular tem00 beams. *IEEE Photonics Technology Letters*, 9(8):1063 – 1065, 1997.

[2] Mark Kuznetsov, Farhad Hakimi, Robert Sprague, and A. Mooradian. Design and characteristics of high-power (>0.5-W CW) diode-pumped vertical-external-cavity surface-emitting semiconductor lasers with circular tem_{00} beams. *IEEE Journal on Selected Topics in Quantum Electronics*, 5(3):561 – 573, 1999.

[3] Ursula Keller and Anne C. Tropper. Passively modelocked surface-emitting semiconductor lasers. *Physics Reports*, 429(2):67 – 120, 2006.

[4] A. Mooradian. High brightness cavity-controlled surface emitting gainas lasers operating at 980 nm. In *Conference on Optical Fiber Communication, Technical Digest Series*, volume 54, pages PD17/1 – PD17/3, 2001.

[5] Aram Mooradian. Overcoming hurdles on the road to more efficient diodes. *Photonics Spectra*, 39:59 – 60, 2005.

[6] S.S. Beyertt, T. Kubler, U. Brauch, A. Giesen, E. Gerster, F. Rinaldi, and P. Unger. Semiconductor thin-disk laser - comparison of spacer and quantum-well pumping. In *OSA Trends in Optics and Photonics Series*, volume 98, pages 294 – 298, 2005.

[7] S. Beyertt, U. Brauch, A. Giesen, E. Gerster, , and M. Zorn. Direct pumping of quantum wells improves performance of semiconductor thin-disk lasers. *Photonic Spectra*, 39(6):60 – 66, 2005.

[8] Svent Simon Beyertt, Martin Zorn, Thomas Kbler, Hans Wenzel, Markus Weyers, Adolf Giesen, Gnther Trnkle, and Uwe Brauch. Optical in-well pumping of a semiconductor disk laser with high optical efficiency. *IEEE Journal of Quantum Electronics*, 41(12):1439 – 1449, 2005.

[9] Jun Ho Lee, Jun Youn Kim, Sang Moon Lee, Jae Ryung Yoo, Ki Sung Kim, Soo Haeng Cho, Seong Jin Lim, Gi Bum Kim, Sung Min Hwang, Taek Kim, and Yong Jo Park. 9.1 W high-efficient continuous-wave end-pumped vertical-external-cavity surface-emitting semiconductor laser. *IEEE Photonics Technology Letters*, 18(20):2117 – 2119, 2006.

[10] Gi Bum Kim, Jun-Youn Kim, Junho Lee, Jaeryung Yoo, Ki-Sung Kim, Sang-Moon Lee, Soohaeng Cho, Seong-Jin Lim, Taek Kim, and Yongjo Park. End-pumped green and blue vertical external cavity surface emitting laser devices. *Applied Physics Letters*, 89(18):181106, 2006.

[11] Jun Ho Lee, Sang Moon Lee, Taek Kim, and Yong Jo Park. 7 W high-efficiency continuous-wave green light generation by intracavity frequency doubling of an end-pumped vertical external-cavity surface emitting semiconductor laser. *Applied Physics Letters*, 89(24):241107, 2006.

[12] Marc Schmid, Sarah Benchabane, Firuz Torabi-Goudarzi, Richard Abram, Allister I. Ferguson, and Erling Riis. Optical in-well pumping of a vertical-external-cavity surface-emitting laser. *Applied Physics Letters*, 84(24):4860–4862, 2004.

[13] J.-M. Hopkins, S.A. Smith, C.W. Jeon, H.D. Sun, D. Burns, S. Calvez, M.D. Dawson, T. Jouhti, and M. Pessa. 0.6 W CW GaInNAs vertical external-cavity surface emitting laser operating at 1.32 μm. *Electronics Letters*, 40(1):30 – 31, 2004.

[14] Hans Lindberg, Martin Strassner, and Anders Larsson. Improved spectral properties of an optically pumped semiconductor disk laser using a thin diamond heat spreader as an intracavity filter. *IEEE Photonics Technology Letters*, 17(7):1363 – 1365, 2005.

[15] M. Rahim, F. Felder, M. Fill, and H. Zogg. Optically pumped 5 μm IV-VI VECSEL with Al-heat spreader. *Opt. Lett.*, 33(24):3010–3012, 2008.

[16] Juan L. A. Chilla, Stuart D. Butterworth, Alexander Zeitschel, John P. Charles, Andrea L. Caprara, Murray K. Reed, and Luis Spinelli. High-power optically pumped semiconductor lasers. volume 5332, pages 143–150. SPIE, 2004.

[17] S. Lutgen, T. Albrecht, P. Brick, W. Reill, J. Luft, and W. Spath. 8 W high-efficiency continuous-wave semiconductor disk laser at 1000 nm. *Applied Physics Letters*, 82(21):3620 – 3622, 2003.

[18] Jennifer E. Hastie, Chan Wook Jeon, David Burns, John-Mark Hopkins, Stephane Calvez, Richard Abram, and Martin D. Dawson. A 0.5 W, 850 nm $Al_xGa_{1-x}As$ vecsel with intra-cavity Silicon Carbide heatspreader. In *Proceedings of SPIE - The International Society for Optical Engineering*, volume 5137, pages 201 – 206, 2002.

[19] J.E. Hastie, J.-M. Hopkins, S. Calvez, Chan Wook Jeon, D. Burns, R. Abram, E. Riis, A.I. Ferguson, and M.D. Dawson. 0.5-W single transverse-mode operation of an 850-nm diode-pumped surface-emitting semiconductor laser. *Photonics Technology Letters, IEEE*, 15(7):894–896, 2003.

[20] K.S. Kim, J.R. Yoo, S.M. Lee, S.J. Lim, J.Y. Kim, J.H. Lee, S.H. Cho, T. Kim, and Y.J. Park. Highly efficient InGaAs QW vertical external cavity surface emitting lasers emitting at 1060nm. *Journal of Crystal Growth*, 287(2):629 – 632, 2006.

[21] Li Fan, Mahmoud Fallahi, Jörg Hader, Aramais R. Zakharian, Jerome V. Moloney, James T. Murray, Robert Bedford, Wolfgang Stolz, and Stephan W. Koch. Multichip vertical-external-cavity surface-emitting lasers: a coherent power scaling scheme. *Opt. Lett.*, 31(24):3612–3614, 2006.

[22] Li Fan, M. Fallahi, A.R. Zakharian, J. Hader, J.V. Moloney, R. Bedford, J.T. Murray, W. Stolz, and S.W. Koch. Extended tunability in a two-chip vecsel. *Photonics Technology Letters, IEEE*, 19(8):544–546, 2007.

[23] P. Dupriez, C. Finot, A. Malinowski, J.K. Sahu, J. Nilsson, D.J. Richardson, K.G. Wilcox, H.D. Foreman, and A.C. Tropper. High-power, high repetition rate picosecond and femtosecond sources based on Yb-doped fiber amplification of VECSELs. *Optics Express*, 14(21):9611.

[24] S.P. Elsmere, Z. Mihoubi, A.H. Quarterman, Pascal Dupriez, J. Nilsson, J.S. Roberts, and A.C. Tropper. High-repetition-rate subpicosecond source of fiber-amplified vertical-external-cavity surface-emitting semiconductor laser pulses. *IEEE Photonics Technology Letters*, 20(8):623 – 625, 2008.

[25] S.P. Elsmere, Z. Mihoubi, A. Quarterman, A.C. Tropper, P. Dupriez, J. Nilsson, and J.S. Roberts. High repetition-rate sub-picosecond source of fibre-amplified vertical-externalcavity surface-emitting semiconductor laser pulses. In *Conference on Lasers and Electro-Optics Europe - Technical Digest*, 2007.

[26] H. Cao, L.R. Chen, J. Magna;, and S. LaRochelle. Tunable 4×10 GHz optically modelocked semiconductor fibre laser. *Electronics Letters*, 41(13):730 – 732, 2005.

[27] S. Hoogland, S. Dhanjal, A.C. Tropper, J.S. Roberts, R. Haring, R. Paschotta, F. Morier-Genoud, and U. Keller. Passively mode-locked diode-pumped surface-emitting semiconductor laser. *Photonics Technology Letters, IEEE*, 12(9):1135–1137, 2000.

[28] A. Garnache, S. Hoogland, A. C. Tropper, I. Sagnes, G. Saint-Girons, and J. S. Roberts. Sub-500-fs soliton-like pulse in a passively mode-locked broadband surface-emitting laser with 100 mW average power. *Applied Physics Letters*, 80(21):3892–3894, 2002.

[29] Peter Klopp, Florian Saas, Martin Zorn, Markus Weyers, and Uwe Griebner. 290-fs pulses from a semiconductor disk laser. *Opt. Express*, 16(8):5770–5775, 2008.

[30] Keith G. Wilcox, Zakaria Mihoubi, G.J. Daniell, Stephen Elsmere, Adrian Quarterman, Ian Farrer, David A. Ritchie, and Anne Tropper. Ultrafast optical stark mode-locked semiconductor laser. *Optics Letters*, 33(23):2797 – 2799, 2008.

[31] Keith G. Wilcox, Zakaria Mihoubi, Stephen Elsmere, Adrian Quarterman, Ian Farrer, David A. Ritchie, and Anne Tropper. 70-fs transform-limited pulses emitted by InGaAs/GaAs quantum well laser. In *Advanced Solid-State Photonics*, page ME4. Optical Society of America, 2009.

[32] A. Aschwanden, D. Lorenser, H. J. Unold, R. Paschotta, E. Gini, and U. Keller. 2.1-W picosecond passively mode-locked external-cavity semiconductor laser. *Opt. Lett.*, 30(3):272–274, 2005.

[33] D. Lorenser, H.J. Unold, D.J.H.C. Maas, A. Aschwanden, R. Grange, R. Paschotta, D. Ebling, E. Gini, and U. Keller. Towards wafer-scale integration of high repetition rate passively mode-locked surface-emitting semiconductor lasers. *Applied Physics B: Lasers and Optics*, 79(8):927–932, 2004.

[34] A.-R. Bellancourt, D.J.H.C. Maas, B. Rudin, M. Golling, T. Südmeyer, and U. Keller. Modelocked integrated external-cavity surface emitting laser. *IET Optoelectronics*, 3(2):61–72, 2009.

[35] Keith G. Wilcox, Mantas Butkus, Anne Tropper, Ian Farrer, David A. Ritchie, and Edik U. Rafailov. 870-fs passively mode-locked quantum dot SESAM semiconductor disk laser. In *Advanced Solid-State Photonics*, page MB19, 2009.

[36] M. Hoffmann, Y. Barbarin, D.J.H.C. Maas, M. Golling, I.L. Krestnikov, S.S. Mikhrin, A.R. Kovsh, T. Südmeyer, and U. Keller. Modelocked quantum dot vertical external cavity surface emitting laser. *Applied Physics B: Lasers and Optics*, 93(4):733 – 736, 2008.

[37] P.P. Vasil'ev and A.B. Sergeev. Generation of bandwidth-limited 2 ps pulses with 100 GHz repetition rate from multisegmented injection laser. *Electronics Letters*, 25(16):1049 – 1050, 1989.

[38] S.L Chuang. *Physics of Optoelectronic Devices*. Wiley-Interscience publication, 1995.

[39] Jennifer E. Hastie, Stephane Calvez, Martin D. Dawson, Tomi Leinonen, Antti Laakso, Jari Lyytikainen, and Markus Pessa. High power CW red vecsel with linearly polarized TEM_{00} output beam. *Optics Express*, 13(1):77 – 81, 2005.

[40] L. A. Coldren and S. W. Corzine. *Diode Lasers and Photonic Integrated Circuits*. WileyBlackwell, 1995.

[41] S. Hoogland. *Optically pumped vertical-external-cavity semiconductor emitting lasers*. PhD thesis, University of Southampton, 2003.

[42] M. Haiml, R. Grange, and U. Keller. Optical characterization of semiconductor saturable absorbers. *Applied Physics B: Lasers and Optics*, 79(3):331–339, 2005.

[43] H.A. Haus. Theory of mode locking with a slow saturable absorber. *IEEE Journal of Quantum Electronics*, QE-11(9):736 – 46, 1975.

[44] Hermann A. Haus. Theory of mode locking with a fast saturable absorber. *Journal of Applied Physics*, 46(7):3049 – 3058, 1975.

[45] Hermann A. Haus, James G. Fujimoto, and Erich P. Ippen. Analytic theory of additive pulse and Kerr lens mode locking. *IEEE Journal of Quantum Electronics*, 28(10):2086 – 2096, 1992.

[46] W. Chow and S. Koch. *Semiconductor-Laser Fundamentals: Physics of the Gain Materials*. Springer, 1999.

[47] A. Mysyrowicz, D. Hulin, A. Antonetti, A. Migus, W.T. Masselink, and H. Morkoc. Dressed excitons in a multiple-quantum-well structure: evidence for an optical stark effect with femtosecond response time. *Physical Review Letters*, 56(25):2748 – 51, 1986.

[48] S. Tsuda, W.H. Knox, S.T. Cundiff, W.Y. Jan, and J.E. Cunningham. Mode-locking ultrafast solid-state lasers with saturable bragg reflectors. *IEEE Journal of Selected Topics in Quantum Electronics*, 2(3):454 – 64, 1996.

[49] G.J. Daniell, Z. Mihoubi, K.G. Wilcox, and A.C. Tropper. Numerical model of the optical stark effect as a mode-locking mechanism for femtosecond vertical-external-cavity surface-emitting semiconductor lasers. In *2008 Conference on Quantum Electronics and Laser Science Conference on Lasers and Electro-Optics, CLEO/QELS*, page CThF3, 2008.

[50] Z. Mihoubi, G.J. Daniell, K.G. Wilcox, and A.C. Tropper. Numerical model of a vertical-external-cavity surface-emitting semiconductor lasers mode-locked by the optical stark effect. In *2008 International Conference on Numerical Simulation of Optoelectronic Devices, NUSOD'08*, pages 91 – 92, 2008.

[51] V.M. Baev, T. Latz, and P.E. Toschek. Laser intracavity absorption spectroscopy. *Applied Physics B: Photophysics and Laser Chemistry*, 69(3):171 – 202, 1999.

[52] V.M. Baev, J. Escher, E. Paeth, R. Schuler, and P.E Toschek. Intra-cavity spectroscopy with diode lasers. *Applied Physics B: Lasers and Optics*, 55(6):463–477, 1992.

[53] Sjoerd Hoogland, Arnaud Garnache, Keith G. Wilcox, Zakaria Mihoubi, Stephen Elsmere, Adrian Quarterman, and Anne Tropper. Spectrotemporal gain bandwidth measurement in an ingaas/gaasp quantum well vertical-external-cavity surface-emitting semiconductor laser. In *2008 Conference on Quantum Electronics and Laser Science Conference on Lasers and Electro-Optics, CLEO/QELS*, page CWD6, 2008.

[54] K.G. Wilcox. *Ultrashort pulse surface emitting semiconductor lasers.* PhD thesis, University of Southampton, 2006.

[55] Orazio Svelto. *Principles of Lasers.* Plenum Press publication, 1998.

[56] G.K. Woodgate. *Elementary Atomic Structure.* Oxford University Press, 1983.

[57] Adrian Quarterman, Keith Wilcox, Vasilis Apostolopoulos, Zakaria Mihoubi, Stephen Elsmere, Ian Farrer, David Ritchie, and Anne Tropper. 70-fs transform-limited pulses emitted by InGaAs/GaAs quantum well laser. *Nature Photonics awaiting publication.*

[58] P.H. Siegel. Terahertz technology. *Microwave Theory and Techniques, IEEE Transactions on*, 50(3):910–928, 2002.

[59] P.H. Siegel. Terahertz technology in biology and medicine. *Microwave Theory and Techniques, IEEE Transactions on*, 52(10):2438–2447, 2004.

[60] K. Humphreys, J.P. Loughran, M. Gradziel, W. Lanigan, T. Ward, J.A. Murphy, and C. O'Sullivan. Medical applications of terahertz imaging: a review of current technology and potential applications in biomedical engineering. volume 1, pages 1302–1305, 2004.

[61] D.H. Auston. Picosecond optoelectronic switching and gating in silicon. *Applied Physics Letters*, 26(3):101 – 103, 1975.

[62] D.H. Auston, K.P. Cheung, and P.R. Smith. Picosecond photoconducting hertzian dipoles. *Applied Physics Letters*, 45(3):284 – 286, 1984.

[63] P.R. Smith, D.H. Auston, and M.C. Nuss. Subpicosecond photoconducting dipole antennas. *IEEE Journal of Quantum Electronics*, 24(2):255 – 260, 1988.

[64] P. F. Moulton. Spectroscopic and laser characteristics of ti:al$_2$o$_3$. *J. Opt. Soc. Am. B*, 3(1):125–133, 1986.

[65] Charles A. Schmuttenmaer. Exploring dynamics in the far-infrared with terahertz spectroscopy. *Chemical Reviews*, 104(4):1759–1780, 2004.

[66] Michael Nagel, Peter Haring Bolivar, Martin Brucherseifer, Heinrich Kurz, Anja Bosserhoff, and Reinhard Büttner. Integrated planar terahertz resonators for femtomolar sensitivity label-free detection of dna hybridization. *Appl. Opt.*, 41(10):2074–2078, 2002.

[67] Paul A. George, Wallace Hui, Farhan Rana, Benjamin G. Hawkins, A. Ezekiel Smith, and Brian J. Kirby. Microfluidic devices for terahertz spectroscopy of biomolecules. *Opt. Express*, 16(3):1577–1582, 2008.

[68] Li Cheng, Shin'ichiro Hayashi, Adrian Dobroiu, Chiko Otani, Kodo Kawase, Teruo Miyazawa, and Yuichi Ogawa. Terahertz-wave absorption in liquids measured using the evanescent field of a silicon waveguide. *Applied Physics Letters*, 92(18):181104, 2008.

[69] K.G. Wilcox, F. Rutz, R. Wilk, H.D. Foreman, J.S. Roberts, J. Sigmund, H.L. Hartnagel, M. Koch, and A.C. Tropper. Terahertz imaging system based on lt-GaAsSb antenna driven by all-semiconductor femtosecond source. *Electronics Letters*, 42(20):1159 – 1161, 2006.

[70] Zakaria Mihoubi, Keith G. Wilcox, Stephen Elsmere, Adrian Quarterman, Rakchanok Rungsawang, Ian Farrer, Harvey E. Beere, David A. Ritchie, Anne Tropper, and Vasileios Apostolopoulos. All-semiconductor room-temperature terahertz time domain spectrometer. *Optics Letters*, 33(18):2125 – 2127, 2008.

[71] R. A. Cheville and S. L. Dexheimer. *Terahertz Time Domain Spectroscopy with Photoconductive Antennas*. Taylor & Francis, 2008.

[72] P.U. Jepsen, R.H. Jacobsen, and S.R. Keiding. Generation and detection of terahertz pulses from biased semiconductor antennas. *Journal of the Optical Society of America B (Optical Physics)*, 13(11):2424 – 36, 1996.

[73] K. Bock, H. L. Hartnagel, and J. Dumas. *Surface induced electromigration in GaAs devices*. Wiley & Sons, 1992.

[74] L. Duvillaret, F. Garet, J.-F. Roux, and J.-L. Coutaz. Analytical modeling and optimization of terahertz time-domain spectroscopy experiments, using photoswitches as antennas. *Selected Topics in Quantum Electronics, IEEE Journal of*, 7(4):615–623, 2001.

[75] K. Sakai. In *Terahertz Optoelectronics*, pages 6–26, 2005.

[76] Masahiko Tani, Kwang-Su Lee, and X.-C. Zhang. Detection of terahertz radiation with low-temperature-grown gaas-based photoconductive antenna using 1.55 μm probe. *Applied Physics Letters*, 77(9):1396–1398, 2000.

[77] D. Rutledge, D. Neikirk, and D Kasilingam. In *Infrared and Millimeter Waves*, volume 10, 1983.

[78] Rajind Mendis, Cezary Sydlo, Jochen Sigmund, Michael Feiginov, Peter Meissner, and Hans L. Hartnagel. Tunable CW-THz system with a log-periodic photoconductive emitter. *Solid-State Electronics*, 48(10-11 SPEC ISS):2041 – 2045, 2004.

[79] J. Sigmund, C. Sydlo, H.L. Hartnagel, N. Benker, H. Fuess, F. Rutz, T. Kleine-Ostmann, and M. Koch. Structure investigation of low-temperature-grown GaAsSb, a material for photoconductive terahertz antennas. *Applied Physics Letters*, 87(25):252103, 2005.

[80] C. Baker, I. S. Gregory, W. R. Tribe, I. V. Bradley, M. J. Evans, M. Withers, P. F. Taday, V. P. Wallace, E. H. Linfield, A. G. Davies, and M. Missous. Terahertz pulsed imaging with 1.06 μu m laser excitation. *Applied Physics Letters*, 83(20):4113–4115, 2003.

[81] B. B. Hu, X.-C. Zhang, and D. H. Auston. Terahertz radiation induced by subband-gap femtosecond optical excitation of GaAs. *Phys. Rev. Lett.*, 67(19):2709–2712, Nov 1991.

[82] Martin van Exter, Ch. Fattinger, and D. Grischkowsky. Terahertz time-domain spectroscopy of water vapor. *Opt. Lett.*, 14(20):1128–1130, 1989.

[83] G. Mouret, W. Chen, D. Boucher, R. Bocquet, P. Mounaix, D. Thron, and D. Lippens. High-power terahertz radiation from a high-repetition-rate large-aperture photoconducting antenna. *Microwave and Optical Technology Letters*, 17(1):23–27, 1998.

[84] A. Bartels, A. Thoma, C. Janke, T. Dekorsy, A. Dreyhaupt, S. Winnerl, and M. Helm. High-resolution thz spectrometer with kHz scan rates. *Opt. Express*, 14(1):430–437, 2006.

[85] A.H. Quarterman, K.G. Wilcox, S.P. Elsmere, Z. Mihoubi, and A.C. Tropper. Active stabilisation and timing jitter characterisation of sub-500 fs pulse passively modelocked vecsel. *Electronics Letters*, 44(19):1135 – 1137, 2008.

[86] D. H. Sutter, G. Steinmeyer, L. Gallmann, N. Matuschek, F. Morier-Genoud, U. Keller, V. Scheuer, G. Angelow, and T. Tschudi. Semiconductor saturable-absorber mirror assisted Kerr-lens mode-locked Ti:Sapphire laser producing pulses in the two-cycle regime. *Opt. Lett.*, 24(9):631–633, 1999.

[87] R. Ell, U. Morgner, F. X. K AÂrtner, J. G. Fujimoto, E. P. Ippen, V. Scheuer, G. Angelow, T. Tschudi, M. J. Lederer, A. Boiko, and B. Luther-Davies. Generation of 5-fs pulses and octave-spanning spectra directly from a Ti:Sapphire laser. *Opt. Lett.*, 26(6):373–375, 2001.

[88] K.G. Wilcox, Z. Mihoubi, S. Elsmere, A. Quarterman, H.D. Foreman, S. Hashimoto, T. Sudmeyer, U. Keller, and A. Tropper. Passively modelocked 832 nm vertical-external-cavity surface-emitting semiconductor laser producing 15.3 ps pulses at 1.9 GHz repetition rate. *Electronics Letters*, 44(25):1469 – 1470, 2008.

[89] Sadao Adachi. GaAs, AlAs, and $Al_xGa_{1-x}As$: Material parameters for use in research and device applications. *Journal of Applied Physics*, 58(3):R1–R29, 1985.

[90] J.I. Mackenzie. *High-brightness diode-pumped waveguide lasers.* PhD thesis, University of Southampton, 2006.

[91] A. Bartels, D. Heinecke, and S. A. Diddams. Passively mode-locked 10 Ghz femtosecond Ti:Sapphire laser. *Opt. Lett.*, 33(16):1905–1907, 2008.